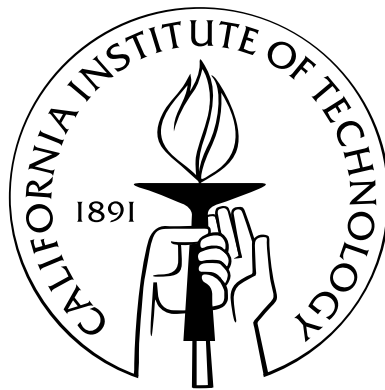


Low-Coherence Interferometric Imaging: Solution of the One-Dimensional Inverse Scattering Problem

Thesis by
M. Julián Chaubell

In Partial Fulfillment of the Requirements
for the Degree of
Doctor of Philosophy



California Institute of Technology
Pasadena, California

2004
(Defended September 5, 2003)

© 2004

M. Julián Chaubell

All Rights Reserved

To
My Father

Acknowledgements

It is not possible to put into words my deep appreciation for my Ph.D advisor, Prof. Oscar Bruno. Not only did he serve as my advisor in mathematics, but he also supported me as I dealt with the innumerable challenges of my life as a graduate student. Throughout the years he managed to perfectly balance our work relationship with what became, indeed, our friendship. Always ready to listen, always willing to show me the way, Oscar has been my mentor, my advocate, and my friend. Thank you for all of this, Oscar.

I want to acknowledge the tremendous support of my entire family, from my mother, Cristina, down to my youngest niece. In spite of the thousands of miles separating us, the love I felt in every one of their calls made it easier for me to be so far from home. I am lucky to have been able to make my girlfriend Nance's family my own as well. I'd like to thank all of them, and especially Nance's parents, Millie and Don, for opening their home and hearts to me during the past five years.

For her help, kindness, and thoughtfulness, I would like to thank our administrator, Ms. Sheila Shull. I must thank the generous and talented system administrator Chad Schmutzer for his ever-ready willingness to solve the countless unpredictable problems I encountered with computers. To my excellent neighbor, Cristophe Geuzaine, I would like to thank for helping me expand my knowledge of programming languages. There are also a few people who truly made a difference in my first years at Caltech. I would like to thank Jason Kastner, Eva Peral and McKay Hyde for their enormous help during my first year as a graduate student. I owe a special thank to you, McKay, for opening the door of your home to me, and for always being willing to help and listen. I wish to thank Patricia Cruz for her contributions towards the optimization algorithm that was a result of her stay at Caltech as a summer intern in 2001. I also want to mention Stephane Lintner who spent some time working with me in the summer of 2000 and Danny Petrsek who was my longtime officemate. To all in the Applied and Computational Mathematics department, thank you

for this huge opportunity to grow in this career.

Adrian Lew and Florian Gstrein have been steady friends. Their entertaining lunchtime conversations in the Rathskeller were such welcome distractions. Thank you also to Maria Hernandez, an excellent friend, for the supportive and valuable discussions during our stay at Caltech. I would like to thank Federico Spedalieri for providing me with such insight into the lifestyle of the U.S. and Caltech. And to Diego Dugatkin for his always enjoyable presence. I also want to mention others who were very important to me during my stay at Caltech including Marisol, Alejandro, Eduardo, Carla, Raul, Flavia, Marta and Patricia.

I was glad to be a part of the Caltech Rugby Club. It was this organization that allowed me to find a balance between my academic and athletic life and to discover the friendship of Calum Chisholm, Steve Callander and Gregg Caldwell.

Amongst all from whom I learned so much, I must mention preeminently Prof. Gloria Frontini, who introduced me to the world of applied mathematics. Her support, encouragement, and motivating influence made it easier for me to make the decision to accept the wonderful challenge of studying at Caltech. I would also like to thank the Universidad Nacional de Mar del Plata where I completed my undergraduate studies and where I took my first steps in mathematics.

There is a person who is special to me—she is the warmth, the balance, the support. She is always there. I specially want to thank you for all your love, Nance.

The last note in my acknowledgments is in honor of my father, who always encouraged me to go one step further. It was the memory of his words that gave me light when everything seemed dark, his voice that guided me in every moment of crisis. It is to his memory that I dedicate this work.

Abstract

Optical coherence tomography (OCT) is a non-invasive imaging technique based on the use of light sources exhibiting a low degree of coherence. Low coherence interferometric microscopes have been successful in producing internal images of thin pieces of biological tissue; typically samples of the order of 1 mm in depth have been imaged, with a resolution of the order of 10 to 20 μm in some portions of the sample. In this thesis, I deal with the imaging problem of determining the internal structure of a body from backscattered laser light and low-coherence interferometry. In detail, I formulate and solve an inverse problem which, using the interference fringes that result as the back-scattering of low-coherence light is made to interfere with a reference beam, produces maps detailing the values of the refractive index within the imaged sample. Unlike previous approaches to this imaging problem, the solver I introduce does not require processing at data collection time, and it can therefore produce solutions for inverse problems of multi-layered structures containing thousands of layers *from back-scattering interference fringes only*. We expect that the approach presented in this work, which accounts fully for the statistical nature of the coherence phenomenon, should prove of interest in the fields of medicine, biology and materials science.

Contents

Acknowledgements	iv
Abstract	vi
1 Introduction	1
1.1 Overview of Chapters	2
2 Microscopy	4
2.1 A Brief History of Microscopy	4
2.2 Imaging Techniques	5
2.2.1 X Rays	5
2.2.1.1 X-ray Computed Tomography (CT)	6
2.2.2 Magnetic Resonance Imaging (MRI)	6
2.2.3 Confocal Fluorescence Microscopy	7
2.2.3.1 Two-Photon Excitation Fluorescence Microscopy	7
2.2.4 Confocal Scanning Microscopy	8
2.2.5 Ultrasound	8
2.2.6 Optical Coherence Tomography (OCT)	9
3 Inverse Problems	11
3.1 Introduction	11
3.2 Inversion Methods	13
3.2.1 The Tikhonov-Phillips Method	14
3.2.2 The Truncated Singular Value Decomposition	15
3.2.3 Iterative Methods	15
3.2.4 Regularization by Discretization	16

3.2.5	Maximum Entropy	17
3.3	Inverse Problems Arising in the Imaging Field	17
3.3.1	X-Ray CT - Radon Transform	17
3.3.2	Ultrasound Computed Tomography	19
3.3.3	Optical Tomography	19
3.4	1-D Inverse Problem for the Helmholtz Equation	20
4	OCT Model and Direct Problem	31
4.1	Introduction	31
4.2	Coherence	36
4.3	Layered Media	40
4.4	Fast Evaluation of the Function Σ	42
5	OCT Inverse Problem	53
5.1	Introduction	53
5.2	Absorption	53
5.2.1	Difficulty in the Evaluation of Pointwise κ Values	54
5.2.2	Absorption Averaging	55
5.3	“Coherent” Nonlinear Equations	58
5.4	Structure of the Minimization Problem and Choice of Starting Points	63
5.5	Model Example	66
5.5.1	Measurement Procedure	67
5.5.2	Solution of the Nonlinear Equations	68
6	Numerical Results	72
6.1	Absorption Effects	72
6.2	Large Absorption/Noise Values	76
6.3	Volumetric Imaging	78
7	Conclusions	80
A	The Lens	82
A.1	Paraxial Approximation	84
	Bibliography	86

List of Figures

2.1	Confocal microscopy system.	9
3.1	Data collection for CT.	18
3.2	The index of refraction (top) and absorption coefficient (bottom) for liquid water as a function of linear frequency [40]. The visible region of the frequency spectrum is indicated by the vertical dashed lines. The absorption coefficient for sea water is indicated by the dashed diagonal line at the left. Note the logarithmic scale in both directions.	29
4.1	Left: a non-planar layered structure. Right: Intensity of the scattered field resulting from an incident beam focused at a point indicated by the arrow on the left non-planar interface.	32
4.2	Optical coherence microscope.	33
4.3	Foci on the front and rear boundaries of a single-layer slab.	34
4.4	Measured results for thicknesses (black dots) and refractive indices (bars) versus the number of layers. The catalog values for thicknesses (long-and-short-dashed curves) and refractive indices (short-dashed curves) are also shown. The odd and even layers correspond to glass and air layers, respectively.	35
4.5	Scattering by a slab.	41
4.6	Display of the rays considered in Table 4.1 and, in the right bottom graph, the correction term of equation (4.32).	44
4.7	Display of the single reflection arising from the j -th layer for a normal incident beam.	46
4.8	Schematic display of coefficient $\alpha_{k,p}$, first realization.	46
4.9	Schematic display of coefficient $\alpha_{k,p}$, second realization.	46

4.10	Left: Refractive index distribution along a multi-layer structure of thickness 1 mm. Right: Display of the corresponding function $ \Sigma(\xi) $, as defined in equation (4.16), evaluated at 2200 sample positions ξ	47
4.11	Left: Display of $ \Sigma_1(\xi) $ evaluated at 2200 sample positions ξ . Right: Difference between Σ , (obtained by means of equation (4.16)), and Σ_1 , obtained by means of equation (4.33), as a function of ξ	48
4.12	Left: Display of $ \Sigma_2(\xi) $, as defined in equation (4.35), evaluated at 2200 sample positions ξ . Right: Difference between Σ (obtained by means of equation (4.16)) and Σ_2 (obtained by means of equation (4.35)) as a function of ξ	49
4.13	Left: Refractive index distribution along a multi-layer structure of thickness 1 mm. Right: Display of $\Sigma(\xi)$, defined by equation (4.16), evaluated at 2200 sample positions ξ	49
4.14	Left: Display of $ \Sigma_1(\xi) $, as defined by equation (4.33), evaluated at 2200 different positions of the sample. Right: Difference between Σ (obtained by means of equation (4.16)) and Σ_1 as a function of ξ	50
4.15	Left: Display of $ \Sigma_2(\xi) $, as defined by equation (4.35), evaluated at 2200 sample positions ξ . Right: Difference between Σ (obtained by means of equation (4.16)) and Σ_2 as a function of ξ	52
5.1	Left: Refractive index distribution. Right: Absorption distribution in blue. Absorption average in red, $\kappa = 0.9458e - 4$	58
5.2	Starting point for the scanning process.	59
5.3	Absolute value of the correlation function Σ as a function of ξ arising from the refractive index distribution displayed in Figure 5.1.	59
5.4	Left: Coarse sampled first spike in Figure 5.3. Right: Finely sampled first spike, with circles showing the coarse samples displayed on the left.	60
5.5	Left: Coarse sampled second spike in Figure 5.3. Right: Finely sampled second spike, with red circles showing the coarse samples displayed on the left, and with green circles showing coarse “aliased” samples providing data of very small numerical value, which is prone to be degraded by noise.	61
5.6	Mean-square function $\phi^q = \phi^q(n, d)$	62

5.7	Mean-square function $\phi^q = \phi^q(n, d)$: dark reds and dark blues indicate large and small function values, respectively.	63
5.8	Mean-square function ϕ^q for several values of the refractive index n	64
5.9	Mean-square function $\phi^q(n, d)$ as a function of d for several values of n	65
5.10	Two-layer structure with refractive indexes n_1 and n_2 and thickness d	66
5.11	Blue curve: Given refractive index distribution. Red: solution obtained by means of the minimization procedure detailed in this section.	71
6.1	Effect of absorption averaging. Upper left: Prescribed refractive index map. Upper right, lower left and lower right: reconstructions using values $\kappa = 0.6 \cdot 10^{-4}$, $\kappa = 0$ and $\kappa = 1.2 \cdot 10^{-4}$ for the average absorption parameter, respectively.	73
6.2	25-layer structure. Upper left: Refractive index distribution. Top right, bottom left and bottom right: Three different (random) absorption distributions.	74
6.3	25-layer structure. Refractive index distribution (blue) and the corresponding reconstruction for three different absorption values distributions.	74
6.4	50-layer structure. Upper left: Refractive index distribution. Top right, bottom left and bottom right: Three different (random) absorption distributions.	75
6.5	50-layer structure. Refractive index distribution (blue) and the corresponding reconstruction for three different absorption value distributions.	75
6.6	$ \Sigma $ for an absorption ranging between 10^{-4} and 10^{-3} . Top left: 25-layer structure. Top right: 50-layer structure. Bottom left and right: corresponding solutions for these absorption levels.	76
6.7	$ \Sigma $ for a noise level of the order of 10^{-3} relative to the maximum interference fringe intensity (which is of the order of 10^{-5}). Top left: 25-layer structure. Top right: 50-layer structure. Bottom left and right: corresponding solutions for these noise levels.	77
6.8	Left: Chessboard distribution of the original figure, with original color code. Center: Refractive index assignment. Left: reconstructions under assumption of lenses with numerical aperture of $N.A. = 0.054$	78
6.9	Same as Figure 6.8.	78
6.10	Same as Figure 6.8.	79
A.1	The lens.	82

List of Tables

4.1	The functions $g(\xi)$, calculated by direct evaluation of the integral (4.28), and $g^{trunc}(\xi)$, calculated from a truncated version of equation (4.30), with truncations as defined in the text. Here $n_1 = 1.4$ and $n_2 = 1.6$; $\tau = 2(\zeta - \xi)/c$	45
4.2	Convergence analysis: exact value $\Sigma = 0.0500432$. Here $\xi = \zeta$	45
5.1	Comparison of correlation values in two different bi-layer structures: 1) Layers contain materials of refractive indexes $N_1 = 1.4 + 10^{-4}i$ and $N_2 = 1.6 + 5 \cdot 10^{-4}i$; and 2) Layers containing materials of refractive indexes $N_3 = 1.4 + 3 \cdot 10^{-4}i$, $N_4 = 1.6 + 3 \cdot 10^{-4}i$, with absorptions equal to the average of the absorptions in N_1 and N_2	57
5.2	Five-layer structure.	67
5.3	Local minima obtained from the minimization process detailed in the text, and displayed by red circles in Figure 5.7.	68
5.4	Solution of the inverse problem with $\kappa = 0.9458e - 4$	70
6.1	Errors in n and d reconstruction.	73
6.2	Errors in n and d reconstruction.	76

Chapter 1

Introduction

The problem of imaging material bodies by means of waves and rays has had a tremendous impact on a wide variety of fields, including geology (e.g., providing support for oil and gas exploration as well as enhanced oil recovery operations); medicine (for medical diagnoses and treatment); biology (for anatomical and molecular investigations); military (humanitarian demining, remote sensing); atmospheric science (for evaluation and prediction of weather conditions); and materials science (imaging of solids at atomic length-scales), amongst many others. The imaging techniques used in these fields are manifold; in the biological and medical sciences, for example, we find magnetic resonance imaging, impedance computer tomography, ultrasound, X-ray computer tomography and emission computed tomography. Using a wide range of sources of lights and sound, the various imaging techniques available provide images at various levels of resolution, literally ranging from hundreds of kilometers in atmospheric applications, to a few microns in some of the most sophisticated biological applications, to a few nanometers in some materials science applications.

In this thesis we are concerned with a new technique, optical coherence tomography (OCT), which has thus far been used for imaging in biology/medical applications. This technique, which is based in interferometry, takes advantage of the low-coherence properties of diode-laser light sources to image selectively (and sequentially) prescribed points within a volumetric sample. Low coherence interferometric microscopes [35, 65] have been successful in producing internal images of thin pieces of biological tissue; typically samples of the order of 1 mm in depth have been imaged, with a resolution of the order of 10 to 20 μm in some portions of the sample. Such images have typically been produced through direct renderings of raw data: the intensities of certain interference fringes as functions of the position of the light-focus within the sample; quite generally, limited post-processing of this data has been

used.

In this work we address, in a mathematically rigorous manner, the inverse (Maxwell) problem of producing the actual values of the refractive index within a multi-layer sample from given low-coherence interferometric data. Once obtained, such a map of the refractive index variations may be useful in a variety of ways [65]; in particular, a straightforward display of this map yields an image of the internal structure of the sample. The advantages of an approach based on the Maxwell equations are manifold. Notably, such full-wave treatments allow for the consideration of various loss mechanisms such as scattering and absorption in a rigorous manner, and, thus, for production of images that remain faithful throughout the body of the sample. The results of this thesis have been announced in [8].

Our discussion is restricted to one-dimensional configurations; we thus relate our approach to some of the noted one-dimensional inverse problems and inverse-problem solvers for Maxwell's equations considered previously. As discussed in Section 3.4, existing methods [13, 27, 30] for solution of classical one-dimensional inverse problems for Maxwell's equations require use of wide wavelength bands, and are thus not applicable to many imaging problems arising in engineering/biological/medical applications. We show, in contrast, that using narrow light-wavelength bands, a certain OCT inverse problem we introduce allows for accurate rendering of refractive index distributions for rather general (thin and penetrable) samples. We expect that, through use of multiple points of collection of light, the present techniques will extend to cases in which layers are not planar, and, thus, to solution fully three-dimensional low-coherence inverse imaging problems.

1.1 Overview of Chapters

The remainder of this thesis is organized as follows. In Chapter 2 we review the history and development of the fields of microscopy and imaging. In Chapter 3 we discuss the basic elements of the theory of inverse problems, we describe the inverse problems arising in some of the imaging techniques mentioned in Chapter 2, and we present a discussion of previous inverse problem solvers—with emphasis on the previous work on the one-dimensional configurations which form the primary focus of this thesis. In Chapter 4 we focus on the OCT model and we present our strategy for solution of the associated direct problem. We show that, for a multi-layer structure, a rigorous geometrical optics method which takes

advantage of the coherence properties of OCT light-sources can be used to produce a fast direct-problem solver—as required by our inverse-problem algorithm. In Chapter 5 we then introduce our inverse solver and in Chapter 6, finally, we present a variety of numerical results.

Chapter 2

Microscopy

2.1 A Brief History of Microscopy

The first useful microscopes were developed in the Netherlands between 1590 and 1608; these first microscopes were simply tubes with lenses at each end. The magnification of these early scopes ranged from 3X to 9X, depending on the size of the diaphragm openings. The lens quality was often poor so the images were not very clear. Antony van Leeuwenhoek (1632-1723, Holland) built microscopes which gave magnifications up to 270 diameters. With this device he made some of the most important discoveries in biology. He discovered bacteria, sperm cells, blood cells and more. The English chemist, mathematician, physicist, and inventor Robert Hooke confirmed van Leeuwenhoek's discoveries of the existence of tiny living organisms in a drop of water. Hooke made a copy of Leeuwenhoek's microscope and then improved upon his design. Later, few major improvements were made until the middle of the 19th century. Present day instruments, changed but little, give magnifications up to 1250 diameters with ordinary light and up to 5000 with blue light. A light microscope, even one with perfect lenses and perfect illumination, cannot be used to distinguish objects that are smaller than half the wavelength of light. Since white light has an average wavelength of $0.55 \mu\text{m}$, any two lines that are closer together than $0.275 \mu\text{m}$ will be seen as a single line, and any object with a diameter smaller than $0.275 \mu\text{m}$ will be invisible, or, at best, show up as a blur. To see very small particles under a microscope, scientists must use a different sort of "illumination," one with a shorter wavelength. In 1934 Ernst Ruska described the construction of an electron microscope which filled the deficiencies of resolution of light microscope. In this kind of microscope, electrons are speeded up in a vacuum until their wavelength is extremely short, only one hundred-thousandth that of white light. Beams

of these fast-moving electrons are focused on a cell sample and are absorbed or scattered by the cell's parts so as to form an image on an electron-sensitive photographic plate. If pushed to the limit, electron microscopes can make it possible to view objects as small as the diameter of an atom. Most electron microscopes used to study biological material can "see" down to about 10 angstroms; although this does not make atoms visible, it does allow researchers to distinguish individual molecules of biological importance. Unfortunately, all electron microscopes suffer from a serious drawback: since no living specimen can survive the needed high vacuum, they cannot show the ever-changing movements that characterize a living cell.

It was Newton's observations of interference phenomena and Young's fundamental theory of interference in 1801 that provided the basis of what we know as interference microscope, see [58, p. 9]. In reference [49] Michelson (1852-1931) introduced an interferometer for light reflected from objects. Michelson's interferometer is the basis of the low-coherence interferometric techniques which underly the OCT microscopes, to whose mathematical study the present thesis is devoted.

2.2 Imaging Techniques

The wide variety of imaging techniques in existence arises from the corresponding diversity of useful energy sources, including light, microwaves, electrons, laser, X rays, ultrasound and nuclear magnetic resonance. The corresponding imaging length-scales range from molecular to geophysical, and the relative advantages and limitations of a given method depends on the way the corresponding energy interacts with the imaged medium. None of these techniques has prevailed over the others, and the selection of a particular one depends on the object to be imaged.

2.2.1 X Rays

Röntgen's discovery [57, p. 2] of X rays in 1895 opened a new era in the practice of medicine: it allowed visualization into the human body without pain or life-risk. However, X-ray imaging techniques have several important limitations. Small characteristic differences (1% to 2%) in X-ray attenuation are not detectable. A large percentage of radiation detected is scattered away from the body, thus reducing the signal-to-noise ratio of the recorded

information. And much detail is lost in the radiographic process due to the superposition of 3-D structural information into a 2-D detector. These problems were minimized with the development of X-ray computed tomography (early 1970s) [57, p. 5].

2.2.1.1 X-ray Computed Tomography (CT)

X-ray CT consists of determining the 2-D or 3-D distribution of tissue attenuation coefficients within the structure by means of mathematical reconstruction techniques based on the Radon inversion formula [57, p. 23]. 2-D images are obtained using a single X-ray tube which rotates 360° recording projections at every angular interval, which may vary between 0.5° to 1°. 3-D volume images can be constructed from a sequence of 2-D adjacent images. The spatial resolution in CT data ranges from 0.1 mm² to 1 mm² while the slice thickness ranges from 1 mm to 10 mm. The CT contrast resolution is in the range of 0.5%.

2.2.2 Magnetic Resonance Imaging (MRI)

Magnetic resonance imaging is an imaging technique used primarily in medical settings to produce high quality images of the inside of the human body [37]. The basic phenomenon of nuclear magnetic resonance has been known since the 1940s and MRI has been developed over the last 60 years. The largest component of the human body—about 75%—is water. A molecule of water (H_2O) is composed of two hydrogen (H) atoms and one oxygen (O) atom. The nucleus of each hydrogen atom consists of a single proton. Under normal conditions, these protons are constantly spinning, which envelopes them within a tiny magnetic field. Normally, this intrinsic magnetic field is randomly oriented. Under the action of an MRI scanner—which is essentially a very large and powerful magnet—the protons in a body line up either with or against the direction of the scanner’s own strong magnetic field. To make an image, pulses of radiowaves are directed at the area being examined through a special antenna. This knocks the protons off-balance, causing them to flip their orientation. When the pulse is turned off, the protons return back to their original positions. As they do so, they emit weak radio signals (the MR signal) of a particular frequency, which are analyzed by a computer and combined to create a series of cross-sectional images. 3-D volume images can be acquired using either 2-D multiple adjacent slice techniques or true 3-D volume acquisitions. The spatial resolution in plane ranges from 0.5 mm to 1 mm. MRI contrast is greatest in soft tissue, detecting 5% differences in signals [57, p. 26].

2.2.3 Confocal Fluorescence Microscopy

In a confocal microscope system, the specimen is not uniformly illuminated throughout its depth. The light is focused on a spot on one volume element of the specimen at a time, and the fluorescent light emitted from this spot is collected by a lens and focused on a pinhole screen blocking light from points out of the focal plane. By scanning many thin sections through the sample, a very clean three-dimensional image of the sample can be built. In practice, the best horizontal resolution of a confocal microscope is about $0.2 \mu\text{m}$, and the best vertical resolution is about $0.5 \mu\text{m}$. One of the main difficulties of conventional light and fluorescence microscopy experiments is out-of-focus blur degrading the image, reducing image contrast and decreasing the resolution. Out-of-focus information often obscures important structures of interest, particularly in thick specimens. In a conventional microscope setup, not only is the plane of focus illuminated, but much of the specimen above and below this point is also illuminated at the same time. This results in out-of-focus blur from these areas above and below the plane of interest. When living specimens are imaged some serious difficulties may occur: Since the small confocal aperture blocks most of the light emitted by the tissue, including light coming from the plane of focus, the exciting laser must be very bright to allow an adequate signal-to-noise ratio. This bright light causes fluorescent dyes to fade within minutes of continuous scanning (photobleaching). Phototoxicity is also a problem. Excited fluorescent dye molecules generate toxic free-radicals. Thus, one must limit the scanning time or light intensity if one hopes to keep the specimen alive. See <http://www.neuro.gatech.edu/potter/2photon.html> for more details.

2.2.3.1 Two-Photon Excitation Fluorescence Microscopy

Two-photon microscopy has allowed the possibility of alleviating the problems addressed in Section 2.2.3 [63]; see also <http://www.neuro.gatech.edu/potter/2photon.html>. In two-photon laser scanning microscopy (TPM), two photons of low energy (half of the wavelength) join forces to excite a fluorophore which would require one photon of twice the energy otherwise. The probability of this to happen is very small and it has quadratic dependence on light intensity. This limits the excitation to a small volume near the aperture and therefore reduces rates for photochemical damage and improved resolution in images of extended samples. The advantages of using lower wavelength results in deeper penetration

of tissue.

2.2.4 Confocal Scanning Microscopy

The confocal microscope was invented by Minsky in 1961 [17, 19, 50]. In a confocal microscope, light from a laser is focused by an objective lens to a small spot on the specimen at the focal plane of the lens, see Figure 2.1. Light reflected back from the illuminated spot on the specimen is collected by the objective and is partially reflected by a beam-splitter to be directed at a pinhole placed in front of the detector. This confocal pinhole is what gives the system its confocal property, by rejecting light that did not originate from the focal plane of the microscope objective. Light rays from below the focal plane come to a focus before reaching the detector pinhole, and then they expand out so that most of the rays are physically blocked from reaching the detector by the detector pinhole. In the same way, light reflected from above the focal plane focuses behind the detector pinhole, so that most of that light also hits the edges of the pinhole and is not detected. However, all the light from the focal plane is focused at the detector pinhole and so is detected at the detector. This ability to reject light from above or below the focal plane enables the confocal microscope to perform depth discrimination and optical tomography. A true 3-D image can be processed by taking a series of confocal images at successive planes into the specimen and assembling them in computer memory.

2.2.5 Ultrasound

Ultrasound is sound with a frequency over 20,000 Hz, which is about the upper limit of human hearing. Dussik was the first person to publish information on the medical use of diagnostic ultrasound; see <http://www.ob-ultrasound.net/dussikbio.html#hyper>. Unlike other techniques reviewed in the present chapter, which involve electromagnetic waves, ultrasound techniques involve longitudinal mechanical waves. In ultrasound, a high frequency sound wave is plunged into the tissue being imaged. The sound waves travel into the tissue or body and are reflected from internal structures with different acoustic properties. Attenuation of the sound wave may occur with propagation. The time behavior or echo structure of the reflected sound wave is detected and the internal structures are determined from the echo delay [7]. The resolution of ultrasound imaging depends directly on the frequency of the sound waves that are used. Most often sound wave frequencies in clinical applications

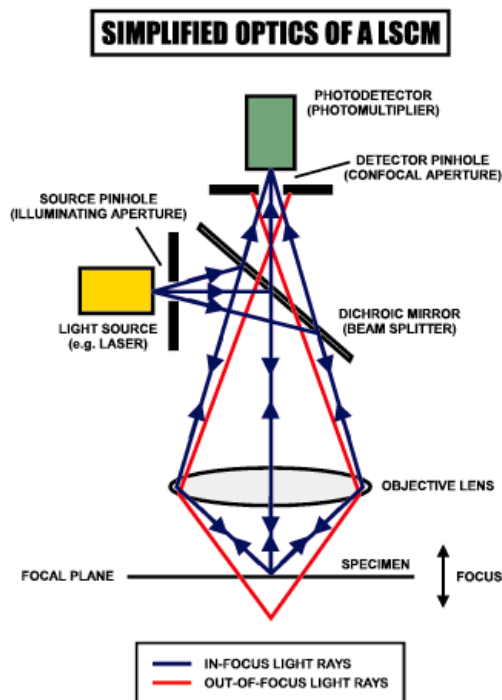


Figure 2.1: Confocal microscopy system.

are in the range of 10 MHz yielding spatial resolution up of $150 \mu\text{m}$. Resolution of the order of $15\text{-}20 \mu\text{m}$ was reached using much higher frequencies with the disadvantage that, since high frequencies are strongly attenuated for most biological tissue, this imaging is limited to depth of a few millimeters. On the other hand, frequencies in the range of 10 MHz are easily transmitted, allowing high penetration in tissue up to several tens of centimeters deep within the body. Use of ultrasound is not limited to medical applications: ultrasound techniques have important industrial applications. For instance, ultrasound is used to measure the viscosity and temperature of molten materials at very high temperatures, or to obtain concentration measurements, and ultrasonic mass flow measurement. [5, 20, 55]

2.2.6 Optical Coherence Tomography (OCT)

We can find the basis of what we know as interference microscope in Newton's observations of interference phenomena and Young's fundamental theory of interference [58, p. 10]. The earliest applications of low-coherence interferometric techniques were related to the detection of faults within fiber-optical cables and network components using optical-coherence domain reflectometry [28, 64, 68], but soon the technique found application in medical and

biological fields [34, 38, 60]. The basis of a low coherence interferometric microscope is a Michelson interferometer with a low-coherence light source (a super-luminescent diode). In an OCT microscope, 1) The sample to be imaged is placed in one arm of the interferometer, see Figure 4.2, and, 2) The light from the reference mirror (which is positioned at variable distances) and the light from the sample are correlated and detected. Since a light source of low coherence is used, the detector only responds to interferometric intensity fluctuations when the sample and the reference reflection have traveled through approximately the same optical lengths, thus giving information on the character of the scatterer to be found in a given position within the sample. Previous approaches to OCT imaging were based on rendering of the raw interference intensity maps to produce an image of internal structure of the sample. A detailed description of OCT tomography is presented in Chapter 4.

Additional information concerning the techniques described in the present Chapter 2 can be found in [7, 16, 17, 57–59].

Chapter 3

Inverse Problems

3.1 Introduction

Some of the most important mathematical problems arising in the imaging field belong to the general class of inverse problems. To preface our introductory history of inverse problems, I would like to bring to these pages the words of Reese T. Prosser in his review [54] of the book *Multidimensional Inverse Scattering Problems* by Alexander G. Ramm:

“The first postwar discussion of a recognizable inverse problem, in 1946, is due to Borg [6], who was concerned with the problem of recovering the density function for a one-dimensional vibrating string from a knowledge of its eigenfrequencies and eigenweights. Shortly thereafter there arose a considerable interest in determining the shape of certain nuclear potentials in quantum mechanics from measurements obtained from the scattering of elementary particle wave functions by these potentials. In 1949 Levinson [46] showed that the potential function which scatters a one dimensional particle is uniquely determined by the asymptotic phase of the particle wave function. In 1952 Jost and Kohn [42] gave a simple algorithm for constructing the potential function from the asymptotic phase. Meanwhile, in 1951 Gelfand and Levitan [27] produced a general method for recovering the potential function in the one-dimensional Schrödinger equation from the spectral data, and Marchenko [2] extended the method to include recovering the potential directly from the scattering data. All these attempts took on a renewed interest in the 1960s, when it was discovered by Gardner, Greene, Kruskal, and Miura [26] that the direct problem for the nonlinear Korteweg-deVries equation could be completely resolved by first resolving an associated

inverse problem for the linear Schrödinger equation. The inverse problem for the Schrödinger equation then took on all the aspects of a thriving cottage industry. The extension of these results to the more realistic and more interesting cases in higher dimensions has not come easily. The difficulties are all present in the prototype problem of the scattering in three dimensions of an elementary particle by a scalar potential. Mathematically, the problem can be briefly stated this way: Consider the time-independent Schrödinger equation

$$\nabla u(x) + k^2 u(x) - q(x)u(x) = 0; x \in R^3.$$

This equation governs the scattering in three dimensions of the quantum mechanical wave function $u(x)$ by the potential $q(x)$. The relevant solution $u(x)$ satisfies the associated integral equation

$$u(x, k) = \exp(ix \cdot k) - \int_{R^3} \frac{\exp(i|k||x - y|)}{4|x - y|} q(y)u(y, k)dy.$$

As $|x| \rightarrow \infty$, this solution has the asymptotic form

$$u(x, k) = e^{ik \cdot x} - T(k', k) \frac{e^{ikr}}{4\pi r} + O(1/r),$$

This form may be interpreted physically as consisting of an ingoing plane wave plus an outgoing spherical wave weighted by the “ T -matrix”

$$T(k', k) = \frac{1}{4\pi} \int_{R^3} e^{-ik' \cdot y} q(y)u(y, k)dy,$$

which embodies the measurable scattering information. Here k is the ingoing plane wave vector and k' is the outgoing scattered wave vector, with $r = |x|$ and $k = |k| = |k'|$. Writing $\theta = k/|k|$, $\theta' = k'/|k'|$, and $A(\theta', \theta, k) = T(k', k)$, we can state the relevant three-dimensional scattering problems as follows:

- The direct potential scattering problem: Given $q(x)$, find $A(\theta', \theta, k)$.
- The inverse potential scattering problem: Given $A(\theta', \theta, k)$, find $q(x)$.

The inverse potential scattering problem breaks naturally into several pieces:

- The uniqueness problem: Given $A(\theta', \theta, k)$, show that at most one potential $q(x)$ can give rise to $A(\theta', \theta, k)$.
- The characterization problem: Given $A(\theta', \theta, k)$, find conditions which guarantee that at least one potential $q(x)$ can give rise to $A(\theta', \theta, k)$.
- The existence problem: Given $A(\theta', \theta, k)$, show that at least one potential can give rise to $A(\theta', \theta, k)$.
- The stability problem: Show that small changes in the data $A(\theta', \theta, k)$ result in small changes in the potential $q(x)$.
- The reconstruction problem: Given $A(\theta', \theta, k)$, construct, analytically or numerically, at least one potential giving rise to $A(\theta', \theta, k)$.
- The partial data problem: Given some portion of $A(\theta', \theta, k)$, construct at least one potential $q(x)$ giving rise to that portion of $A(\theta', \theta, k)$.

None of these problems is easy, and most are still open.”

In Chapter 3.2 below we present a brief introduction to the main techniques generally used in the solution of inverse problems; in Chapter 3.3 we then provide a succinct description of the types of inverse problems arising in the fields biological, medicine and engineering.

3.2 Inversion Methods

Given an operator L_λ depending on the parameter λ and the equation

$$L_\lambda u = f, \tag{3.1}$$

we refer to the forward problem as the problem to solve u in (3.1) for a given λ and f [48].

Now, if we are given an Operator B such that

$$Bu = g, \tag{3.2}$$

then we refer to an inverse problem as the problem of finding λ from the system of equations (3.1) and (3.2) for given f and g .

As it happens, inverse problems are often “ill-posed”. To define the concept of ill-posedness let A be a general map from a Hilbert space X into a Hilbert space Y . Then, the equation

$$Ax = b \tag{3.3}$$

is called well-posed if

1. the equation is solvable for each b ,
2. the solution x is uniquely determined, and
3. the solution x depends continuously on b .

Otherwise, the equation is said to be ill-posed.

Most imaging problems are ill-posed. They commonly fail to satisfy condition (3) , which leads to instability, i.e., a small data error δ in b can lead to a large error in the computed solution x . Knowledge of information about the function x such as smoothness and size might be used to enhance the stability of the problem. Denoting by $b^\delta = b + \delta$, a regularization method is any method that computes from b^δ and from a knowledge of a set $M \subseteq X$ where the solution must lie, an element $x^\delta \in M$ such that $\|x - x^\delta\| \leq \epsilon(\delta)$ with $\epsilon(\delta) \rightarrow 0$ as $\delta \rightarrow 0$. Following [48], we summarize some common regularization methods

1. The Tikhonov-Phillips Method
2. The Truncated Singular Value Decomposition
3. Iterative Methods
4. Regularization by Discretization
5. Maximum Entropy

3.2.1 The Tikhonov-Phillips Method

This regularization method [66] seeks the minimizer x^δ of

$$\min_{x \in X} \left\{ \|Ax - b^\delta\|_Y + \alpha \|x\|_X \right\},$$

where $\alpha > 0$ is a suitably chosen “regularization parameter.” If the operator A is linear [52], then

$$x^\delta = (A^*A + \alpha I)^{-1}A^*b,$$

where A^* is the adjoint of A . Application of this technique in medical imaging can be found in [51, 53, 56]. Other applications of this technique can be found such as to determine the particle size distribution of latex [23] or to estimate the relaxation spectrum of viscoelastic materials [22].

3.2.2 The Truncated Singular Value Decomposition

The idea of this technique consists of expressing the approximate solution x^δ by

$$x^\delta = \sum_{k, \sigma_k \geq \sigma} \frac{1}{\sigma_k} (b^\delta, b_k) x_k,$$

where x_k, b_k are orthonormal systems in X, Y , respectively, and σ_k are the singular values of the operator A and its adjoint A^* , i.e.,

$$Ax = \sum_{k=1}^{\infty} \sigma_k (x, x_k) b_k,$$

$$A^*x = \sum_{k=1}^{\infty} \sigma_k (b, b_k) x_k.$$

As pointed out in [47], the decay of the singular values σ_k is a measure for the ill-posedness of the operator. In most cases this technique is too expensive to provide an efficient practical reconstruction method, but on the other hand, it is a very valuable tool for analysis. An example of the application of this technique can be found in [61].

3.2.3 Iterative Methods

The term “iterative method” refers to a wide range of techniques that use successive approximations to obtain more accurate solutions to a linear system at each step. Iterative methods act as regularization if the iteration is stopped early enough. As indicated in [47], iterative methods compute first the contributions to large singular values and thus, the smoother part of the solution. Iterative techniques that seek to minimize the defect $\|Af - g\|$ with respect to f can be used in the nonlinear context as well, and, thus, such methods can be

applied to the (typically nonlinear) imaging problems [47]. With a finite set of data $g \in \mathbb{R}^M$ and $f \in \mathbb{R}^N$ we write

$$\phi(f) = \frac{1}{2} \sum_{m=1}^M F_m^2, \quad (3.4)$$

where $F_m = [(Af)_m - g_m]$, and (for sufficiently smooth operators $A : \mathbb{R}^N \rightarrow \mathbb{R}^M$) expand it in the form

$$\phi(f+v) = v \cdot \nabla \phi(f) + \frac{1}{2} v \cdot H(f)v + (\|v\|^3), \quad (3.5)$$

where $\nabla \phi(f) = J_A(f)^T F$, $J_A(f)_{mn} = (\partial(Af)_m / \partial f_n)$ is the Jacobian matrix of the operator A and where, defining for a given function $h(\vec{x})$, $[\nabla^2 h]_{ij} = (\partial^2 h / \partial x_i \partial x_j)$, we have set

$$H(f) = J_A(f)^T J_A(f) + \sum_m^M (Af - g)_m \nabla^2 (Af)_m.$$

Seeking minimization of the second order approximation by means of Newton's methods we obtain the algorithm

$$f_{k+1} = f_k + v^k, \quad (3.6)$$

where v^k is the solution of the system

$$H(f^k)v^k = -\nabla \phi(f^k). \quad (3.7)$$

To avoid evaluation of second derivatives one can approximate the Hessian (3.7) by $H(f) \approx \phi'^T \phi'$ arguing that F is sufficiently small near the solution. The Newton-type method resulting from this simplification is referred to as the "Gauss-Newton" method; see also [11] and Section 5.3. Examples of iterative methods applied to imaging techniques can be found in [45].

3.2.4 Regularization by Discretization

This method of regularization [48] consists of approximating the operator A in (3.3) by a discretization A_h of A with step-size h in such a way that if $h \rightarrow 0$ then $A_h \rightarrow A$ in some sense. Since A^{-1} is not continuous, the solution g_h of the equation

$$f_h = A_h^{-1} g_h, \quad (3.8)$$

will not converge to a good approximation of the solution f when the procedure is applied to g^δ . However, with a suitable election of $h = h(\delta)$

$$f^\delta = A_{h(\delta)}^{-1} g_{h(\delta)}, \quad (3.9)$$

may be made to satisfy $\|f - f^\delta\| < \epsilon(\delta)$. Often the discretization is performed by projecting on finite dimensional subspaces. Applications of this technique to problems of medical imaging can be found in [4].

3.2.5 Maximum Entropy

This method searches for minimizers f_δ of the problem

$$\min_{f \in X} \left\{ \|Af - g^\delta\|_Y + \alpha \Omega(f) \right\},$$

where $\Omega(f)$ is given by

$$\Omega(f) = - \int f(x) \log |f(x)| dx.$$

The minimization problem is then solved by means of iterative methods. This is applied for example in positron-emission tomography, see [33].

3.3 Inverse Problems Arising in the Imaging Field

3.3.1 X-Ray CT - Radon Transform

To describe the CT imaging problem, let us consider a domain $\Omega \in \mathbb{R}^2$ and the linear attenuation coefficient $a(x, y)$ defined on Ω . If I_0 is the intensity of the source and I the intensity transmitted along the ray L , then

$$I = I_0 e^{-\int_L a(x,y) dL}. \quad (3.10)$$

The mathematical problem in transmission tomography is to determine a from measurements of I for a large set of rays L [48]. If L is the straight line connecting the source

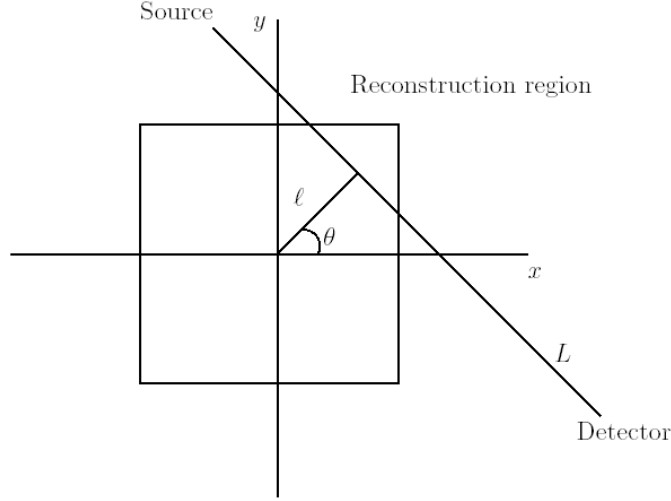


Figure 3.1: Data collection for CT.

$X_0 = (x_0, y_0)$ and the detector $X_1 = (x_1, y_1)$, then we have

$$\log \left(\frac{I}{I_0} \right) = - \int_0^1 a((X_0 - X_1)s + X_0) ds, \quad (3.11)$$

which is a reparametrization of the Radon Transform R defined by [32]

$$[R\hat{a}](\ell, \theta) = \int_{-\infty}^{\infty} \hat{a}(\sqrt{\ell^2 + z^2}, \theta + \tan^{-1}(z/\ell)) dz, \quad (3.12)$$

where $\hat{a}(r, \phi) = a(r \cos \phi, r \sin \phi)$ is the attenuation coefficient in polar coordinates. Here ℓ denotes the distance of the straight line L to the origin of coordinates and θ denotes the angle that the perpendicular to L forms with the positive x axis, see Figure 3.1.

The input data to a reconstruction algorithm are estimates of the values of $[R\hat{a}](\ell, \theta)$ for a finite number of pairs (ℓ, θ) ; its output is an estimate of \hat{a} . The inverse operator for the Radon Transform we are looking for is given by

$$[R^{-1}p](r, \phi) = \frac{1}{2\pi^2} \int_0^\pi \int_{-E}^E \frac{1}{r \cos(\theta - \phi) - \ell} \frac{\partial p(\ell, \theta)}{\partial \ell} d\ell d\theta, \quad (3.13)$$

where $p(\ell, \theta) = 0$ if $|\ell| < E$. It is important to note that for the reconstruction problem we need a discrete version for this inverse operator, see [32].

3.3.2 Ultrasound Computed Tomography

Consider an object Ω with refractive index n which is probed by a plane wave with wavelength λ and wave number $k = 2\pi/\lambda$, $u_\theta = e^{ikx \cdot \theta}$, traveling in the direction given by the unit vector θ . The total field $u(x) = u(x, \theta)$ satisfies the Helmholtz equation

$$\nabla u + k^2(1 + m)u = 0, \quad m = n^2 - 1,$$

and the scattered field $u - u_\theta$ satisfies radiation condition at infinity. The inverse problem to be solved is as follows: Given

$$u(x, \theta), \quad \theta \in S^2$$

for x on a certain surface outside Ω , determine m within Ω .

Most solvers for this problem are based on linearization, such as those given by the Born and Rytov approximations [48]. The Born approximation assumes that the field inside the body can be approximated by the incident field and leads to the linear integral equation

$$u(x, \theta) = u_\theta - k^2 \int_{\Omega} G(x - y)m(y)dy, \quad x \notin \Omega \quad (3.14)$$

for m , where G is the 3 dimensional Green function

$$G(x) = \frac{e^{ik|x|}}{4\pi|x|}.$$

Unfortunately, the assumptions underlying the Born and Rytov approximations are not satisfied in medical imaging since they do not take into account multiple reflections events which are of considerable relevance in scattering from biological tissues. Thus, the reconstructions of m obtained from solving the integral equation (3.14) can be of relatively poor quality [48, p. 96].

3.3.3 Optical Tomography

Optical tomography is an imaging technique which seeks to recover the spatial distribution of tissue absorption and scattering parameters in the near-infrared and optical wavelength range from surface measurements of light transmission [48]. The process is described by the

(Boltzman) transport equation

$$\frac{\partial u(x, \theta, t)}{\partial t} + \theta \cdot \nabla u(x, \theta, t) + a(x)u(x, \theta, t) = b(x) \int_{S^2} \eta(\theta \cdot \theta') u(x, \theta', t) d\theta' + f(x, \theta, t)$$

for the density $u(x, \theta, t)$ of photons at $x \in \Omega$ flying in the direction $\theta \in S^2$ at time t . The constants a and b are tissue parameters. The scattering kernel η is assumed to be known and f is the source term. The initial and boundary conditions are given by

$$\begin{aligned} u(x, \theta, 0) &= 0 \text{ in } \Omega \times S^2 \\ u(x, \theta, t) &= 0 \text{ on } \partial\Omega \times S^2 \times R, \quad \nu_x \cdot \theta \leq 0. \end{aligned}$$

The inverse problem arising from this model seeks to determine the tissue parameters a and b from a given outward radiation

$$g(x, \theta, t) = u(x, \theta, t) \text{ on } \partial\Omega \times S^2 \times R, \quad \nu_x \cdot \theta \geq 0.$$

Some of the best-known numerical methods for the solution of this inverse problem are of iterative type, where iterations are either applied directly to the transport equation or to its so-called diffusion approximation—which is an approximation to the transport equation by a parabolic differential equation. Unfortunately the inverse problems for equations of this type are very ill-posed. An extensive review of the methods developed to solve the transport inverse problem can be found in the references [3] and [4]. A study of the advantages of incorporating prior information to the reconstruction process is given in [62]. Quasi-Newton methods to the solution of the inverse problem are studied in [45].

3.4 1-D Inverse Problem for the Helmholtz Equation

The Helmholtz equation governs a variety of physical phenomena related to propagation of acoustic and electromagnetic waves [14, 44], and, it has thus come to be a centerpiece in a wide range of fields, including as medical diagnostics, non-destructive industrial testing, anti-submarine warfare, oil exploration, etc. [13]. As is well known, the inverse problem for the Helmholtz equation is highly nonlinear. In the one dimensional case, the problem can be reduced to a linear one, but the procedure is not stable numerically [27]. In this section

we present some of the inverse scattering solvers proposed previously for inverse problems associated with the Helmholtz equation

$$u'' + k^2 n(x)^2 u = 0, \quad (3.15)$$

and the closely related Schrödinger equation

$$u'' + k^2 u = V(r)u. \quad (3.16)$$

The scattering of a particle of energy $E = k^2$ by a *central* potential $V(r)$ (a function of $r = |\vec{r}|$) is governed by the three dimensional Schrödinger equation

$$\Delta u(\vec{r}) + Eu(\vec{r}) = V(r)u(\vec{r}), \quad (3.17)$$

which can be reduced to a sequence of one-dimensional (radial) Schrödinger equations expressing the solution u in terms of its spherical harmonics expansion,

$$\varphi_l'' + \left(E - \frac{l(l+1)}{r^2} \right) \varphi_l = V(r)\varphi_l, \quad (3.18)$$

The problem of determining $V(r)$ from scattering data has been the subject of very extensive studies. In what follows we discuss briefly the contributions introduced in [13, 27, 30].

Gelfand-Levitan method. In [27] the authors dealt with the problem of determining the potential $V(x)$ in the second order differential equation

$$y'' + (E - V(x))y = 0, \quad (3.19)$$

(defined on the interval $(0, \infty)$ with initial conditions $y(0) = 1$, $y'(0) = h$ and under the assumption that $V(x)$ is continuous) from a given spectral function $\rho(E)$ and the corresponding bound states. The spectral function $\rho(E)$ is a monotonic function, bounded on each interval, such that for any function $f(x)$ with integrable square the equation

$$\int_0^\infty f^2(x)dx = \int_{-\infty}^\infty \hat{f}(E)^2 d\rho(E)$$

holds, where

$$\widehat{f}(E) = \int_0^{\infty} f(x)\phi(x, E)dx,$$

and where $\phi(x, E)$ is the solution of equation (3.19) with the given boundary conditions. The bound states correspond to the solutions of (3.18) which satisfy the boundary conditions $\varphi(E, 0) = 0$, $\varphi'(E, 0) = 1$ and are square-integrable on the whole positive real axis.

The authors gave conditions ensuring the existence of a potential V that gives rise to a prescribed spectral function ρ , and they provided a method to compute $V(x)$ and h for a given admissible ρ . To do this the authors reduced the inverse problem to solution of a *linear* integral equation

$$g(x, y) + \int_0^x K(x, t)g(x, t)dt + K(x, y) = 0,$$

where

$$g(x, y) = \int_{-\infty}^{\infty} \cos(\sqrt{E}x) \cos(\sqrt{E}y) d\sigma(E),$$

and

$$\sigma(E) = \begin{cases} \rho(E) - \frac{2}{\pi}\sqrt{E}, & E \geq 0, \\ \rho(E) & E < 0. \end{cases}$$

Once the function K is known, the potential $V(x)$ and the initial condition h can be obtained:

$$V(x) = 2 \frac{dK(x, x)}{dx}$$

and $h = K(0, 0)$.

We emphasize that the spectral function is related to the phase-shift δ_0 of the wave function φ_0 and which is a function of the energy E and which is a measurable quantity. Thus, from knowledge of δ_0 it is possible to obtain $\rho(E)$ and then, following the steps detailed above, to determine the potential V . A more detailed description of this method is given in [12]. Marchenko modified the theory of Gelfand and Levitan making it possible to obtain the potential $V(x)$ directly from scattering data. Indeed, denoting $S(k) = \exp(2i\delta(k))$ and

$$A_0(t) = (2i\pi)^{-1} \int_{-\infty}^{\infty} [S(k) - 1] e^{ikt} dk,$$

Marchenko obtained a linear integral equation

$$A(r, t) = A_0(r + t) + \int_r^\infty A(r, s)A_0(s + t)ds, t > r,$$

from whose solution it is possible to obtain the potential V :

$$V(r) = -2\frac{dA(r, r)}{dr}.$$

It is possible to prove that Marchenko's theory is equivalent to Gelfand-Levitan's theory; see [12, p. 73].

Integral equation method. In reference [30] the author deals with an inverse problem of the form

$$\begin{aligned} y''(x) + \frac{\omega^2}{v(x)^2}y(x) &= 0 \\ y'(0) + \frac{i\omega}{v(0)}y(0) &= 2i\omega \\ y'(1) - \frac{i\omega}{v(1)}y(1) &= 0, \end{aligned} \tag{3.20}$$

where the goal is to determine the unknown velocity v from data of the scattering field prescribed at a set of ω values. The procedure is the following: After the change of variables

$$\tau = \int_0^x v(s)^{-1}ds,$$

a new formulation of the problem is obtained:

$$\begin{aligned} \left(\frac{u'}{c}\right)' + \frac{\omega^2 u}{c} &= Lu = 0 \\ [u' + i\omega u](0) &= 2i\omega \\ [u' - i\omega u](1) &= 0, \end{aligned}$$

where $u(\tau) = y(x(\tau))$ and $c(\tau) = v(x(\tau))$. Then, noting that the operator L depends on c explicitly the problem can be expressed as the integral equation for c :

$$\int_0^1 uLu_i = \int_0^1 (u_i + u_s) Lu_i = -2i\omega u_s(0; \omega), \tag{3.21}$$

where $u_s = u - u_i$. The values of $u_s(0; \omega)$ for the set of $\omega_j = j\pi/2 = k_j/2$ are our known data. The most general approach to obtain a solution of equation (3.21) considers the operator $L_0 v = v'' + \omega^2 v = 0$ and $u_i = e^{i\omega\tau}$ and thus, equation (3.21) can be written as

$$\int_0^1 e^{i\omega\tau} (i\omega e^{i\omega\tau} + u'_s) \gamma(\tau) d\tau = 2i\omega u_s(0; \omega), \quad (3.22)$$

where $\gamma = c'/c$ or

$$i\omega \int_0^1 e^{2i\omega\tau} \gamma(\tau) d\tau = 2i\omega u_s(0; \omega) - \int_0^1 \gamma(\tau) u_s(\tau, \omega) e^{i\omega\tau} d\tau. \quad (3.23)$$

Now, assuming that $c'(0) = c'(1) = 0$ so that the sine series of γ is appropriate, dividing by $i\omega$, taking the imaginary part and setting the set $\omega = \omega_k = k\pi/2$ the author gets

$$\int_0^1 \gamma \sin k\pi\tau d\tau = 2Im(u_s(0; \omega_k)) + \frac{1}{\omega_k} Re \left(\int_0^1 \gamma u'_s(\tau; \omega) e^{ik\pi\tau/2} d\tau \right) = B_k/2, \quad (3.24)$$

where B_k represents the coefficients in

$$\gamma(\tau) = \sum_1^{\infty} B_k \sin k\pi\tau.$$

Note that the B_k are not directly available since the integral in the right hand side involves the unknown γ . The author uses iteration to tackle this problem. First, he considers equation (3.24) without the integral term, i.e.,

$$\int_0^1 \gamma \sin k\pi\tau d\tau = 2Im(u_s(0; \omega_k)),$$

and he obtains

$$\gamma_0(\tau) = 4 \sum_1^N Im(u_s(0; \omega_k) \sin k\pi\tau), \quad (3.25)$$

$$c_0(\tau) = \exp \left(\frac{4}{\pi} \sum_1^N Im(u_s(0; \omega_k)) (1 - \cos k\pi\tau) / k \right). \quad (3.26)$$

Then using (3.25) and (3.26) in (3.24) it is possible to compute B_k and thus obtain a new γ and a new c by means of

$$\begin{aligned}\gamma(\tau) &= \sum_1^N B_k \sin k\pi\tau, \\ c(\tau) &= \exp\left(\frac{1}{\pi} \sum_1^N B_k (1 - \cos k\pi\tau) / k\right).\end{aligned}$$

This process is continued to convergence.

Spline projection method. In the article [18] the authors seek an approximation to the function $n(x)$ such that, given the reflection coefficient $R(\omega)$ of the corresponding layered structure, the solution $u(x)$ of the boundary value problem

$$\begin{aligned}u''(x) + \omega^2 n(x)^2 u(x) &= 0 \\ u'(0) + i\omega n_0(0)u(0) &= 2in_0\omega \\ u'(1) - i\omega n_0(1)u(1) &= 0,\end{aligned}\tag{3.27}$$

satisfies $u(0) = 1 + R(\omega)$ and $u'(0) = in_0\omega(1 - R(\omega))$ for all values of ω . The method, which assumes knowledge of a discrete set of values of $R(\omega)$, proceeds by approximating $n(x)$ using a k -th order spline expansion of the form

$$n(x) \approx \bar{n}(x) = \sum_i^N \lambda_i B_{i,k}(x).$$

This expansion leads to the solution of a non-linear system of equations in λ_i , which is solved by means of Levenberg-Marquardt algorithm. The authors show that this technique gives a certain degree of stability when sufficiently small noise errors are present in the measured data.

Techniques based on trace formulae. Trace formulae methods were introduced in reference [15] to study one-dimensional inverse quantum mechanical scattering problems in the line. In reference [13] the authors introduced trace formulae different from those of [15]; in what follows we discuss briefly the approach [13], which is more closely related than [15] to the imaging problems considered in this thesis.

In reference [13] the authors deal with the inverse problem for the one-dimensional scalar Helmholtz equation for electromagnetic scattering by a layered structure described by a (continuous or discontinuous) function $q = q(x)$:

$$\phi''(x, k) + k^2(1 + q(x))\phi(x, k) = 0. \quad (3.28)$$

To describe this inverse problem in detail, for each complex $k \in \mathbb{C}^+$ (= complex numbers with positive imaginary part) we consider the functions $\phi_+(x, k)$ (total field for left-to-right incidence) and $\phi_-(x, k)$ (total field for right-to-left incidence) given by

$$\begin{aligned} \phi_+(x, k) &= \phi_{inc+}(x, k) + \phi_{scatt+}(x, k) \\ \phi_-(x, k) &= \phi_{inc-}(x, k) + \phi_{scatt-}(x, k), \end{aligned} \quad (3.29)$$

where

$$\begin{aligned} \phi_{inc+}(x, k) &= e^{ikx} \\ \phi_{inc-}(x, k) &= e^{-ikx}, \end{aligned} \quad (3.30)$$

and $\phi_{scatt+}(x, k)$, $\phi_{scatt-}(x, k)$ satisfy the Helmholtz equation and the outgoing radiation boundary conditions

$$\begin{aligned} \phi'_{scatt+}(0, k) + ik\phi_{scatt+}(0, k) &= 0 \\ \phi'_{scatt-}(1, k) + ik\phi_{scatt-}(1, k) &= 0, \end{aligned} \quad (3.31)$$

respectively. Defining for $k \in \mathbb{C}^+$ the impedance functions

$$\begin{aligned} p_+(x, k) &= \frac{\phi'_+(x, k)}{ik\phi_+(x, k)} \\ p_-(x, k) &= \frac{\phi'_-(x, k)}{-ik\phi_-(x, k)}, \end{aligned} \quad (3.32)$$

the inverse problem under consideration is described as follows: given the values $p_+(0, k)$ of the impedance function at $x = 0$ for a finite number of frequencies $k_j = jh$, $j = 1, 2, \dots, N$ (where h is a positive constant), produce an approximation of the potential $q(x)$ in the interval $[0, 1]$.

In order to solve this problem the authors obtain the trace formulae

$$\begin{aligned} q'(x) &= \frac{2}{\pi}(1+q(x)) \int_{-\infty}^{\infty} (p_+(x,k) - p_-(x,k))dk \\ &\approx \frac{2}{\pi}(1+q(x)) \int_{-k_{max}}^{k_{max}} (p_+(x,k) - p_-(x,k))dk, \end{aligned} \quad (3.33)$$

and the Riccati equations

$$\begin{aligned} p'_+(x,k) &= -ik(p_+^2(x,k) - (1+q(x))), \\ p'_-(x,k) &= ik(p_-^2(x,k) - (1+q(x))), \end{aligned}$$

with initial conditions

$$\begin{aligned} p'_+(0,k) &= p_0(k), \\ p'_-(0,k) &= 1, \\ q(0) &= 0. \end{aligned}$$

This is an integro-differential system of equations for p_+ , p_- and q , which, as it is shown in [13], admits a unique solution for sufficiently large values of k_{max} . Further, this solution is stable with respect to small perturbations of the initial data $p_0(k)$.

In order to implement the algorithm it is necessary to select appropriate values for the truncation parameter k_{max} in equation (3.33); the authors use values ranging in the interval $5 \leq k_{max} \leq 100$ and they perform the integration using N_k integration points (wavenumbers) with $50 \leq N_k \leq 3200$.

Applicability of previous Helmholtz inverse solvers to imaging problems.

The inverse solvers described above in this section require knowledge of data in a wide frequency (energy) range, a requirement which may render them inapplicable to some of the most important engineering/medical configurations arising in practice. Indeed, the algorithm [13] described in the previous subsection, for example, uses values of the truncation parameter k_{max} of equation (3.33) in the range $5 \leq k_{max} \leq 100$ with wavenumber steps $0.1 \leq h_k \leq 0.2$ for $k_{max} = 5$ and $h_k = 0.1$ for $k_{max} = 100$. Even in the most favorable case, $k_{max} = 5$ and $h_k = 0.2$, we would have an infinite ratio of maximum to minimum wave number (if an

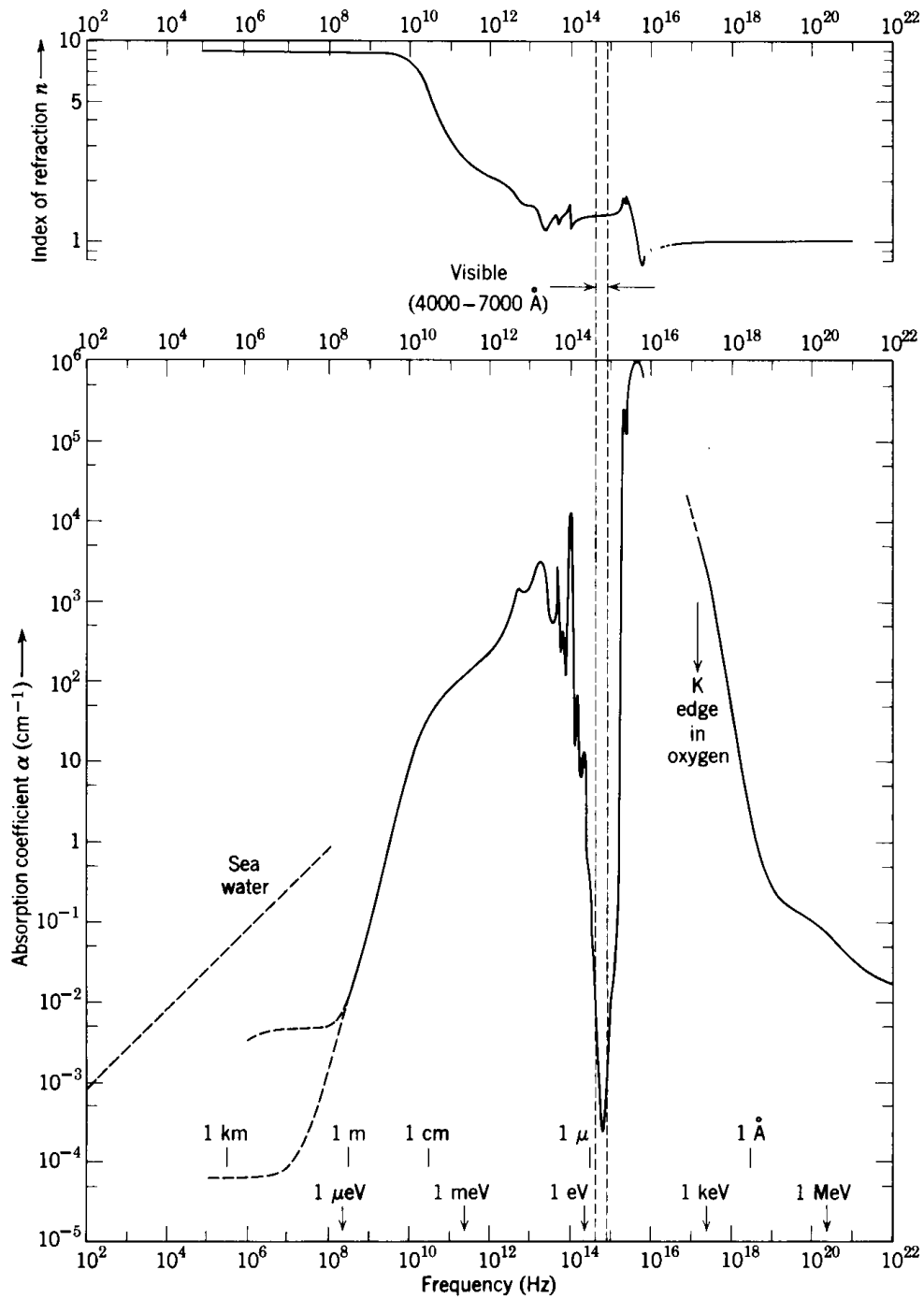
integration scheme centered at zero is used), or a ratio of $5/0.1 = 50$ —if the infinite ratio is avoided by integrating between, say, -4.9 and 5.1 with the same step $h_k = 0.2$. Thus, in the best possible scenario considered in [13] there is a factor of 50 between the lowest and largest wavenumbers used, and, thus, a corresponding factor of 50 between the largest and smallest wavelengths used. For the values $k_{max} = 100$ and $h_k = 0.1$ used in [13], in turn, the largest wavelength ratio is $100/0.05 = 2000$.

As is well known, unfortunately, both the absorption and the refractive index of materials depend very strongly on wavelength; the variation of these quantities for water, for example, is depicted in Figure 3.2. It is easy to see from this figure that, for imaging of biological bodies—in which water is a main component—for example, an inverse problem solver must only rely upon a range of frequencies restricted to the narrow wavelength band around the *visible band*—for which the absorption is very small, and for which the index of refraction is virtually constant. Indeed, use of light outside this narrow band (for which the combined effects of the orders-of-magnitude larger absorption losses and the uncertainties caused by the fast and large variations of the refractive indexes—which, in view of Figure 3.2 are certain to occur, but which, because of the presence of other materials in combination with water, are actually unknown), cannot provide any useful information about the internal structure of a water-based sample.

Clearly, the range of frequencies required by the algorithm of [13], in which the ratio of smallest to largest frequency is of the order of 50, cannot all be accommodated within any acceptable neighborhood of the $0.4\text{-}0.75\ \mu\text{m}$ visible band—nor within any region R of the spectrum satisfying the following three fundamental premises:

- R contains sufficiently short wavelengths—to resolve relevant features,
- Frequencies in R give rise to sufficiently small absorption—for adequate penetration, and
- Frequencies in R give rise to negligible refractive index variations for all of the materials making up the sample—without which the inverse problem is not determined.

Examination of tables of optical constants of materials [1, 43] suggests that, for most engineering/medical/biological configurations, involving e.g. water, semi-conductors, metals, glass, silicon, etc., the required set of three premises mentioned above is not satisfied in



XBL 751-58

Figure 3.2: The index of refraction (top) and absorption coefficient (bottom) for liquid water as a function of linear frequency [40]. The visible region of the frequency spectrum is indicated by the vertical dashed lines. The absorption coefficient for sea water is indicated by the dashed diagonal line at the left. Note the logarithmic scale in both directions.

any sufficiently large region, say, accommodating factors of 50 between largest and smallest frequencies used, which are required by the inverse solvers mentioned in this section.

As mentioned in the introduction to Chapter 1, in contrast, we approach the imaging problem through the solution of an *OCT inverse problem*, in which, given a set of fringe patterns, one seeks to obtain the distribution of refractive indexes within the sample. As discussed in Section 5.3 below, some of the most significant difficulties usually encountered in classical inverse problems can be eliminated in this context. Most importantly, the dominating light sources used in low-coherence interferometry techniques, SLDs (superluminescent light emitting diode), span the wavelength range from 675 nm to 1600 nm and have spectral widths up to 70 nm [21]. From Figure 3.2 we see that, for water, for example, this range of frequencies, which is only slightly larger than the visible, the absorption is small and the refractive index is virtually constant—so that, at least, sufficiently strong backscattering signals can be obtained for appropriately thin samples, and a meaningful inverse problem can be posed. The focus of this thesis is, precisely, to formulate this OCT inverse problem, and to provide a corresponding fast and accurate inverse problem solver for it.

Chapter 4

OCT Model and Direct Problem

4.1 Introduction

Optical coherence tomography (OCT) is a non-invasive imaging technique based on the use of light sources exhibiting a low degree of coherence. Low coherence interferometric microscopes [35, 65] have been successful in producing internal images of thin pieces of biological tissue; typically samples of the order of 1 mm in depth have been imaged, with a resolution of the order of 10 to 20 μm in some portions of the sample. Such images have been produced through renderings of the intensities of certain interference fringes as functions of the position of the light-focus within the sample; quite generally, limited post-processing of this data has been used. In this work we address, in a mathematically rigorous manner, the inverse (Maxwell) problem of producing, from given low-coherence interferometric data, the actual values of the refractive index within samples containing multiple parallel layers of various materials. Once obtained, such a map of the refractive index variations may be useful in a variety of ways; in particular, a straightforward display of this map yields an image of the internal structure of the sample. The advantages of an approach based on the Maxwell equations are significant. Notably, such full-wave treatments allow for the consideration of various loss mechanisms such as scattering and absorption in a rigorous manner, and, thus, to produce images that remain faithful throughout the body of the sample.

The importance of parallel-layer geometries is manifold: not only do they arise in a range of important engineering applications [25] (e.g., for quality control of transparent films of various materials), but also, certain techniques applicable to layered geometries, such as those presented here, should extend to more general configurations. We note that, when

layers are not planar, such as those shown in Figure 4.1 left, the techniques described in this thesis do not apply directly—since light is backscattered in a wide range of directions. (The scattered field for the curved geometry of Figure 4.1 was obtained using the fast, high-order integral equation solver of [10].) We expect that use of finite-element representations of surface layers and multiple points of collection of the light scattered by the sample will enable a generalization of the present techniques for evaluation of interface normals, and thus, for volumetric imaging of fully two- and three-dimensional bodies.

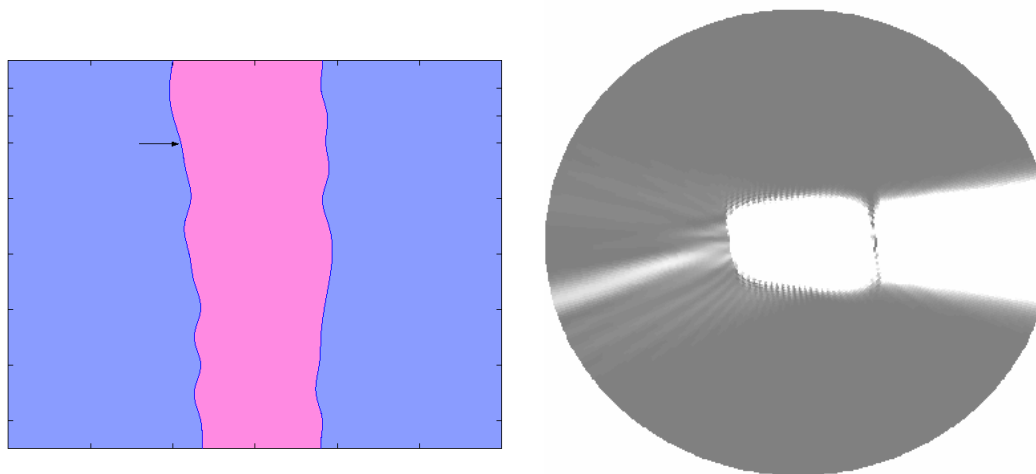


Figure 4.1: Left: a non-planar layered structure. Right: Intensity of the scattered field resulting from an incident beam focused at a point indicated by the arrow on the left non-planar interface.

The present theoretical/computational framework is developed for configurations such as those present in existing OCT devices [35, 36], see Figure 4.2. In those devices, single laser beams are focused by a lens at a point within the sample—in setup that gives rise to low numerical aperture. Various types of imaging techniques have been used in connection with OCT devices which, appealing to the low coherence properties of light, result in images of the interior of the sample. The actual inverse problem that yields from interference data the refractive index map, however, has not been considered before this work.

OCT devices have in fact been used in a few cases, however, for evaluation of refractive index maps in layered samples containing a small number of layers [24, 25, 65]. These methods which are based on approximate geometrical considerations and basic laws of geometrical optics, yield approximations to the thickness and the refractive index of each

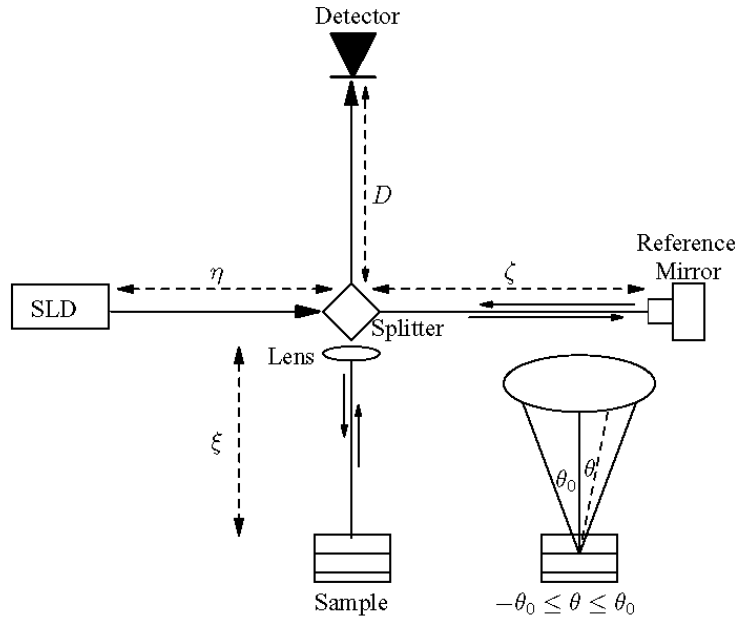


Figure 4.2: Optical coherence microscope.

layer within a layered structure from *two measured quantities*. In [24, 25], for example, the measured information used for thickness/index determination is the sample displacement required to obtain a *maximum reflected intensity* and the mirror displacement giving a *maximum for the interference fringe intensities*. Clearly, such methods depend heavily on accurate determination of such maxima at measurement time; accordingly, only structures consisting of the order ≈ 10 layers or less have heretofore been dealt with by means of such approaches.

The techniques [24, 25, 69] are all based on same mathematical principles, as summarized as follows; for simplicity, we restrict this description to a sample consisting of a single layer whose refractive index and width are to be found—the extension to multiple layers is straightforward. As indicated in the scheme of Figure 4.3 the light passing through the lens is first focused onto the front surface of the sample, and then the sample is moved toward the objective lens until the incident light is focused on the rear surface. Using Snell's law we have the first relation

$$n \sin \theta_1 = \sin \theta_0 = \text{NA}, \quad (4.1)$$

where NA is the numerical aperture of the lens. The distance between the first and the

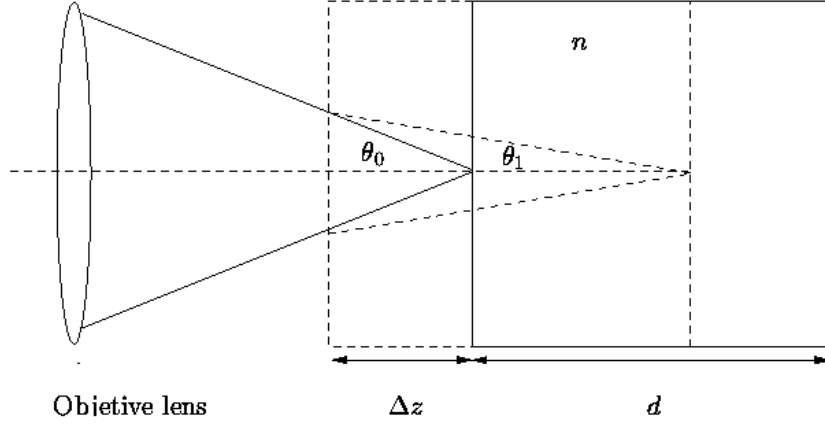


Figure 4.3: Foci on the front and rear boundaries of a single-layer slab.

second confocal points is given by

$$\Delta z \tan \theta_0 = d \tan \theta_1. \quad (4.2)$$

The change Δl in the optical path (under the paraxial approximation, in which all rays are considered parallel) is given by

$$\Delta l = nd - \Delta z. \quad (4.3)$$

Using these equations and the measured values of Δz and Δl it is possible to obtain the refractive index and the thickness by mean of the relations

$$n = \left(\frac{1}{2} \left\{ \text{NA}^2 + [\text{NA}^4 + 4(1 - \text{NA}^2)(1 + \Delta l/\Delta z)^2]^{1/2} \right\} \right)^{1/2}, \quad (4.4)$$

and

$$d = \frac{\Delta l + \Delta z}{n}. \quad (4.5)$$

Two different methods are used in [24, 25, 69] to measure the quantity Δl : the method of reference [24] is based on low-coherence interferometry (LCI), while those in [25, 69] use wavelength-scanning heterodyne interferometry (WSHI). In the first case, confocal microscopy is performed first: a beam of light is focused by a microscope objective onto the

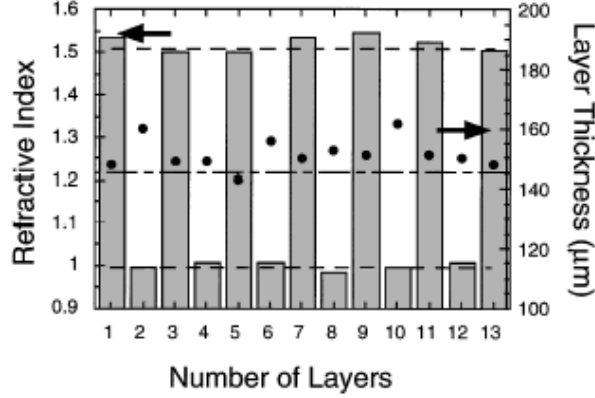


Figure 4.4: Measured results for thicknesses (black dots) and refractive indices (bars) versus the number of layers. The catalog values for thicknesses (long-and-short-dashed curves) and refractive indices (short-dashed curves) are also shown. The odd and even layers correspond to glass and air layers, respectively.

front surface of the specimen, see Section 2.2.4. Then, the reference mirror is moved to the position where the maximum contrast of the interference signal is obtained. Thus the optical path matching condition (OPMC) for both arms is satisfied. Next, confocal microscopy is performed again, the sample is moved closer to the objective until the peak of the confocal signal for the rear surface of the layer is found. The sample displacement given is denoted Δz . Now that the OPMC has been broken, it is necessary to move the reference mirror by Δl to attain the OPMC for the rear surface.

WSHI is based on the following principles: In a Michelson interferometer that has unbalanced arms with an OPD Δl , the frequency of the laser source is continuously tuned by $\Delta \nu$. The phase of the interference signal changes by $\Delta \varphi$, which is proportional to the OPD as

$$\Delta \varphi = \frac{2\pi \Delta l}{c} \Delta \nu,$$

where c is the speed of light. Therefore measuring the phase change $\Delta \varphi$ allows the OPD to be decided directly.

Figure 4.4 displays the results of [24]; we see the the refractive index values are reproduced fairly accurately. The layer thicknesses, in turn, suffer from a significant amount of dispersion and a tendency to be larger than the catalog values. Based on our numerical experiments, we propose that two approximations used by the authors should account for such disagreements: 1) neglect of absorption effects and 2) assumption that the incident

beam consists of parallel rays; compare Figure 4.3. The approximation 1) should be easy to compensate for. Improving modeling in connection with point 2), in turn, requires a modification of the complete analysis of 4.3—which, indeed, is based on this approximation in a substantial manner.

The technique introduced in this thesis accounts rigorously for all physical effects and, in particular, it does not rely on approximations such as 1) and 2). Even more importantly, our inverse problem solver produces solutions for inverse problems *from back-scattering interference fringes only*, and, unlike those of [24, 25, 69] *it does not require processing at data collection time*. Thus, our solver can produce solutions for inverse problems including thousands of layers. Our rigorous analysis and computational treatment, finally, results in *quantitatively accurate* renderings of the refractive index maps within the sample.

In this Chapter, we present the governing principles of the OCT technique and we formulate our fast algorithm for the solution of the direct problem. Our approach fully accounts for the statistical nature of the coherence phenomenon. The resulting model and direct problem solver are then used, in Chapter 5, as part of our OCT inverse problem solver.

4.2 Coherence

The OCT technique under consideration is based on use of a Michelson interferometer together with a low-coherence light source, as shown in Figure 4.2. As the sample to be imaged is placed in one arm of the interferometer, the light reflected from the reference mirror and the light backscattered from the sample are combined at the detector; the intensity of the interference fringes that result as the position of the sample is varied is the data from which the interior image of the sample is to be obtained.

The total optical intensity received by the detector D is given by [29]

$$I_D = \int_{S_P} \langle |u^{ref}(P, t) + u^{scatt}(P, t)|^2 \rangle_T dS_P = \int_{S_P} \langle |u^{ref}(P, t)|^2 \rangle_T + \langle |u^{scatt}(P, t)|^2 \rangle_T + 2Re \langle (u^{ref}(P, t))^* u^{scatt}(P, t) \rangle_T dS_P, \quad (4.6)$$

where $*$ denotes complex conjugate, P is a point on the detector, dS_P is the element of area on the detector, $u^{ref}(P, t)$ and $u^{scatt}(P, t)$ represent the fields back-scattered from the reference arm and the sample arm respectively, and where the symbol $\langle \dots \rangle_T$ denotes

time averages:

$$\langle G \rangle_T = \lim_{T \rightarrow \infty} \frac{1}{T} \int_{-T/2}^{T/2} G(t) dt.$$

Since the random processes associated with the emission of light are stationary and ergodic [21, 29], all the time averages we will encounter can be equated to ensemble averages,

$$\langle G(t) \rangle_T = \langle G(\omega) \rangle_\Omega.$$

Here $\langle G(\omega) \rangle_\Omega$ denotes ensemble averages over the space Ω of realizations: denoting by M is the probability measure we have

$$\langle G(\omega) \rangle_\Omega = \int_\Omega G(\omega) M(d\Omega).$$

In view of ergodicity, in what follows we thus identify time averages and ensemble averages, and we denote both of them by means of the symbol $\langle \dots \rangle$.

From equation (4.6) and since the reference intensity stays constant and the sample intensities vary slowly as the sample is moved, the interference fringes that appear in the light-intensity patterns can only result from the term

$$\Sigma = \int_{S_P} \langle \left(u^{ref}(P, t) \right)^* u^{scatt}(P, t) \rangle dS_P. \quad (4.7)$$

Clearly, Σ can be obtained by subtracting from I_D the sum

$$\int_{S_P} \langle |u^{ref}(P, t)|^2 \rangle dS_P + \int_{S_P} \langle |u^{scatt}(P, t)|^2 \rangle dS_P. \quad (4.8)$$

The intensities in equation (4.8) can be measured by closing the corresponding arm in the Michelson interferometer; e.g, the intensities

$$\int_{S_P} \langle |u^{scatt}(P, t)|^2 \rangle dS_P,$$

can be obtained by taking measurements with the reference arm closed.

We now seek to express Σ in terms of the statistical properties of the light source. To do this we denote by $u^{src}(P, x, z, t)$ and $A(P, x, z, \omega)$ the field emitted by the source and its

Fourier transform with respect to t , respectively:

$$\begin{aligned} u^{src}(P, x, z, t) &= \frac{1}{\sqrt{2\pi}} \int_{-\infty}^{\infty} A(P, x, z, \omega) e^{-i\omega t} d\omega, \\ A(P, x, z, \omega) &= \frac{1}{\sqrt{2\pi}} \int_{-\infty}^{\infty} u^{src}(P, x, z, t) e^{i\omega t} dt, \end{aligned} \quad (4.9)$$

where, for simplicity we assume $A(P, x, z, \omega) = \tilde{A}(P, \omega) e^{i\frac{\omega}{c}z}$; the case of general incidence can be treated analogously. Here c denotes the speed of light in vacuum.

The source beam travels through the source arm of the interferometer and, after passing through the splitter, gives rise incident fields

$$u^{inc}(x, z, t) = \frac{1}{2\sqrt{2\pi}} \int_{-\infty}^{\infty} \tilde{A}(P, \omega) \tilde{u}^{inc}(z, \omega) e^{-i\omega t} d\omega \quad (4.10)$$

on the sample and mirror arms, where $\tilde{u}^{inc}(z, \omega)$ denotes the plane wave

$$\tilde{u}^{inc}(z, \omega) = e^{i\frac{\omega}{c}z}. \quad (4.11)$$

The reference and sample backscattered fields at a point P of the detector are then given by

$$u^{ref}(P, t) = \frac{1}{4\sqrt{2\pi}} \int_{-\infty}^{\infty} \tilde{A}(P, \omega) \tilde{u}^{ref}(P, \omega) e^{-i\omega t} d\omega, \quad (4.12)$$

and

$$u^{scatt}(P, t) = \frac{1}{4\sqrt{2\pi}} \int_{-\infty}^{\infty} \tilde{A}(P, \omega) \tilde{u}^{scatt}(P, \omega) e^{-i\omega t} d\omega, \quad (4.13)$$

where $\tilde{u}^{scatt}(P, \omega)$ and $\tilde{u}^{ref}(P, \omega)$ are the backscattered field and the field in the reference arm arising from the incident field (4.11); note the factor $\frac{1}{2}$ which results as the reflected beams pass through the splitter a second time.

Substituting equations (4.12) and (4.13) into (4.7) we obtain

$$\Sigma = \frac{1}{32\pi} \int_{S_P} \int_{-\infty}^{\infty} \int_{-\infty}^{\infty} \langle \tilde{A}^*(P, \omega) \tilde{A}(P, \omega') \rangle \left(\tilde{u}^{ref}(P, \omega) \right)^* \tilde{u}^{scatt}(P, \omega') e^{i\omega t} e^{-i\omega' t} d\omega d\omega' dS_P.$$

But from (4.10) we have

$$\begin{aligned}
\langle \tilde{A}^*(P, \omega) \tilde{A}(P, \omega') \rangle &= \int_{\Omega} \tilde{A}^*(P, \omega) \tilde{A}(P, \omega') M(d\Omega) \\
&= \frac{1}{2\pi} \int_{-\infty}^{\infty} \int_{-\infty}^{\infty} \langle u^*(P, t) u(P, t') \rangle e^{i\omega t} e^{-i\omega' t'} dt dt' \\
&= \frac{1}{2\pi} \int_{-\infty}^{\infty} \int_{-\infty}^{\infty} \Gamma(t - t') e^{i\omega t} e^{-i\omega' t'} dt dt' \quad (4.14) \\
&= \frac{1}{2\pi} \int_{-\infty}^{\infty} \Gamma(\tau) e^{i\omega\tau} d\tau \int_{-\infty}^{\infty} e^{i(\omega - \omega')t} dt \\
&= S(\omega) \delta(\omega - \omega'),
\end{aligned}$$

where $\Gamma(\tau) = \langle u^*(P, t + \tau) u(P, t) \rangle$ is the self coherence function, and its Fourier transform $S(\omega)$ is the power spectral density of the optical field, respectively. (In passing we note that the last three identities in equation (4.14) in fact constitute a proof of the Wiener-Khinchin theorem [29].) Calling

$$g(P) = \frac{1}{16\sqrt{2\pi}} \int_{-\infty}^{\infty} S(\omega) \left(\tilde{u}^{ref}(P, \omega) \right)^* \tilde{u}^{scatt}(P, \omega) d\omega, \quad (4.15)$$

it follows that Σ can be expressed in terms of the power spectral density $S(\omega)$

$$\Sigma = \int_{S_P} g(P) dS_P, \quad (4.16)$$

which gives us the needed expression for Σ in terms of the statistical properties of the light source and the refractive properties of the sample under pure plane waves of the form (4.11).

As is commonly done, in our work we will assume a Gaussian Power Spectral Density of the form

$$S(\omega) = \frac{4\sqrt{\log(2)\pi}}{\Delta\omega} e^{-\left(2\sqrt{\log(2)} \frac{\omega - \bar{\omega}}{\Delta\omega}\right)^2},$$

whose complex degree of coherence is given by

$$\gamma(\tau) = e^{-\left(\frac{\Delta\omega\tau}{4\sqrt{\log(2)}}\right)^2} e^{-i\bar{\omega}\tau}. \quad (4.17)$$

Here, calling λ and $\Delta\lambda$ and c the center wavelength, the full-width at half-maximum (FWHM) and the speed of light respectively, $\bar{\omega} = 2\pi c/\lambda$ is the central angular frequency

and $\Delta\omega = 2\pi c\Delta\lambda/\lambda^2$ is the width of the spectrum line between the half-power points. In many of our concrete numerical examples we use the reasonable but otherwise arbitrary values $\lambda = 850$ nm, $\Delta\lambda = 70$ nm [21], together with the corresponding values of \bar{w} and $\Delta\omega$.

As mentioned above, our numerical method uses measured values of Σ to determine the distributions of refractive index within the sample, and, to do this, it requires an effective method for evaluation of Σ for a *prescribed* refractive index distribution. It is easy to see, however, that the numerical evaluation of Σ through direct integration of the expression (4.16) for each mirror and sample position would lead to inordinately long computing times. Fortunately, the low coherence property of the light allows us to obtain Σ in an extremely simple and fast manner—as explained in what follows.

4.3 Layered Media

The wave equation describing the propagation of linearly polarized TE waves in a dielectric medium is given by

$$\left[\frac{\partial^2}{\partial z^2} + \frac{\partial^2}{\partial x^2} + \omega^2 \mu \epsilon(z) \right] u(x, z) = 0, \quad (4.18)$$

where μ is the magnetic permeability (a constant throughout space for the non-magnetic samples under consideration) and $\epsilon = \epsilon(z)$ is the dielectric constant of the medium varying in the z direction, and where $u(x, z) = E_y(x, z)$ is the y -component of the electric field [14].

In the single-layer case (see Figure 4.5) with refractive index n_1 and thickness d_1 the solution of equation (4.18) in region 1 under an incident wave in the direction (α, β) , $u^{inc} = E_0 e^{i(k_x x + k_z z)} = E_0 e^{i\frac{\omega}{c}(\alpha x + \beta z)}$ is given by

$$u(x, z) = u^{inc}(x, z) + u^{scatt}(x, z),$$

where the reflected wave $u^{scatt}(x, z)$ (that is, the wave scattered by the sample in the backward direction) is given by [31]

$$u^{scatt}(x, z) = E_0 e^{i(k_x x - k_z z)} \left[r + \frac{r' t t' e^{i\delta_1}}{1 - r'^2 e^{i\delta_1}} \right]. \quad (4.19)$$

In equation (4.19) and in Figure 4.5 the parameters r , t , r' and t' denote Fresnel coefficients:

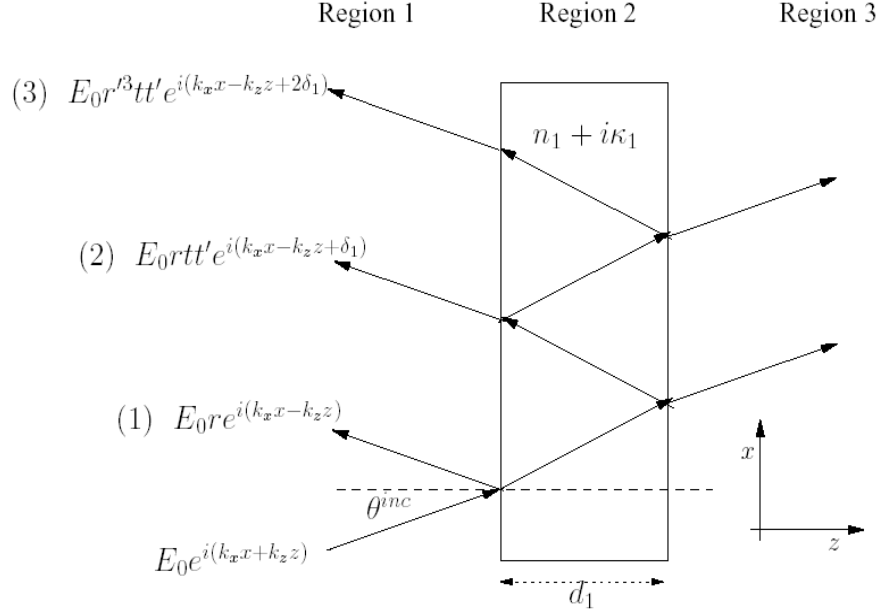


Figure 4.5: Scattering by a slab.

in the notation of equations (4.23) and (4.24) below these are given by $r = R_{0,1}$, $t = T_{0,1}$, $r' = R_{1,2} = -R_{0,1}$ and $t' = T_{1,0}$, with $n_0 = 1$, $\kappa_0 = 0$, and $n_1 + i\kappa_1$ equal to the refractive index of the layer. Further, calling θ^{trans} the *complex* transmission angle given by the complex form of Snell's law, $\sin(\theta^{inc})/\sin(\theta^{trans}) = n_1 + i\kappa_1$, the parameter δ_1 is given by

$$\delta_1 = 2n_1 d_1 \cos(\theta^{trans}) \omega/c. \quad (4.20)$$

If $\kappa_1 = 0$ then δ_1 is real, and it equals the optical path-length difference between adjacent rays—see, e.g., the rays (1) and (2) in Figure 4.5.

The scattered wave $u^{scatt}(x, z)$ may be viewed as the sum of contributions from an infinite number of reflections given by

$$\begin{aligned} E_{1r} &= E_0 r e^{i(k_x x - k_z z)}, \\ E_{2r} &= E_0 t r' t' e^{i\delta_1} e^{i(k_x x - k_z z)}, \\ E_{3r} &= E_0 t r'^3 t' e^{i2\delta_1} e^{i(k_x x - k_z z)}, \end{aligned}$$

$$\begin{aligned} & \vdots \\ E_{N_r} &= E_0 t r'^{(2N-3)} t' e^{i(N-1)\delta_1} e^{i(k_x x - k_z z)}, \end{aligned}$$

For a multi-layer film, in turn

$$u^{scatt}(x, z) = E_0 \tilde{R}_{0,1} e^{i(k_x x - k_z z)}, \quad (4.21)$$

where, calling θ_q^{trans} the q -th transmission angle, $\delta_q = 2n_q d_q \cos(\theta_q^{trans}) \omega/c$ and $\tilde{R}_{q,q+1}$ the generalized reflection coefficients at the interface between region q and region $q+1$ we have

$$\tilde{R}_{q,q+1} = \frac{R_{q,q+1} + \tilde{R}_{q+1,q+2} e^{i\delta_q}}{1 + R_{q,q+1} \tilde{R}_{q+1,q+2} e^{i\delta_q}}. \quad (4.22)$$

Here $R_{q,q+1}$ are the regular Fresnel reflection coefficient given by

$$R_{q,q+1} = \frac{(n_q + i\kappa_q) - (n_{q+1} + i\kappa_{q+1})}{n_q + i\kappa_q + n_{q+1} + i\kappa_{q+1}}. \quad (4.23)$$

It is appropriate to quote here the Fresnel transmission coefficients as well:

$$T_{q,q+1} = \frac{2(n_q + i\kappa_q)}{n_q + i\kappa_q + n_{q+1} + i\kappa_{q+1}}, \quad (4.24)$$

see e.g. [14].

4.4 Fast Evaluation of the Function Σ

For clarity in the exposition, in this section we assume

$$u^{inc}(x, z, \omega) = e^{ikz} = e^{i\frac{\omega}{c}z}, \quad (4.25)$$

where $k = 2\pi/\lambda = \omega/c$; it should be clear that an analogous treatment can be given for the case of general incidence. Such general cases have indeed been implemented as part of our direct and inverse problem solvers. Further, to motivate the introduction of our fast evaluation algorithm, we begin by considering a configuration for which the sample consists of a single homogeneous slab under the normally incident wave (4.25). The implications of this analysis on the multi-layer, multi-incidence-angle case are described towards the end

of this section.

Under the present single-layer, *normal-incidence* assumptions, it follows that the backscattering received from the sample at a point P on the detector is independent of P , and, for a fixed mirror position ζ , depends only on frequency and the position ξ of the sample:

$$\tilde{u}^{scatt}(P, \xi, \omega) = \tilde{u}^{scatt}(\xi, \omega) = \frac{1}{4} e^{ik(D+\eta+2\xi)+\pi i} \left[r + \frac{r'tt' e^{i\delta_1}}{1 - r'^2 e^{i\delta_1}} \right],$$

where η is defined in Figure 4.2, and r, r', t, t' and δ_1 are the Fresnel coefficients defined in Section 4.3. For the reflection from the mirror, on the other hand, we have

$$\tilde{u}^{ref}(P, \omega) = \tilde{u}^{ref}(\omega) = \frac{1}{4} e^{ik(D+\eta+2\zeta)+2\pi i} = \frac{1}{4} e^{ik(D+\eta+2\zeta)}, \quad (4.26)$$

where D, ζ and ξ are defined in Figure 4.2. The $2\pi i$ constant in the first exponent of equation (4.26) results from the two mirror reflections: one by the splitter mirror, the other by the reference mirror. The factor $\frac{1}{4}$, in turn, is due to the fact that light passes twice through the splitter.

Denoting

$$\tau = 2(\zeta - \xi)/c, \quad (4.27)$$

the function (4.15) for the present configuration is given by

$$g(P, \xi) = g(\xi) = -\frac{1}{16\sqrt{2\pi}} \int_{-\infty}^{\infty} S(\omega) \left[r + \frac{r'tt' e^{i\delta_1}}{1 - r'^2 e^{i\delta_1}} \right] e^{-i\omega\tau} d\omega,$$

or, in view of equation (4.20)

$$g(P, \xi) = g(\xi) = -\frac{1}{16\sqrt{2\pi}} \int_{-\infty}^{\infty} S(\omega) \left[r + \frac{r'tt' e^{i\omega t_1^{delay}}}{1 - r'^2 e^{i\omega t_1^{delay}}} \right] e^{-i\omega\tau} d\omega, \quad (4.28)$$

where $t_1^{delay} = \delta_1/\omega = 2n_1 d_1 \cos(\theta^{trans})/c = 2n_1 d_1/c$; more generally we define

$$t_q^{delay} = 2n_q d_q \cos(\theta_q^{trans})/c. \quad (4.29)$$

Note that, under our standing assumption that ζ is constant, the correlation Σ is a function of ξ only: $\Sigma = \Sigma(\xi)$; see equation (4.16).

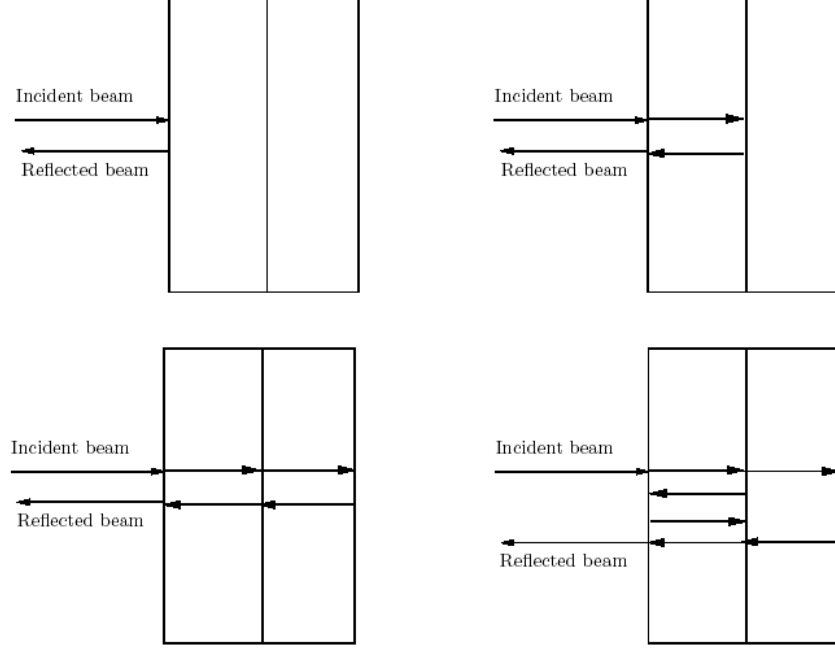


Figure 4.6: Display of the rays considered in Table 4.1 and, in the right bottom graph, the correction term of equation (4.32).

To simplify the evaluation of the integral in equation (4.28) we use a series expansion of the bracketed term in the integrand and we obtain

$$\begin{aligned}
g(\xi) &= -\frac{1}{16\sqrt{2\pi}} \left[r \int_{-\infty}^{\infty} S(\omega) e^{-i\omega\tau} d\omega + (r'tt') \int_{-\infty}^{\infty} S(\omega) e^{i\omega t_1^{delay}} e^{-i\omega\tau} d\omega \right] + \\
&- \frac{1}{16\sqrt{2\pi}} (r'^3 tt') \int_{-\infty}^{\infty} S(\omega) e^{i2\omega t_1^{delay}} e^{-i\omega\tau} d\omega + \dots + \\
&- \frac{1}{16\sqrt{2\pi}} (r'^{(2N-3)} tt') \int_{-\infty}^{\infty} S(\omega) e^{i(N-1)\omega t_1^{delay}} e^{-i\omega\tau} d\omega + \dots .
\end{aligned}$$

It follows that,

$$\begin{aligned}
g(\xi) &= -\frac{\sqrt{2\pi}}{16} \left[r\gamma(\tau) + (r'tt')\gamma(\tau - t_1^{delay}) \right] + \\
&- \frac{\sqrt{2\pi}}{16} (r'^3 tt')\gamma(\tau - 2t_1^{delay}) + \dots + \\
&- \frac{\sqrt{2\pi}}{16} (r'^{(2N-3)} tt')\gamma(\tau - (N-1)t_1^{delay}) + \dots , \tag{4.30}
\end{aligned}$$

where $\gamma(\tau)$ is the complex degree of coherence of the source

$$\gamma(x) = \frac{1}{2\pi} \int_{-\infty}^{\infty} S(\omega) e^{-i\omega x} d\omega.$$

As it happens, the series (4.30) converges extremely fast, and even its first term alone provides extremely accurate approximations in some cases. Its significance is easy to grasp: the j -th term in the series represents light backscattered after j bounces within the layer, with the weight factor $\gamma(\tau - jt_1^{delay})$ accounting for reduced contributions to the function Σ due to loss of coherence as j and, thus, the total optical paths increase. Analogous (albeit more complex) ray expansions can be obtained for any given number of layers and for arbitrary incidences.

Table 4.1: The functions $g(\xi)$, calculated by direct evaluation of the integral (4.28), and $g^{trunc}(\xi)$, calculated from a truncated version of equation (4.30), with truncations as defined in the text. Here $n_1 = 1.4$ and $n_2 = 1.6$; $\tau = 2(\zeta - \xi)/c$.

ξ	$g(\xi)$	$g^{trunc}(\xi), (C = -1/16\sqrt{2\pi})$
$\xi = \zeta$	0.0522212	$CR_{0,1}\gamma(\tau) = 0.0522214$
$\xi = \zeta - d_1^{opt}$	0.0203082	$CR_{1,2}T_{0,1}T_{1,0}\gamma(\tau - d_1^{opt}/c) = 0.0203083$
$\xi = \zeta - (d_1^{opt} + d_2^{opt})$	-0.0699794	$CR_{2,3}T_{0,1}T_{1,0}T_{1,2}T_{2,1}\gamma(\tau - 2(d_1^{opt} + d_2^{opt})/c) = -0.0699856$

To visualize the importance of these rapidly convergent ray expansions in our context we first analyze the convergence of the series (4.30) for a few significant examples. In our first example the sample is a structure consisting of two layers of width $d_1 = d_2 = 10 \mu\text{m}$ containing materials of refractive indexes $n_1 = 1.4$ and $n_2 = 1.6$ respectively. We denote by $d_1^{opt} = n_1 d_1$ and $d_2^{opt} = n_2 d_2$ their respective optical path lengths. Here as above, for simplicity in the exposition we assume a normal incident beam of the form $u^{inc}(x, z) = e^{ik_z z}$.

We will denote by $g^{trunc}(\xi)$ the various truncations we will introduce for the function $g(\xi)$. The reflected waves to be included in g^{trunc} will vary depending on the context.

Table 4.2: Convergence analysis: exact value $\Sigma = 0.0500432$. Here $\xi = \zeta$.

Ray expression ($C = -1/16\sqrt{2\pi}$)	Ray contribution	g^{trunc} (Cumulative)
$CR_{0,1}\gamma(0)$	0.0522214	0.0522214
$CR_{1,2}T_{0,1}T_{1,0}\gamma(-2d_1^{opt}/c)$	-0.00180599	0.0504154
$CR_{2,3}T_{0,1}T_{1,0}T_{1,2}T_{2,1}\gamma(-2(d_1^{opt} + d_2^{opt})/c)$	-0.000374135	0.0500413
$-CR_{0,1}R_{1,2}^2 T_{0,1}T_{1,0}\gamma(-2d_1^{opt}/c)$	$2.1392 \cdot 10^{-6}$	0.0500434

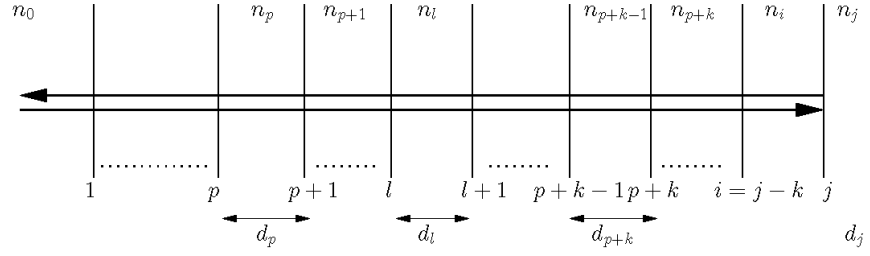


Figure 4.7: Display of the single reflection arising from the j -th layer for a normal incident beam.

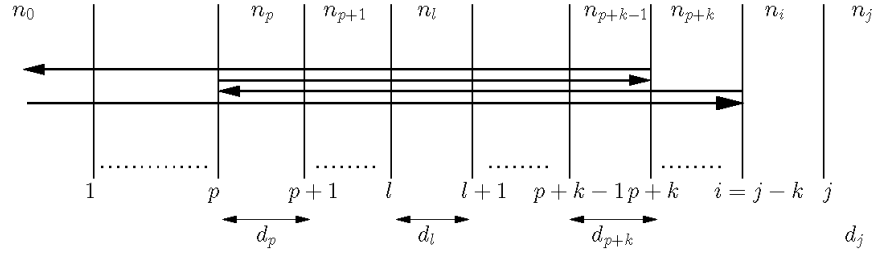


Figure 4.8: Schematic display of coefficient $\alpha_{k,p}$, first realization.

Table 4.1 contains values of the function g and various truncations g^{trunc} .

To define the relevant truncations g^{trunc} we note that, for the present two-layer structure we have

$$\begin{aligned}\tilde{u}^{scatt}(P, \omega) &= -\frac{1}{4}\tilde{R}_{0,1}e^{ik(D+\eta+2\xi)} \\ \tilde{u}^{ref}(P, \omega) &= \frac{1}{4}e^{ik(D+\eta+2\zeta)},\end{aligned}$$

where $\tilde{R}_{0,1}$ is given by equation (4.22). In this case equation (4.15) becomes

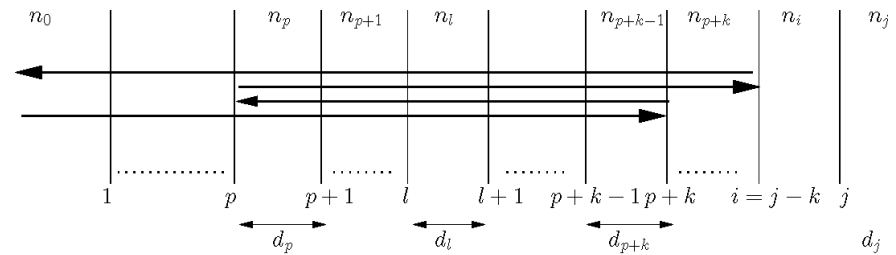


Figure 4.9: Schematic display of coefficient $\alpha_{k,p}$, second realization.

$$g(\xi) = -\frac{1}{16\sqrt{2\pi}} \int_{-\infty}^{\infty} S(\omega) \tilde{R}_{0,1} e^{-i\omega\tau} d\omega, \quad (4.31)$$

with $\tau(\xi)$ given by equation (4.27). As in the single layer case, this function may be viewed as a sum of contributions resulting from reflections of rays on the various interfaces, which are given, in turn, by the coefficients $R_{q,q+1}$ defined in equation (4.23) as well as the coefficients $T_{q,q+1}$ defined in equation (4.24).

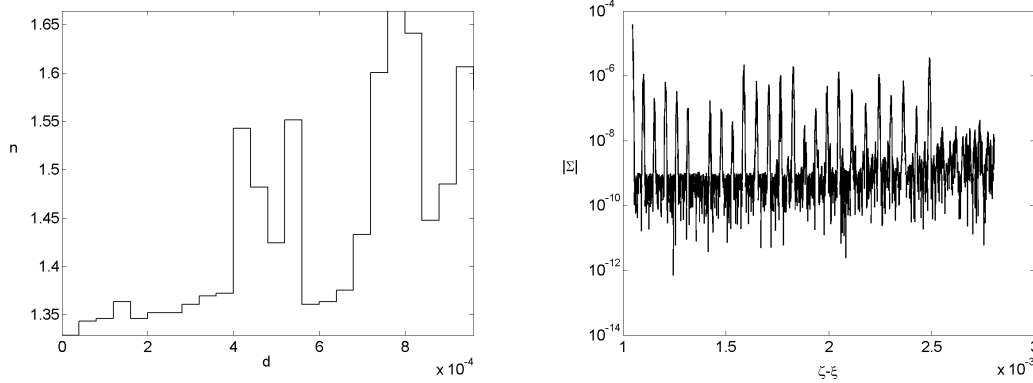


Figure 4.10: Left: Refractive index distribution along a multi-layer structure of thickness 1 mm. Right: Display of the corresponding function $|\Sigma(\xi)|$, as defined in equation (4.16), evaluated at 2200 sample positions ξ .

In rows 1), 2) and 3) of Table 4.1, the truncated function g^{trunc} includes contributions as follows: Row 1) The ray reflected into the detector directly from the first interface (with a contribution of $-1/16\sqrt{2\pi}R_{0,1}\gamma(0)$), see Figure 4.6, top left; Row 2) The portion of the ray reflected at the second interface which it transmitted back into the detector through the first interface (with a contribution of $-1/16\sqrt{2\pi}R_{1,2}T_{0,1}T_{1,0}\gamma(\tau - d_1^{opt}/c)$), see Figure 4.6, top right and; Row 3) The portion of the ray reflected at the third interface which then impinges on the detector after having been transmitted by both the second and first interfaces (with a contribution of $-1/16\sqrt{2\pi}R_{2,3}T_{0,1}T_{1,0}T_{1,2}T_{2,1}\gamma(\tau - 2(d_1^{opt} + d_2^{opt})/c)$), see Figure 4.6, bottom left.

The agreement between the exact (as calculated by direct evaluation of the integral (4.28)) and approximate expressions for g is excellent and, clearly, the approximate expression is much easier to evaluate: in every case we just need one term of the series to obtain the value of the integral (4.31) with an absolute error of the order of 10^{-5} . In the last row we

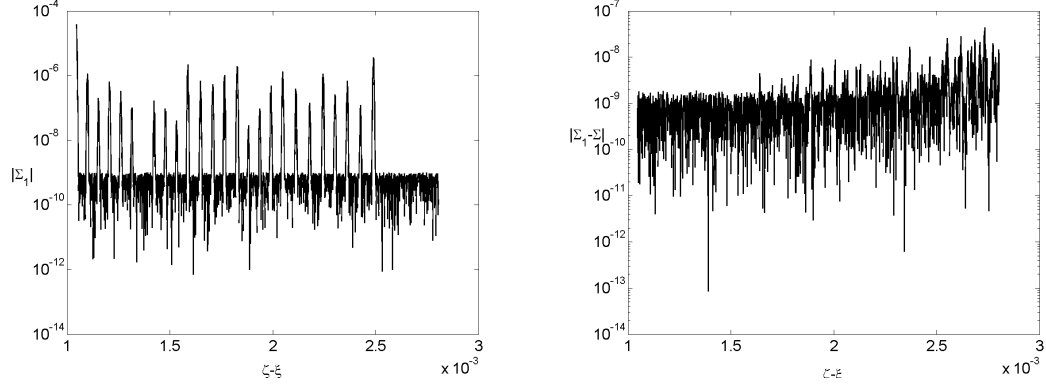


Figure 4.11: Left: Display of $|\Sigma_1(\xi)|$ evaluated at 2200 sample positions ξ . Right: Difference between Σ , (obtained by means of equation (4.16)), and Σ_1 , obtained by means of equation (4.33), as a function of ξ .

find the lowest accuracy; this approximation can be improved by adding the contribution of an additional reflection—so as to account for a multiple reflection within the first layer, see Figure 4.6, bottom right. The resulting improved approximation is

$$\begin{aligned}
 g^{trunc} &= -\frac{\sqrt{2\pi}}{16} \left(R_{2,3} T_{0,1} T_{1,0} T_{1,2} T_{2,1} \gamma (\tau - 2(d_1^{opt} + d_2^{opt})/c) \right) \\
 &+ \frac{\sqrt{2\pi}}{16} \left(R_{0,1} R_{1,2}^2 T_{0,1} T_{1,0} \gamma (\tau - 4d_1^{opt}/\omega) \right) = -0.0699794. \quad (4.32)
 \end{aligned}$$

Of course, to obtain the same accuracy for thinner layers it is necessary to either use more terms in the truncated function, or to reduce the coherence length of the source. Restricting ourselves to a fixed coherence length, we continue our convergence study by considering layers with reduced thicknesses: $d_1 = d_2 = 1 \mu\text{m}$. Again we use the values $n_1 = 1.4$ and $n_2 = 1.6$. For the purposes of this example we restrict ourselves to the case $\xi = \zeta$. In Table 4.2 we see that, indeed, the exact value $g = 0.0500432$ is approximated rapidly by the appropriate sequence of truncated g^{trunc} .

For a multi-layer structure the contribution of multi-reflections becomes more and more important as the number of layers increases. In what follows we show that a ray expansion is still possible even for samples containing a large number of layers.

To do this we proceed as follows: given a position ξ of the sample we compute $\tau = 2(\zeta - \xi)/c$ and we determine the value of j that minimizes the quantity $|\tau - \sum_{q=1}^{j-1} t_q^{delay}|$ amongst all j with $1 \leq j \leq N^{layers}$, where t_q^{delay} is given by equation (4.29). We then

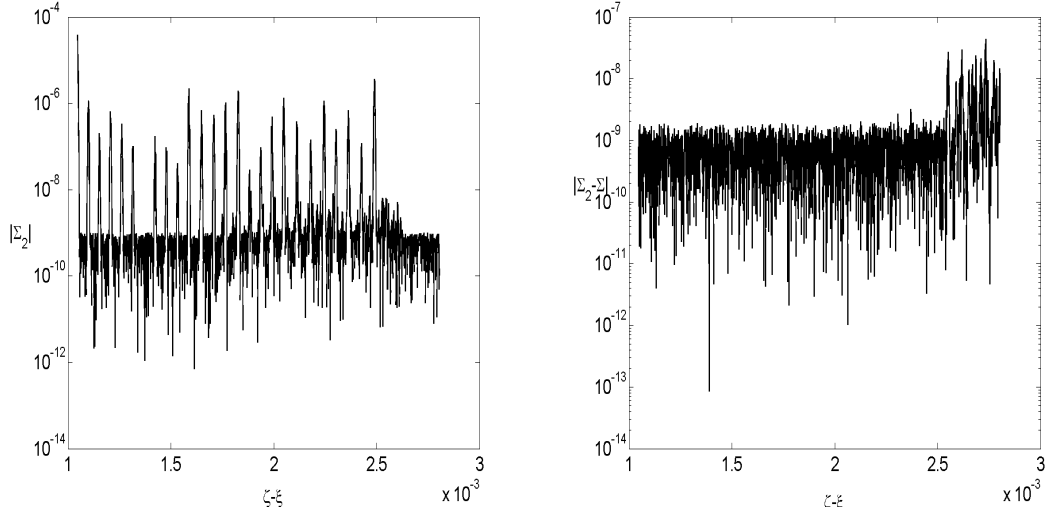


Figure 4.12: Left: Display of $|\Sigma_2(\xi)|$, as defined in equation (4.35), evaluated at 2200 sample positions ξ . Right: Difference between Σ (obtained by means of equation (4.16)) and Σ_2 (obtained by means of equation (4.35)) as a function of ξ .

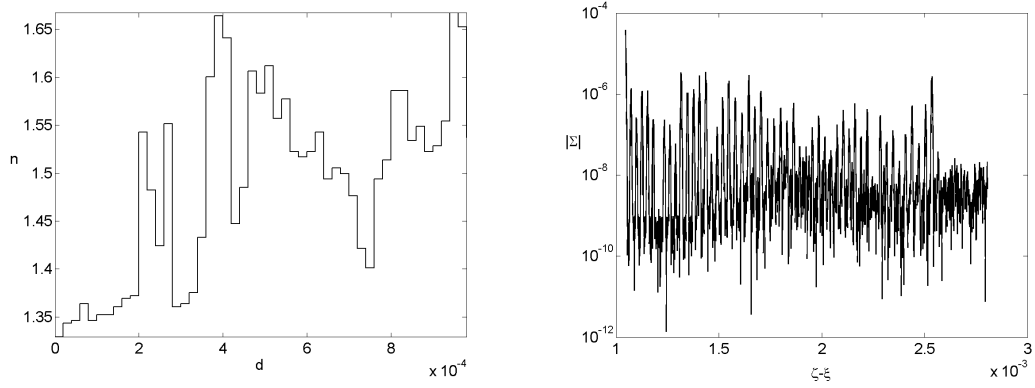


Figure 4.13: Left: Refractive index distribution along a multi-layer structure of thickness 1 mm. Right: Display of $\Sigma(\xi)$, defined by equation (4.16), evaluated at 2200 sample positions ξ .

calculate the partial correlation

$$\Sigma_1(\xi) = -\frac{\sqrt{2\pi}}{8} \int_{S_P} \text{Re} \left(\bar{R}_{j-1,j} \gamma \left(\tau - \sum_{s=1}^{j-1} t_s^{\text{delay}} \right) \right) dS_P, \quad (4.33)$$

where \bar{R} is given by

$$\bar{R}_{j-1,j} = R_{j-1,j} \prod_{q=1}^{i-1} T_{q-1,q} T_{q,q-1}, \quad (4.34)$$

which involves only interface transmissions, except for the direct reflection at the j th boundary; see Figure 4.7 which shows the ray giving rise to this single-reflection contribution to Σ in the case of a normally incident beam. The quantity Σ_1 is usually a poor approximation to Σ . To improve this approximation we define

$$\Sigma_2(\xi) = \Sigma_1(\xi) + \Sigma_c(\xi), \quad (4.35)$$

where Σ_c is a correction term including a finite number of multiple reflections, as discussed in what follows, which is needed to reduce the truncation error to a prescribed level—which, typically we take to equal the noise floor. In our work we consider a noise floor of the order of 10^{-4} relative to the intensity signal of the first reflection, which is itself proportional to $R_{0,1}$. We also note that, for the refractive indexes we consider most often in our numerical examples, all of the quantities $R_{j-1,j}$ are of the order of 10^{-1} for every $1 \leq j \leq N^{\text{layers}}$. It therefore follows that, for the values of the parameters we have chosen, $R_{j-1,j}^5 \approx O(\text{noise floor})$ and thus, to compute Σ_c to within an error of the order of the prescribed noise floor we need only take into account the reflections involving, at most, three reflections coefficients—thus, neglecting five reflections and higher. (Clearly the number of reflections is necessarily odd.) Of course, the number of reflections needed to achieve a desired error depends on the specific values of the parameters under consideration, and those given above are meant as an illustration only.

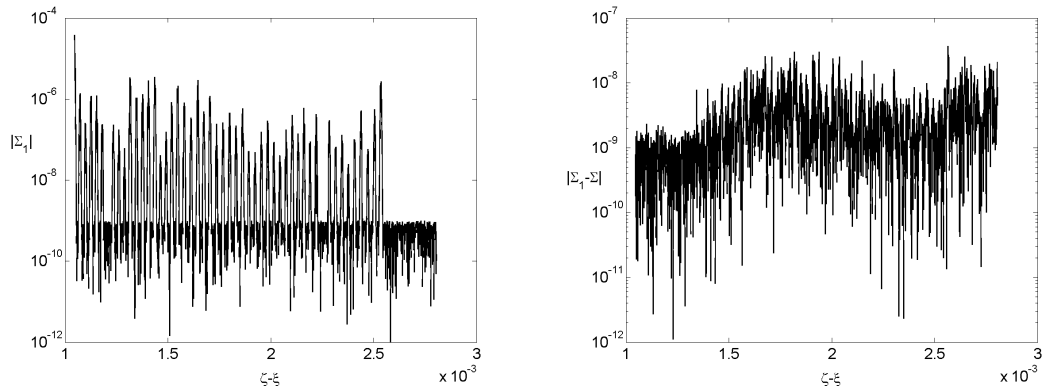


Figure 4.14: Left: Display of $|\Sigma_1(\xi)|$, as defined by equation (4.33), evaluated at 2200 different positions of the sample. Right: Difference between Σ (obtained by means of equation (4.16)) and Σ_1 as a function of ξ .

To compute Σ_c we thus add all the rays which are reflected at previous boundaries, up to

the j -th boundary, and whose total optical path is equal to the relevant single reflection path. Under the assumption discussed above that a maximum of three reflections is allowable, for example, and considering the rays that reach their maximum depth inside the sample at the i -th boundary, with $i < j$ and with $j - i = k$ interfaces before the j -th boundary, then we need to include all the possible paths that reflect at the i -th interface and travel twice through a group of exactly k subsequent layers, see Figure 4.8.

To provide a closed form expression for Σ_c under the hypothesis of a maximum of three reflections we define

$$\alpha_{k,p} = R_{p-1,p} R_{p+k-1,p+k} \prod_{l=p+1}^{p+k-1} T_{l-1,l} T_{l,l-1},$$

where $R_{j-1,j}$, $T_{q-1,q}$ are the Fresnel coefficient defined in (4.23) and (4.24), respectively. The quantity $\alpha_{k,p}$ is the coefficient accounting for the reflection at the interfaces p and $p+k$ and the transmissions through interfaces $p+1, \dots, p+k-1$. Note that generally there are two possible realizations involving the same set of reflection and transmission coefficients, an exception of this rule arises for $p+k = i$. The factor m_{p+k} , which is defined by $m_{k,p} = 1$ for $p+k = i$, and by $m_{k,p} = 2$ for $p+k \neq i$ accounts for such multiplicities in equation (4.36). (Figure 4.9 displays a second realization of $\alpha_{k,p}$, different from that of Figure 4.8.) Then denoting by

$$\hat{\alpha} = \frac{\sqrt{2\pi}}{8} Re \left(\sum_{i=j/2}^{j-1} \bar{R}_{i-1,i} \sum_{k=j-i}^{j-i+2} \sum_{p=1}^{i-k} m_{k,p} \alpha_{k,p} \gamma \left(\tau - \sum_{q=1}^{i-1} t_q^{delay} - \sum_{q=p}^{p+k-1} t_q^{delay} \right) \right), \quad (4.36)$$

the sum of all possible rays containing at most three reflections, $\Sigma_c(\xi)$ is given by

$$\Sigma_c(\xi) = \int_{S_P} \hat{\alpha} dS_P. \quad (4.37)$$

In order to illustrate numerically the character of equation (4.35) we present two numerical examples. We first consider a multi-layer structure with $N^{layers} = 25$ layers of thickness $d_q = 40 \mu\text{m}$ for $1 \leq q \leq N^{layers}$, see Figure (4.10) left. Figure (4.10) right displays $|\Sigma|$ as a function of ξ for the refractive index distribution shown in on Figure (4.10) left. Figures (4.11) and (4.12), in turn, display $|\Sigma_1|$ and $|\Sigma_2|$ as functions of ξ (see equations (4.33) and (4.35)), and the corresponding errors in these approximations to $|\Sigma|$. From

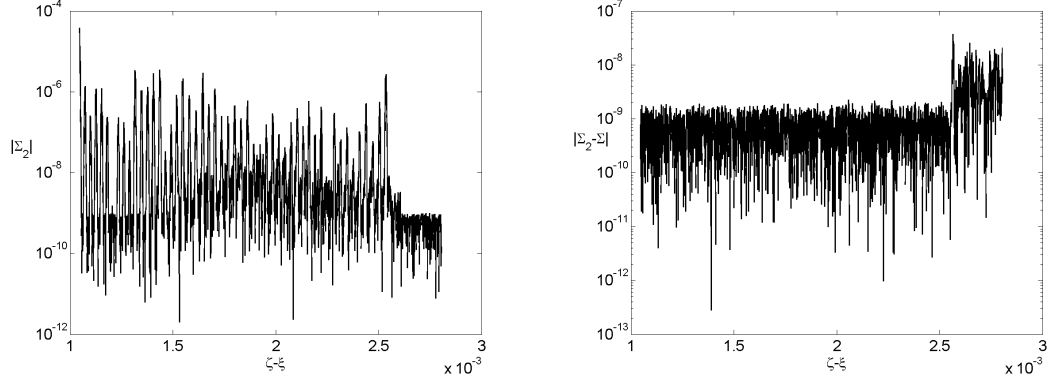


Figure 4.15: Left: Display of $|\Sigma_2(\xi)|$, as defined by equation (4.35), evaluated at 2200 sample positions ξ . Right: Difference between Σ (obtained by means of equation (4.16)) and Σ_2 as a function of ξ .

Figure (4.11) we see that inclusion of a single reflection does not suffice to obtain agreement of Σ and $|\Sigma_2|$ up to the noise floor. Figure (4.12), on the other hand, shows that by adding the correction term (4.37) an error below the noise floor results.

In the second example, we consider a multi-layer structure with $N^{layers} = 50$ layers of thickness $d_q = 20 \mu\text{m}$, see Figure (4.13) left. Figure (4.13) right displays $|\Sigma|$ as a function of ξ —for the refractive index distribution displayed in Figure (4.13) left. Figure (4.14) and Figure (4.15) display $|\Sigma_1|$ and $|\Sigma_2|$ obtained using equations (4.33) and (4.35), and the corresponding errors in these approximations to $|\Sigma|$. We see that the single reflection approximation Σ_1 in this case is less accurate than in the previous example. Again the correction term drastically improves the approximation, see Figure 4.15 right.

The benefits of this approach for fast evaluation of the correlation are significant: the direct evaluation of Σ at 2200 values of ξ requires 104 minutes on a 2.4GHz PC (for either $N^{layers} = 25$ or $N^{layers} = 50$), while the evaluation of the accurate approximation $|\Sigma_2|$ at the same number of points can be accomplished in 25 seconds for $N^{layers} = 25$ and 80 seconds for $N^{layers} = 50$, on the same computer.

Chapter 5

OCT Inverse Problem

5.1 Introduction

Our approach to the OCT imaging problem seeks to solve the inverse problem of obtaining distributions of refractive indexes from OCT fringe-patterns. As discussed in Section 3, the classical inverse problem for the Helmholtz equation is ill-posed and therefore extremely difficult to solve. Fortunately, the coherence properties of light, which certainly play a central role in direct OCT imaging strategies (such as those proposed in [38] and [68]), can also be exploited to solve efficiently the fringes-to-indexes inverse problem under consideration. We formulate the OCT inverse problem as follows: Assuming

$$\Sigma = B\tilde{u}^{scatt}(x, z, \omega) = \frac{1}{\sqrt{2\pi}} \int_{S_P} \int_{-\infty}^{\infty} S(\omega) \tilde{u}^{ref*}(P, \omega) \tilde{u}^{inc}(P, \omega) d\omega dS_P \quad (5.1)$$

is known for various sample positions ξ , see equation (4.7), determine the refractive index $n(z)$ within the sample.

5.2 Absorption

At this stage it is important to discuss the role of absorption—the imaginary part of the refractive index—in our problem. The absorption κ has a measurable effect in the backscattered field, and, as we will show, its consideration is necessary if accurate renderings are to be obtained through the solution of OCT inverse problems. In what follows we show, however, that a *precise* determination of the variations of κ within the sample is not necessary in many cases of practical interest—such as, for example, when the sample to be imaged does not contain large variations in the absorption coefficient. In such cases, in essence,

only the average value of κ plays a role in the solution of our inverse problem.

5.2.1 Difficulty in the Evaluation of Pointwise κ Values

We first consider an example showing that, quite generally, it is not easy to obtain the values of κ within the sample through solution of an inverse problem. The geometry of this example is quite simple: it consists of a planar interface between materials of refractive indexes $n+i\kappa$ on the right side and $n_1+i\kappa_1$ on the left side. Further, we assume a horizontal incident plane wave $e^{ik_z z}$. As before τ is given by equation (4.27). In this case the fringes at the detector are determined by

$$\Sigma(\xi) = \int_{S_P} \text{Re} \left(-\frac{\sqrt{2\pi}}{16} r \gamma(\tau) \right) dS_P,$$

where r is the Fresnel reflection coefficient

$$r = \frac{n_1 + i\kappa_1 - (n + i\kappa)}{n_1 + i\kappa_1 + (n + i\kappa)},$$

and $\gamma(\tau)$ is defined by equation (4.17). Assuming $n_1 = 1$ and $\kappa_1 = 0$ we have for the integrand

$$g(\xi) = \text{Re} \left(-\frac{\sqrt{2\pi}}{16} r \gamma(\tau) \right) = \frac{|\gamma(\tau)| \sqrt{\frac{\pi}{2}} \left((-1 + n^2 + \kappa^2) \cos(\omega\tau) + 2\kappa \sin(\omega\tau) \right)}{4\tau^2 (1 + 2n + n^2 + \kappa^2)}.$$

For this example a simplified version of our inverse problem can be stated as follows: given $g(\xi_1)$ and $g(\xi_2)$ determine n and κ . Here, we denote $\tau_1 = 2(\zeta - \xi_1)/c$ and $\tau_2 = 2(\zeta - \xi_2)/c$. To solve for n and κ we use Newton's method which leads us to deal with the Jacobian matrix J whose components are given by

$$\begin{aligned} J_{11} &= \frac{|\gamma(\tau_1)| \sqrt{\frac{\pi}{2}} \left((1 + 2n + n^2 - \kappa^2) \cos(\omega\tau_1) - 2(1+n)\kappa \sin(\omega\tau_1) \right)}{2(1 + 2n + n^2 + \kappa^2)^2} \\ J_{12} &= \frac{|\gamma(\tau_1)| \sqrt{\frac{\pi}{2}} \left(2(1+n)\kappa \cos(\omega\tau_1) + (1 + 2n + n^2 - \kappa^2) \sin(\omega\tau_1) \right)}{2(1 + 2n + n^2 + \kappa^2)^2} \\ J_{21} &= \frac{|\gamma(\tau_2)| \sqrt{\frac{\pi}{2}} \left((1 + 2n + n^2 - \kappa^2) \cos(\omega\tau_2) - 2(1+n)\kappa \sin(\omega\tau_2) \right)}{2(1 + 2n + n^2 + \kappa^2)^2} \\ J_{22} &= \frac{|\gamma(\tau_2)| \sqrt{\frac{\pi}{2}} \left(2(1+n)\kappa \cos(\omega\tau_2) + (1 + 2n + n^2 - \kappa^2) \sin(\omega\tau_2) \right)}{2(1 + 2n + n^2 + \kappa^2)^2}, \end{aligned}$$

$$\det(J) = \frac{-|\gamma(\tau_1)||\gamma(\tau_2)|\pi \sin(\omega(\tau_1 - \tau_2))}{8(1 + 2n + n^2 + \kappa^2)^2},$$

so that, at every Newton iteration the system

$$\begin{pmatrix} J_{11}^j & J_{12}^j \\ J_{21}^j & J_{22}^j \end{pmatrix} \begin{pmatrix} n^{j+1} - n^j \\ \kappa^{j+1} - \kappa^j \end{pmatrix} = \begin{pmatrix} \Sigma_1 - \Sigma^j(\xi_1) \\ \Sigma_2 - \Sigma^j(\xi_2) \end{pmatrix} \quad (5.2)$$

must be solved. Here Σ_1 and Σ_2 denote measured data, while the j super-indexes in J and Σ indicate that these functions are evaluated at n^j, κ^j .

One can check easily that the order of magnitude of the quantities in the system (5.2) are as follows:

$$\begin{pmatrix} O(1) & O(1) \\ O(1) & O(1) \end{pmatrix} \begin{pmatrix} O(1) \\ O(\kappa) \end{pmatrix} = \begin{pmatrix} O(1) \\ O(1) \end{pmatrix}$$

for definiteness we quote here the value $O(\kappa) \approx 10^{-4}$, which is commonly found in biological tissue. Thus, κ is given by a difference of the form

$$\kappa = O(1) - O(1).$$

Clearly, this operation leads to a significant loss of accuracy. Further, such accuracy losses are compounded in the evaluation of the absorption in the subsequent layers of a multi-layered sample, giving rise to incorrect rates of decay, and thus, to a rapid deterioration of the accuracy *in both the real and imaginary part of the refractive index*. Our numerical experiments fully support this analysis, showing that accurate determination of absorption values on a layered structure can only be accomplished for samples containing a small number of layers. Fortunately, we find that accurate determination of the absorption coefficient is not necessary and appropriate estimates of their averages suffice—as discussed in the following section.

5.2.2 Absorption Averaging

It is easy to see that, in many cases, only the average value of the absorption coefficient κ plays a significant role in the backscattered returns, and, thus, in the determination of *the real part* of the refractive index throughout the sample. To demonstrate this we consider

a layered structure containing a number Q layers of thicknesses d_q and refractive indexes $N_q = n_q + i\kappa_q$ ($q = 1, \dots, Q$). For notational simplicity we restrict our discussion to an incident ray of the form

$$E^{inc} = E_0 e^{ik_z z};$$

it should be clear that the conclusions of this analysis apply in the case of general incidence as well.

Due to the nature of our interferometric problem it is important to consider rays which travel a given real distance D within the sample. For any such ray we have $D = \sum_{q=1}^Q f_q d_q$ where f_q denotes the number of times the ray traveled through the q -th layer. The contribution of the ray to the scattered field, in turn, is given by

$$E^{refl} = R E_0 e^{-k_z \sum_{q=1}^Q \kappa_q f_q d_q} e^{ik_z z} e^{ik_z \sum_{q=1}^Q n_q f_q d_q}, \quad (5.3)$$

where the quantity R involves products of the coefficients $T_{q,q+1}$, $R_{q,q+1}$ of equations (4.23) and (4.24).

Equation (5.3) can be re-expressed as follows

$$\begin{aligned} E^{refl} &= R E_0 e^{-k_z D (\sum_{q=1}^Q \kappa_q f_q d_q) / D} e^{ik_z z} e^{ik_z \sum_{q=1}^Q n_q f_q d_q} \\ &= R E_0 e^{-k_z \bar{\kappa} D} e^{ik_z z} e^{ik_z \sum_{q=1}^Q n_q f_q d_q}, \end{aligned}$$

where $\bar{\kappa} = (\sum_{q=1}^Q \kappa_q f_q d_q) / D$ is the absorption average along the path visited by the ray. From equations (4.23) and (4.24), and since $O(\kappa_q)$ is small, we have

$$\begin{aligned} T_{q,q+1} &\approx \hat{T}_{q,q+1} = \frac{2n_q}{n_q + n_{q+1}} \\ R_{q,q+1} &\approx \hat{R}_{q,q+1} = \frac{n_q - n_{q+1}}{n_q + n_{q+1}}, \end{aligned}$$

so that $R \approx \tilde{R}$ where \tilde{R} is a coefficient involving products of $\tilde{T}_{q,q+1}$, $\tilde{R}_{q,q+1}$ and we therefore obtain our approximate expression for the reflected field

$$E_r \approx \tilde{R} E_0 e^{-k_z \bar{\kappa} D} e^{ik_z z} e^{ik_z \sum_{q=1}^Q n_q f_q d_q},$$

which depends on the absorption in terms of the average absorption only.

To demonstrate the accuracy of this approximation, we again use two-layer structures, with layers of thicknesses $d_1 = d_2 = 10 \mu\text{m}$, and we assume an incident beam of the form $u(x, z) = e^{ik_z z}$. We then compare the function g resulting in the case in which the refractive indexes of the respective layers are $N_1 = 1.4 + 10^{-4}i$ and $N_2 = 1.6 + 5 \cdot 10^{-4}i$, to that resulting from use of refractive indexes $N_3 = 1.4 + 3 \cdot 10^{-4}i$ and $N_4 = 1.6 + 3 \cdot 10^{-4}i$ —whose imaginary parts equal the average of the imaginary parts of N_1 and N_2 . The values of the function g and its truncation g^{trunc} are given in Table 5.1.

Again we have

$$\begin{aligned}\tilde{u}^{scatt}(P, \omega) &= -\frac{1}{4}\tilde{R}_{0,1}e^{ik(D+\eta+2\xi)} \\ \tilde{u}^{ref}(P, \omega) &= \frac{1}{4}e^{ik(D+\eta+2\xi)},\end{aligned}$$

where $\tilde{R}_{0,1}$ is given by equation (4.22). In this case equation (4.16) becomes

$$\Sigma(\xi) = -\frac{1}{16\sqrt{2\pi}} \int_{S_P} \int_{-\infty}^{\infty} S(\omega) \tilde{R}_{0,1} e^{-i\omega\tau} d\omega dS_P. \quad (5.4)$$

where τ is given by equation (4.27).

Table 5.1: Comparison of correlation values in two different bi-layer structures: 1) Layers contain materials of refractive indexes $N_1 = 1.4 + 10^{-4}i$ and $N_2 = 1.6 + 5 \cdot 10^{-4}i$; and 2) Layers containing materials of refractive indexes $N_3 = 1.4 + 3 \cdot 10^{-4}i$, $N_4 = 1.6 + 3 \cdot 10^{-4}i$, with absorptions equal to the average of the absorptions in N_1 and N_2 .

ξ	$g(\xi) (N_1, N_2)$	$g(\xi) (N_3, N_4)$
$\xi = 0$	0.0522214	0.0522214
$\xi = d_1^{opt}$	0.0203083	0.0194274
$\xi = (d_1^{opt} + d_2^{opt})$	-0.064040	-0.064040

From Table 5.1 we see that use of an average value of the absorption does indeed lead to good approximations of g . (As shown in Section 6, however, total neglect of the absorption may leads to significant distortions in the images produced.) We also note that a somewhat lesser degree of agreement occurs for the values of g at $\xi = d_1^{opt}/c = n_1 d_1/c$. In principle this might be considered as a failure of our theory—but in fact it is not. Indeed, for this value of ξ the only ray that produces a significant contribution to g is that which has only traveled through the first layer, and thus, has not been able to sample the various absorptions

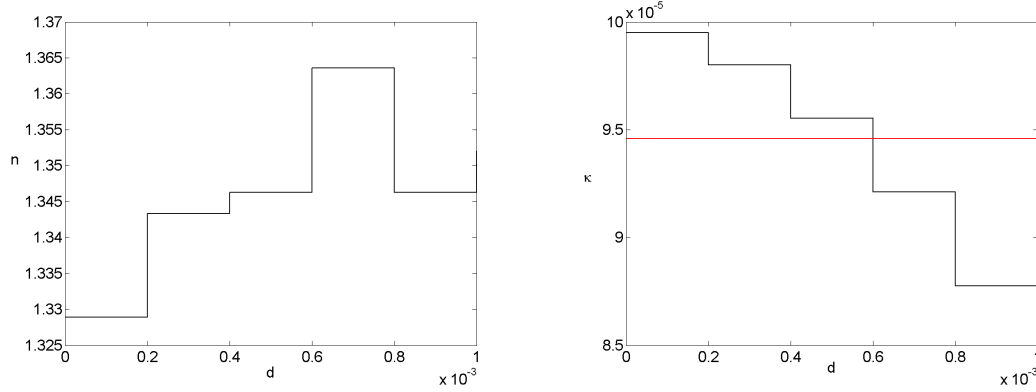


Figure 5.1: Left: Refractive index distribution. Right: Absorption distribution in blue. Absorption average in red, $\kappa = 0.9458e - 4$.

present in the specimen. Better agreement occurs for $\xi = 0$ because the absorption only plays a role in the reflection coefficient and does not lead to true absorption of energy in this case. For $\xi = \text{Re}(d_1^{\text{opt}} + d_2^{\text{opt}})$ we again see excellent agreement, as the absorption of both layers has been sampled. Generally then, we may expect good approximations from the averaging procedure except for particular situations in which the local averages of the absorption within the sample differs significantly from its overall absorption. The experiments presented in Section 6 give a clear sense of the (small amount of) tuning of the average absorption parameter which is needed to produce good reconstructions.

5.3 “Coherent” Nonlinear Equations

To describe the advantages provided by the OCT setup for the solution of the fringes-to-indexes inverse problem we point out that, as noted earlier, the field u^{scatt} equals the sum of a series of multiple reflections at the various layer interfaces. Every one of these reflections interferes with the reference beam to a larger or lesser extent, depending on the difference between the total optical path of a given reflection and the total optical path of the reference beam—so that, for a given reference path-length, fringes arise, mainly, from small regions within the sample. The procedure we use to solve the OCT inverse problem, which is detailed in what follows, depends on this observation for both, computational efficiency and accuracy.

Consider a multi-layer structure with a number Q of layers with refractive indexes N_q

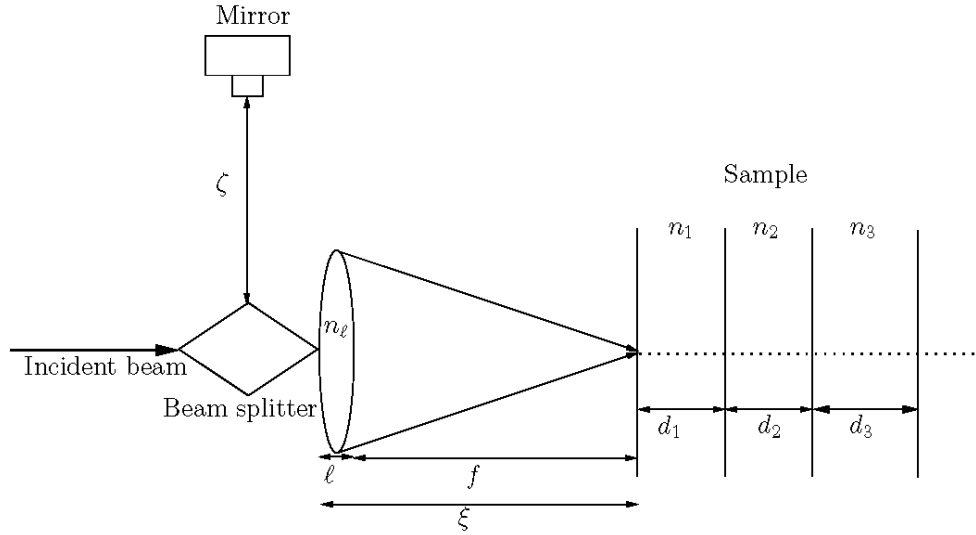


Figure 5.2: Starting point for the scanning process.

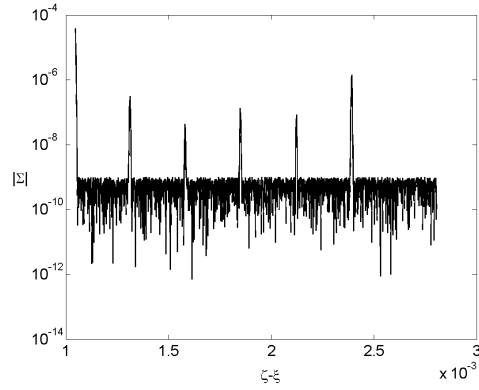


Figure 5.3: Absolute value of the correlation function Σ as a function of ξ arising from the refractive index distribution displayed in Figure 5.1.

and thicknesses d_q with $1 \leq q \leq Q$, such as the one shown in Figure 5.1. Assume the reference mirror and the sample are located at distances ζ and ξ from the beam splitter, respectively, and that a lens with axial thickness ℓ and refractive index n_ℓ is placed in the sample arm, see Figure 5.2. The optical path-length traveled by a ray of light in the reference arm equals 2ζ , while the optical path-length in the sample arm traveled by a ray of light which is reflected only once, and for which the reflection takes place at the i -th interface equals $2(\xi - \ell)/\cos(\theta') + L + \sum_{q=1}^i 2N_q d_q \cos(\theta_{q^{trans}})$, where L is the optical path-length traveled by the light through the lens (equation (A.3)), θ' is the angle of the

incident ray defined in equation (A.1) and θ_q^{trans} is the transmission angle through the q -th interface. Note that θ' is a function of h ; see Figure A.1.

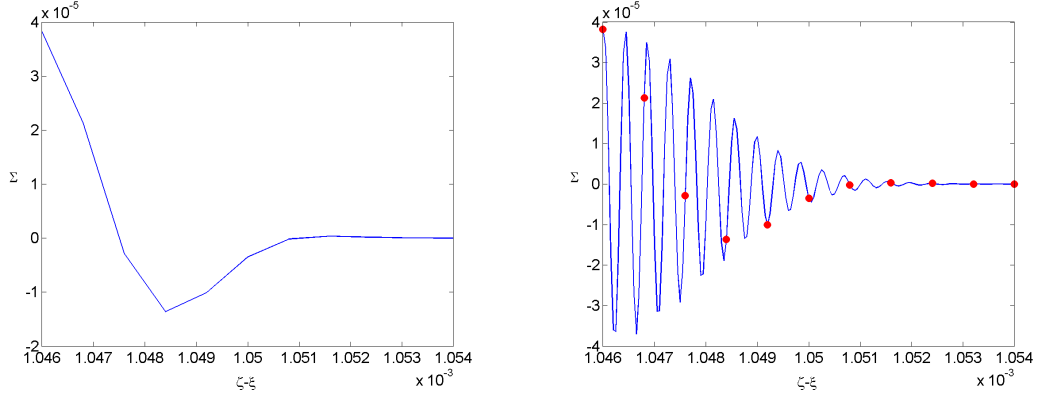


Figure 5.4: Left: Coarse sampled first spike in Figure 5.3. Right: Finely sampled first spike, with circles showing the coarse samples displayed on the left.

In order to solve the fringes-to-indexes inverse problem we need to obtain the thicknesses d_q as well as the real part n_q of the refractive indexes $N_q = n_q + i\kappa_q$ from the values of Σ in equation (5.4) for various values of ξ . To do this, we consider measurements of Σ for different positions of the sample as detailed in what follows: We first place the sample at an initial position $\xi = \xi_0$ for which the paraxial focus (see Appendix A) coincides with the first interface, and we place the mirror so that the optical path-length ζ traveled by the light from the lens to the mirror matches the optical path-length $n_\ell \ell + f$ traveled by a horizontal ray of light from the lens to the first interface; see Figure 5.2. We then take successive measurements locating the sample at positions

$$\xi_i = \xi_0 - i\epsilon, \quad (5.5)$$

where ϵ is a suitable parameter—which, for our numerical examples, was taken to equal $\epsilon = 800$ nm: close to but different from the 850 nm center wavelength of the source; see Section 5.5.1 for a discussion on useful choices of the parameter ϵ .

Figure 5.3 shows the total fringe intensity as a function of ξ . The marked spikes in this figure correspond to light scattered by the interfaces: from left to right the first spike correspond to the interfaces between air and the first layer, the second one corresponds to the interface between the first two layers in the sample, and so on, and the last spike

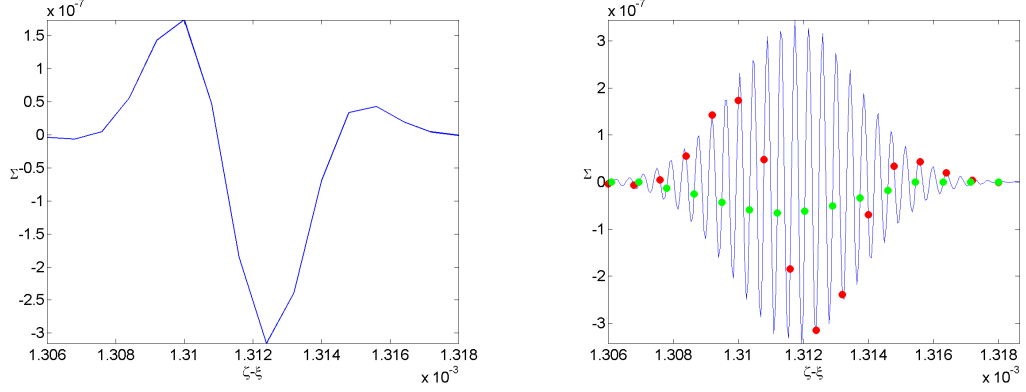


Figure 5.5: Left: Coarse sampled second spike in Figure 5.3. Right: Finely sampled second spike, with red circles showing the coarse samples displayed on the left, and with green circles showing coarse “aliased” samples providing data of very small numerical value, which is prone to be degraded by noise.

correspond to reflection between the last interface and air.

In Figures 5.4 and Figure 5.5 we show blow-ups of the two first spikes in Figure 5.3 right, respectively; we see that these spikes have a definite structure. Our methods utilize the details of such spike structures to determine the refractive index distributions within the sample.

To do this we denote by Υ_q the number of “relevant” (non-negligible) measurements associated with the q -th spike. Further, we denote by ξ_i^q ($1 \leq i \leq \Upsilon_q$) the sample positions associated with such relevant measurements for the q -th spike, so that $\Sigma(\xi_i^q)$ is the i -th measurement associated with the q -th interface, $1 \leq i \leq \Upsilon_q$.

The first spike, detailed in Figure 5.4, can be used to determine the refractive index of the first layer, since the coherent backscattering from the subsequent layers is exponentially small. That is to say, this index of refraction can be obtained as the solution of a certain nonlinear vector equation, $F^1(X^1) = 0 \in \mathbb{R}^{\Upsilon_1}$ where the vector function F^1 has components $F_i^1(X^1) = \Sigma^{meas}(\xi_i^1) - \Sigma_2(\xi_i^1, X^1)$, where X^1 denotes the refractive index n_1 to be calculated. More generally, once the first $q - 1$ refractive indexes and the first $q - 2$ widths have been found, the q -th spike can be used to determine the refractive index of the q -th layer and the thickness of the $(q - 1)$ -th layer. In each case, we must determine the values of a refractive index and a thickness as the solution to a certain nonlinear equation $F^q(X^q) = 0 \in \mathbb{R}^{\Upsilon_q}$

where X^q is the two-dimensional vector

$$X^q = (n_q, d_{q-1}).$$

Here as above

$$F_i^q(X^q) = \Sigma^{meas}(\xi_i^q) - \Sigma(\xi_i^q, X^q).$$

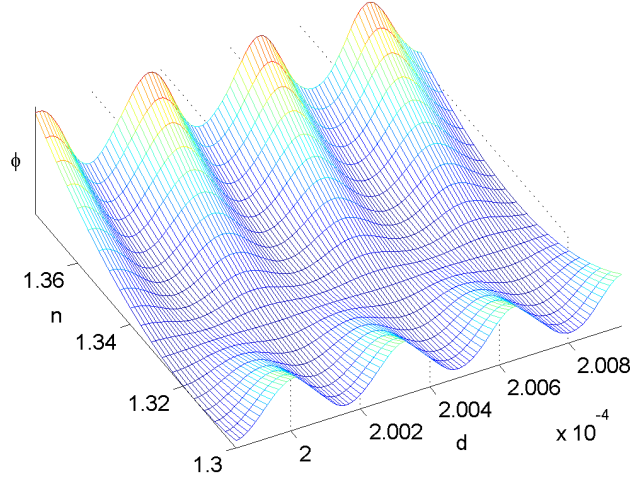


Figure 5.6: Mean-square function $\phi^q = \phi^q(n, d)$.

While in principle it would suffice to use two equations to determine n_q and d_{q-1} , we have found that, as is common in the solution of inverse problems, use of an overdetermined system of Υ_q equations and two unknowns is highly advantageous in this case. Denoting by X_0^q the solution of the overdetermined system of nonlinear equations $F(X^q) = 0$ or, equivalently, the minimizer of the functional $\phi^q(X^q) = \frac{1}{2}F^q(X^q)^T F^q(X^q)$, we obtain X_0^q by means of the Gauss-Newton method: Defining by Y_n^q is the solution of the linear system

$$A_n^q Y_n^q = -\nabla \phi^q(X_n^q),$$

(where $\nabla \phi^q(X_n^q) = J_{F^q}^T(X_n^q) F^q(X_n^q)$, $A_n^q = J_{F^q}^T(X_n^q) J_{F^q}(X_n^q)$, J the Jacobian of F^q), we produce the $(n + 1)$ -th Gauss-Newton iterate by means of the expression

$$X_{n+1}^q = X_n^q + Y_n^q.$$

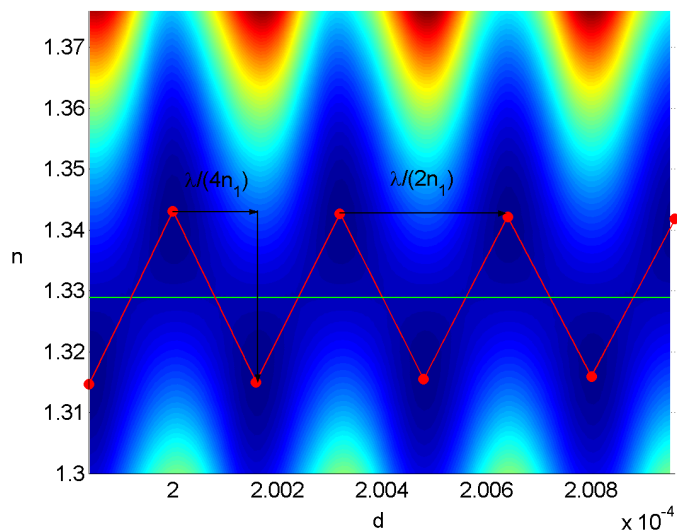


Figure 5.7: Mean-square function $\phi^q = \phi^q(n, d)$: dark reds and dark blues indicate large and small function values, respectively.

As it happens, the derivatives necessary to evaluate the gradient and the jacobian of the function ϕ^q for a given layer can be computed analytically from the expression (4.35) for the approximation Σ_2 of the correlation Σ . Indeed, note that, when working on the q -th interface, the only term in equation (4.35) that depends on the differentiation variables n_q and d_{q-1} is Σ_1 , as given in equation (4.33). The term Σ_c only involves reflections arising from the previous layers and therefore, it does not depend on either n_q or d_{q-1} .

A difficulty arises in our minimization problem since the Gauss-Newton method generally converges to a local minimum only, and local minima are ubiquitous in our problem. An important task is, then, to find appropriate starting points which guarantee that a Newton-based method yields the global minimum. Our construction of an appropriate class of starting points, which is presented in the following section, is, indeed, what renders our approach feasible.

5.4 Structure of the Minimization Problem and Choice of Starting Points

Our algorithm for determination of global minima is based on some important general properties of the functions $\phi(X^q)$. Figures 5.6 to 5.9 illustrate these characteristics:

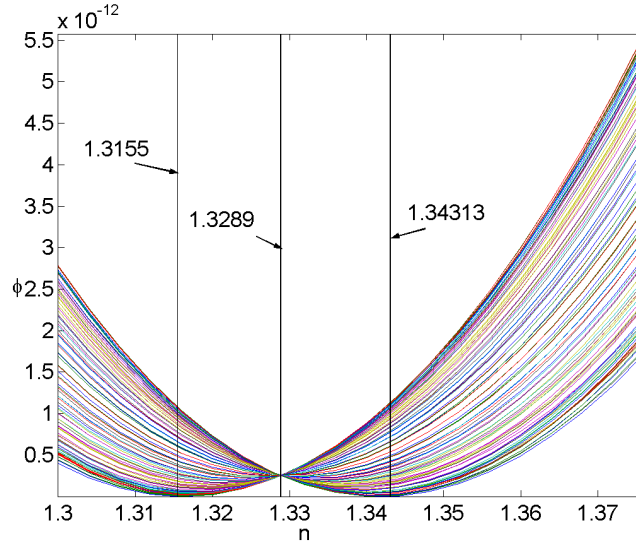


Figure 5.8: Mean-square function ϕ^q for several values of the refractive index n .

1. The function $\phi^q(X)$ has several local minima within the minimization domain—see Figure 5.6 and the top view Figure 5.7, in which darker shades of blue identify smaller values of the function ϕ .
2. For fixed values of d the function ϕ^q exhibits a parabolic behavior with respect to refractive index variations, (see Figure 5.8), and, for fixed values of n , it exhibits oscillatory behavior with respect to variations of the thickness parameter d , (see Figure 5.9).
3. The local minima (resp. local maxima) of ϕ^q as a function of d for fixed $n > n_{q-1}$ are located at positions that vary only slightly with n , and the distance between two consecutive local minima (resp. local maxima) is $\approx \tilde{\lambda}/2$ —where $\tilde{\lambda} = \lambda/n_{q-1}$ is the center wavelength in the $(q-1)$ -th layer ($\tilde{\omega} = 2\pi c/\lambda$ is the center frequency of the laser). Analogously, for all fixed $n < n_{q-1}$ the distance between two consecutive local minima or maxima is, again, $\approx \tilde{\lambda}/2$. The fact that the distance between local maxima/minima is approximately half a wavelength can be understood easily by considering that, as the position of the interface under consideration is perturbed by an amount $\pm e$, the phase of the returning reflection beam undergoes a perturbation of $\pm 2e$, i.e., a ray traveling through the sample and returning from the interface needs to travel an additional $\pm 2e$ to arrive at the detector.

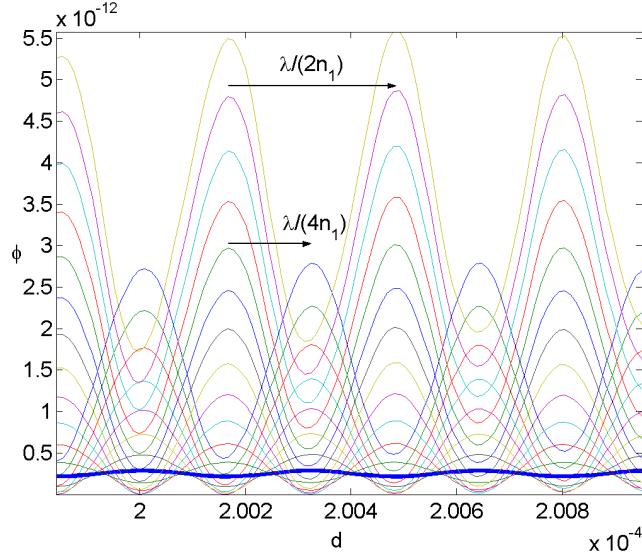


Figure 5.9: Mean-square function $\phi^q(n, d)$ as a function of d for several values of n .

4. The symmetries observed in Figure 5.7 can be understood by considering a two-layer problem, with refractive indexes n_1 and n_2 on the left and right of the interface, respectively, and illuminated by a normally incident ray; see Figure 5.10. The field reflected at the interface between the two layers is determined by the reflection coefficient $r = (n_1 - n_2)/(n_1 + n_2)$, and thus, for a fixed value of n_1 and setting $n_2 = n_1 + e$, to first order in e the field reflected by the interface is an odd function of e ,

$$\frac{-e}{2n_1 - e} = \frac{-e}{2n_1} (1 + e/2n_1 + \dots) \approx \frac{-e}{2n_1}.$$

On the other hand, an increase of d in the amount $\Delta d = \frac{\lambda}{4n_1}$ leads to an increase in the phase of the corresponding portion of field backscattered from the sample by π —that is, it leads to a change in sign in the field itself. It follows that, to first order in e , the quantity $\phi^q = \phi^q(n, d)$ as a function of d will be invariant under the substitutions

$$e = n - n_1, \quad n_1 - e \rightarrow n, \quad d + \frac{\lambda}{4n_1} \rightarrow d,$$

which explains the symmetries in Figure 5.7 around the line $n = n_1$.

5. In view of points 2. to 4. above we see that the line $n = n_{q-1}$ separates two sequences of local minima, and these two sequences contain all of the local minima relevant to

the determination of the thickness d_{q-1} and the refractive index n_q associated with the interference peak under consideration.

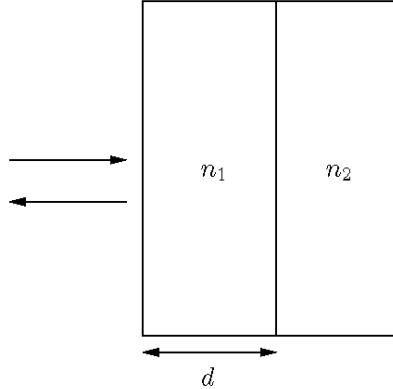


Figure 5.10: Two-layer structure with refractive indexes n_1 and n_2 and thickness d .

In light of these properties we design our minimization algorithm as follows: To determine the thickness and refractive index associated with a given fringe-intensity peak, we begin our optimization by setting the thickness parameter d to equal the thickness associated with the largest measured intensity in that peak. Next, we perform a minimization along the refractive index direction, thus obtaining a first high-quality initial guess p_0 for the minimization problem. Then, using the initial guess p_0 we proceed with Gauss-Newton iterations to convergence, to obtain a first local minimum, which we denote by p_1 . Once p_1 is obtained, we can produce very good new initial guesses in each one of the basins of attraction, see Figures 5.6, 5.7, and 5.9, in view of properties 4 and 5 above, by simply using the symmetry with respect to $n = n_1$ and the fact that the n -axis distances between minima are known with relatively small uncertainties. The Newton iterations starting from each one of these initial guesses converge rapidly to local minima p_1, p_2, \dots, p_m . The global minimization problem is then solved by selecting the p_i with a minimum ϕ value .

5.5 Model Example

In this section we present a numerical example demonstrating all of the details involved in the solution of an OCT inverse problem. To do this we consider a sample with a small number of layers: the five-layer structure depicted in Figure 5.1; see Table 5.2 for the precise

Table 5.2: Five-layer structure.

Layer	Refractive Index (n, κ)	Thickness d
1	(1.3289, $9.95e - 5$)	$2.0e - 4$
2	(1.3433, $9.80e - 5$)	$2.0e - 4$
3	(1.3462, $9.55e - 5$)	$2.0e - 4$
4	(1.3635, $9.21e - 5$)	$2.0e - 4$
5	(1.3462, $8.77e - 5$)	$2.0e - 4$

parameter values defining this sample structure (all of which are fairly common values for biological applications). Solutions of inverse problems involving much larger number of layers are given in Section 6. In the rest of this thesis we assume the focusing lens has the following characteristics: refractive index $n_\ell = 1.523$, thickness $\ell = 2mm$ and $r_1 = 10mm$, see Figure A.1 in Appendix A for details. In all cases we assume only a portion of the beam leaving the lens is used, leading to an effective numerical aperture of $NA = 0.054$; the corresponding paraxial focal point is located at $z = f$, where f is given by equation (A.4). The center wavelength and bandwidth of the laser were taken to be $\lambda = 850$ nm and $\Delta\lambda = 70$ nm, respectively. In our examples an error was added to synthetic “experimental data” so as to simulate the experimental noise floor; the added error was taken to be random and to the order of 10^{-4} times the largest interference intensity Σ arising in the computation.

5.5.1 Measurement Procedure

To obtain the measured data we begin by placing the sample so that its leftmost boundary lies at the point $z = \xi_0 = f + \ell$, see Figure 5.2, which coincides with the paraxial focal point. We then place the mirror at a distance $\zeta = f + \ell n_\ell$, see Figure 5.2. Next, we obtain the sequence of intensity-fringe values Σ that occur as the sample is relocated at the sequence of positions $\xi = \xi_0 - i \cdot \epsilon$ —where ϵ is an appropriately chosen step-size, and where i ranges from 1 to a number N^{meas} of measurements for which the scanning process cover the whole sample. We note that, for $i = 0$, the paraxial optical path length in the sample and reference arms are identical. It is important to select of the parameter ϵ appropriately: we recommend to choose ϵ close to but slightly different from the laser center wavelength; in our examples we used $\epsilon = 800$ nm for the laser wavelength $\lambda = 850$ nm. Adequate choices of ϵ lead to good fringe-sampling. Using $\epsilon = 850$ nm, for example, would lead to highly aliased

measurements such as those shown in green circles in Figure 5.5. Clearly, the green-circle data-points contain information of very poor quality, since they lie close to the noise floor and, thus, are significantly polluted by it. Solving the inverse problem with such polluted data is difficult, and may even lead to incorrect solutions.

5.5.2 Solution of the Nonlinear Equations

The first step in our nonlinear solve is to identify the measurement peaks which indicate the presence of interface layers. To do this we search for the measured values of $|\Sigma|$ above a certain threshold T^{thresh} ; in most of our examples we have used the threshold value $T^{thresh} = 10^{-8}$ —above the noise floor, which was assumed to equal 10^{-9} relative to the unit incident field. In the process of identifying measurement peaks two different problems may occur: 1) Isolated values greater than 10^{-8} may arise as result of multi-layers reflections. Those measurements would be interpreted as arising from a non-existing layer; this problem is tackled by noting that a peak must consist of a minimum number of measurements above the threshold; a lesser number of such measurements is therefore not taken to identify an interface. 2) Members of a peak may occasionally have a value of less than 10^{-8} and thus they would split the peak into two, which would then be taken to identify two different interfaces. This problem is tackled by noting that, if, indeed, two interfaces are to be identified, there should be a minimum number of consecutive low measurement values between them.

Table 5.3: Local minima obtained from the minimization process detailed in the text, and displayed by red circles in Figure 5.7.

Layer	Refractive Index n	Thickness d	ϕ	<i>Distance</i>
1	1.31468	$1.99841e - 4$	$1.37206e - 15$	$1.6e - 7$
2	1.34313	$2.0003e - 4$	$4.31751e - 18$	$1.59e - 7$
3	1.31501	$2.0016e - 4$	$1.41788e - 15$	$1.6e - 7$
4	1.34268	$2.0032e - 4$	$5.18346e - 15$	$1.6e - 7$
5	1.3155	$2.0048e - 4$	$1.07638e - 14$	$1.61e - 7$
6	1.34219	$2.00641e - 4$	$1.78218e - 14$	$1.6e - 7$
7	1.31594	$2.00801e - 4$	$2.60107e - 14$	$1.6e - 7$
8	1.34179	$2.00961e - 4$	$3.53315e - 14$	—

Determination of the first layer. Note that the first group of data measurements, displayed in Figure 5.4 left, is only determined by the refractive index of the first layer. Indeed, the second interface does not contribute significantly to the first fringe pattern: the rays reflected by it travel a significantly longer optical path than the rays reflected by the mirror. Therefore, the function $\phi^1(n_1)$ to be minimized depends only, (up to errors that are exponentially small on the width of the subsequent layer), on the refractive index n_1 . Following the notation of Section 5.3, in this case we obtain $\Upsilon_1 = 9$, $\xi_i^0 = f + \ell - i \cdot \epsilon$ ($0 \leq i \leq 9$), $X^1 = n_1$ and $F^1(n_1) \in \mathbb{R}^9$ with components $F_i^1(n_1) = \Sigma^{meas}(\xi_i^1) - \Sigma_2(\xi_i^1, n_1)$ —where the “measurements” $\Sigma^{meas}(\xi_i^1)$ for $0 \leq i \leq 9$ are displayed in Figure 5.4 left in red circles. The function $\phi^1(n_1)$ to be minimized is given by $\phi^1(n_1) = \frac{1}{2}|F^1(n_1)|^2$. In this case the minimization process proceeds as follows: Taking the initial guess $n_1^0 = 1$ we obtain the successive iterations

$$n_1^j = n_1^{j-1} + \frac{\phi'(n_1^{j-1})}{|J_F(n_1^{j-1})|^2},$$

where $J_F(n_1^{j-1})$ denotes the Jacobian whose components are $\partial F_i^1(n_1^{j-1})/\partial n_1$ with $0 \leq i \leq 9$. We stop the iteration process when $\left| \frac{\phi'(n_1^{j-1})}{|J_F(n_1^{j-1})|^2} \right| < 10^{-4}$. The result of the iteration process can be seen in the first row of Table 5.4; compare the “true” values displayed in Table 5.2.

Determination of the subsequent layers. To determine the thickness of the first layer and the refractive index of the second layer we utilize the second peak (depicted in Figure 5.5 left) which arises from reflections on the second interface. Note that the reflection from the third interface does not contribute, up to exponentially small errors, to the fringe pattern under consideration. Here we obtained $\Upsilon_2 = 9$. Solving the index-thickness inverse problem, as discussed in the previous chapter, requires determination of the values of a refractive index and a thickness as the solution of a certain nonlinear equation $F^{q=2}(X^{q=2}) = 0 \in \mathbb{R}^9$ where $X^{q=2}$ is the two-dimensional vector $X^{q=2} = (n_2, d_1)$.

$$F_i^{q=2}(X^2) = \Sigma^{meas}(\xi_i^2) - \Sigma(\xi_i^2, X^{q=2}).$$

with $0 \leq i \leq 9$. We will thus seek X_0^2 as the limit of the convergent sequence X_n^2 produced by Newton’s method for the functional $\phi^{q=2}(X^{q=2}) = \frac{1}{2}F^{q=2}(X^{q=2})^T F^{q=2}(X^{q=2})$ (Figure 5.6),

that is, we define

$$X_{n+1}^{q=2} = X_n^{q=2} + Y_n^{q=2},$$

where $Y_n^{q=2}$ is the solution of the linear system

$$A_n^{q=2} Y_n^{q=2} = -\nabla \phi^{q=2}(X^{q=2}),$$

where $\nabla \phi^{q=2}(X^{q=2}) = J_{F^{q=2}}^T(X^{q=2}) F^{q=2}(X^{q=2})$, $A_n^{q=2} = J_{F^{q=2}}^T(X_n^{q=2}) J_{F^{q=2}}(X_n^{q=2})$, J the Jacobian of $F^{q=2}$.

Table 5.4: Solution of the inverse problem with $\kappa = 0.9458e - 4$.

Layer	Refractive Index n	Thickness d
1	1.3288	$2.000006578e - 4$
2	1.3431	$2.000333861e - 4$
3	1.3459	$2.000400647e - 4$
4	1.3628	$2.001059278e - 4$
5	1.3459	$2.000428811e - 4$

As mentioned in Section 5.4, the function ϕ^q to be minimized has several local minima. In what follows, we show every detail of our global minimization method as it was described in Section 5.3. We first select an initial guess (n_2^0, d_1^0) , as given by the value $\xi_i^{q=2} = \xi_i^{2:max}$ that maximizes $|\Sigma^{meas}(\xi_i^2)|$ and we compute $d_1^0 = (\zeta - \xi_i^{2:max} \ell + n_\ell \ell) / n_1$. Note that d_1^0 is the actual distance a *normally* incident ray would travel inside the sample to reach the focus, assuming the focus and the second interface coincide for the sample position $\xi_i^{2:max}$. In general, for the q -th layer we use the initial guess $d_{q-1}^0 = (\zeta - \xi_i^{q:max} - \ell + n_\ell \ell) / n_{q-1} - \sum_{j=1}^{q-2} n_j d_j$. As a guess n_2^0 for the refractive index of the second layer, in turn, we take the value of the refractive index of the previous layer, $n_2^0 = n_1$. Once we have our initial guess, we perform a one-dimensional Newton minimization process in the variable n_2 (keeping d_1^0 fixed). In this way, we obtain a local minimum of $\phi^{q=2}$ for $d = d_1^0$ which will be our initial guess to perform a two-dimensional minimization process, leading to a first local minimum of $\phi^{q=2}$. Now, using the symmetry properties of the function ϕ^q described in Section 5.4, new starting points for the Newton methods are obtained, and all local minimum can be found. Comparison of the function values of all local minima, finally, yields the desired

global minimum.

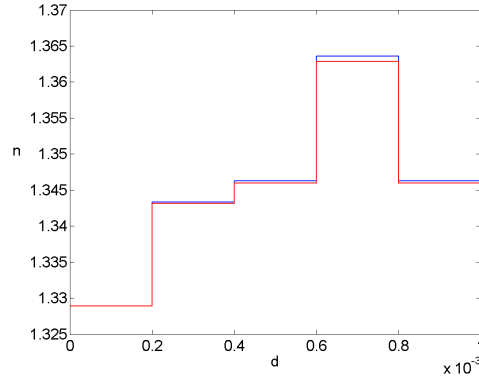


Figure 5.11: Blue curve: Given refractive index distribution. Red: solution obtained by means of the minimization procedure detailed in this section.

Table 5.3 shows the local minima of $\phi^{q=2}$, which are displayed as red circles in Figure 5.7. The sixth column shows the distance between two consecutive local minima. We see that, in accordance with our theory, this distance is in fact $\approx \lambda/(4n_1) = 1.5991e - 7$, where $n_1 = 1.3289$. Figure 5.8, in turn, displays $\phi^{q=2}$ as a function of n for several values of d ; we see that all local minima are concentrated around two values of n , again, in agreement with our theoretical results.

A similar algorithm is utilized to determine the thicknesses and refractive indexes of the subsequent layers. The solution obtained by this process is displayed in Figure 5.11 and the values obtained are shown in Table 5.4. The solution of the present inverse problem depicted in Figure 5.11 was obtained in 2 second run in a 2.4GHz Pentium IV PC.

Chapter 6

Numerical Results

In this chapter we demonstrate the performance of our algorithms through a variety of numerical examples. In all cases an error was added to synthetic “experimental data” so as to simulate the experimental noise floor; the added noise floor was taken to be random and to the order of 10^{-9} , relative to a unit incident field (10^{-4} relative to the largest interference intensity), see Figure 5.3. This noise level is much larger than the various noise bars reported in the literature [28, 39, 64, 67, 68].

6.1 Absorption Effects

To appreciate the effect of the approximations introduced in Section 5.2, we present solutions of an inverse problem containing a wide range of absorption variations—with an average absorption value equal to $0.6 \cdot 10^{-4}$. We generally may not assume this average value is known, and thus reconstructions should proceed through appropriate tuning of this parameter, see Figure 6.1.

This figure presents a prescribed refractive index map together with an image reconstructed under various assumptions for the average absorption parameter. We see that, as anticipated, values of this parameter close to the actual average absorption value result in excellent reconstructions, and that, even reconstructions based on values of this parameter far from the actual average absorption value produce informative images—albeit somewhat distorted.

In our second set of numerical examples we present inversion results corresponding to the 25-layer structure shown in Figure 6.2 top left, under assumption of three different (random) arrays of absorption coefficients, shown in Figure 6.2 top right, bottom left and

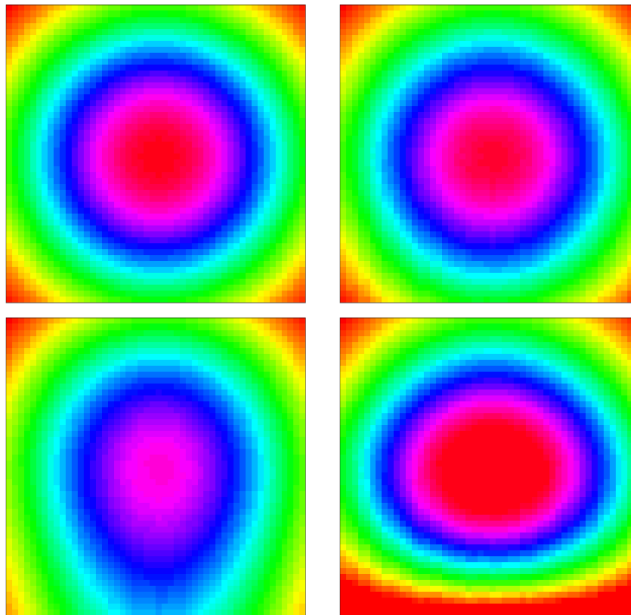


Figure 6.1: Effect of absorption averaging. Upper left: Prescribed refractive index map. Upper right, lower left and lower right: reconstructions using values $\kappa = 0.6 \cdot 10^{-4}$, $\kappa = 0$ and $\kappa = 1.2 \cdot 10^{-4}$ for the average absorption parameter, respectively.

bottom right. In all three cases the absorption coefficients κ range between 10^{-5} and 10^{-4} . The three corresponding reconstructions, obtained under assumption of a constant absorption equal to the average absorption in the true samples (which equals $0.6 \cdot 10^{-4}$) are shown in Figure 6.3 in red, magenta and green, respectively. Each one of these curves was obtained in an approximately 4 minute run on a 2.4GHz Pentium IV processor. Table 6.1 shows the maximum relative error for n and d in the solution. The agreement is excellent: the maximum error in the solution, which occurs for the magenta curve, does not exceed 2% in either the width or the refractive index.

Table 6.1: Errors in n and d reconstruction.

Color	Max Error in n	Max Error in d
Red	0.82%	0.76%
Green	0.48%	0.45%
Magenta	2%	1.7%

Our third set is similar to the previous one: it presents inversion results corresponding to the 50-layer structure shown in Figure 6.4 top left, under assumption of three different (random) arrays of absorption coefficients, shown in Figure 6.4 top right, bottom left and

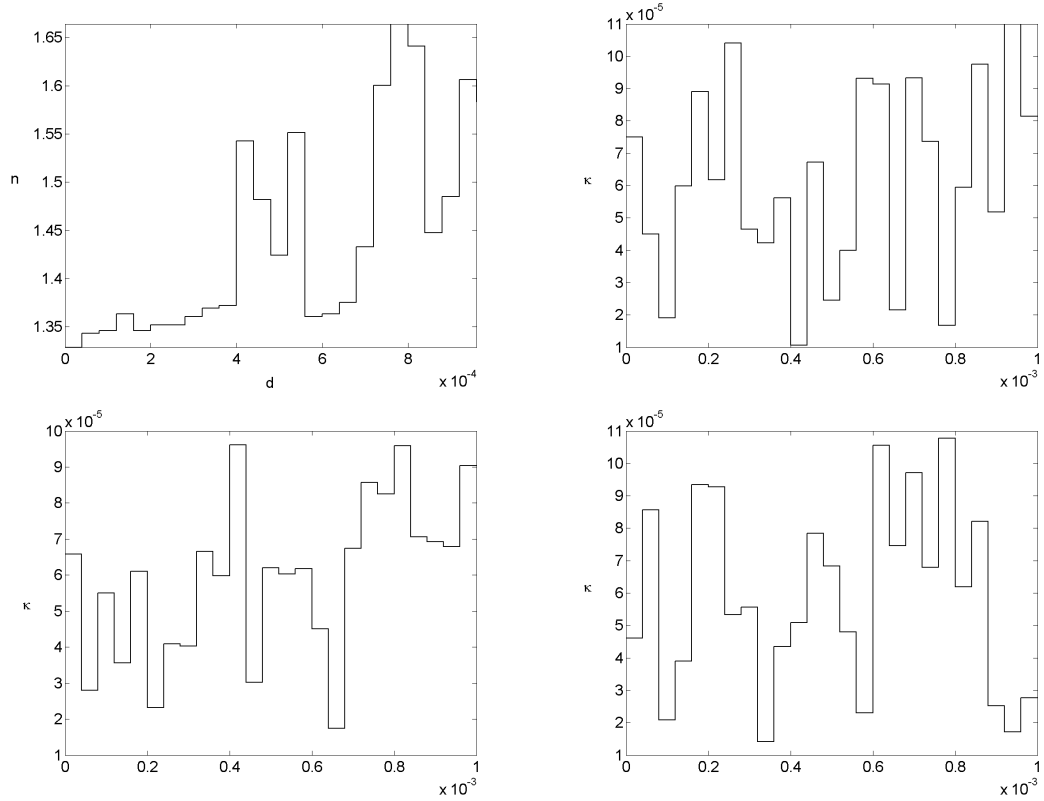


Figure 6.2: 25-layer structure. Upper left: Refractive index distribution. Top right, bottom left and bottom right: Three different (random) absorption distributions.

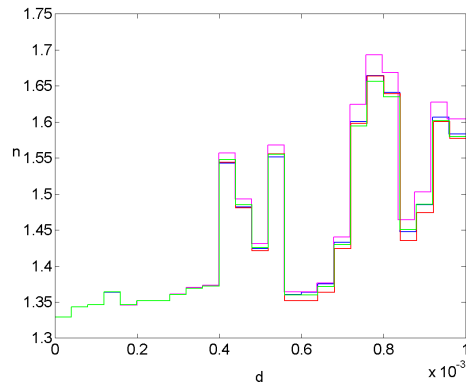


Figure 6.3: 25-layer structure. Refractive index distribution (blue) and the corresponding reconstruction for three different absorption values distributions.

bottom right. The range of values of the absorption coefficient is the same as that in the previous example. Again, the three corresponding reconstructions, obtained under assumption of a constant absorption equal to the average absorption in the true samples

are shown in Figure 6.5 in red, magenta and green, respectively. The quality of these results is similar to that obtained in the previous case, see Table 6.2.

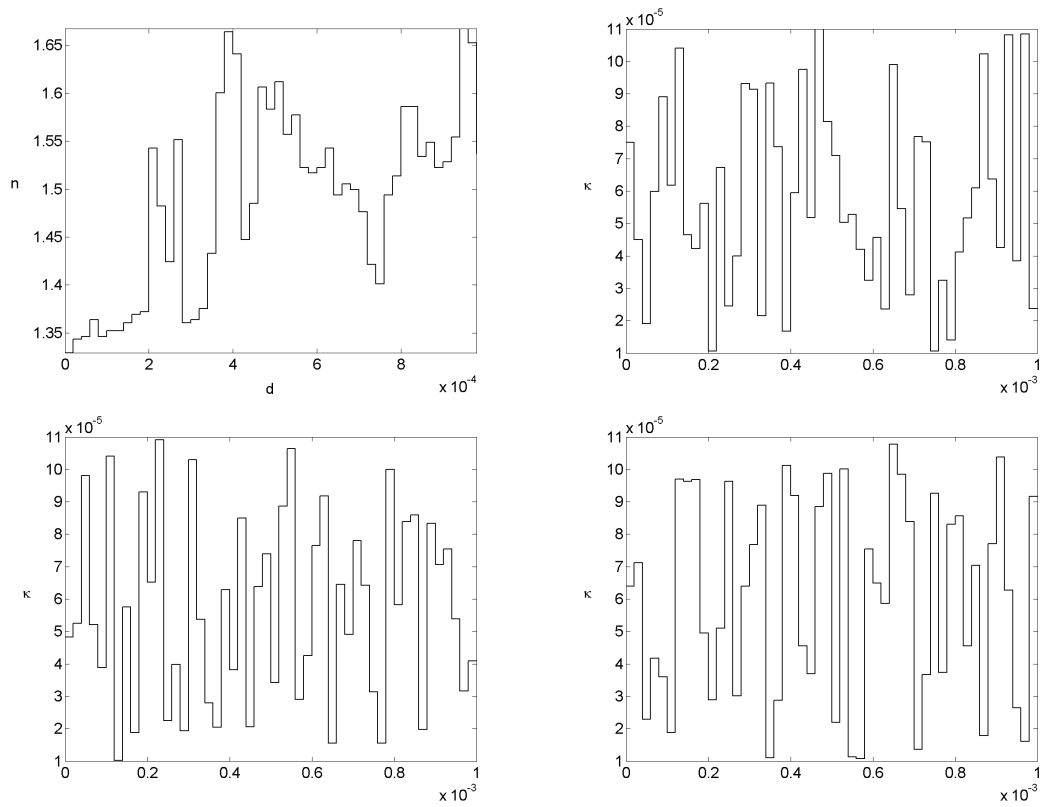


Figure 6.4: 50-layer structure. Upper left: Refractive index distribution. Top right, bottom left and bottom right: Three different (random) absorption distributions.

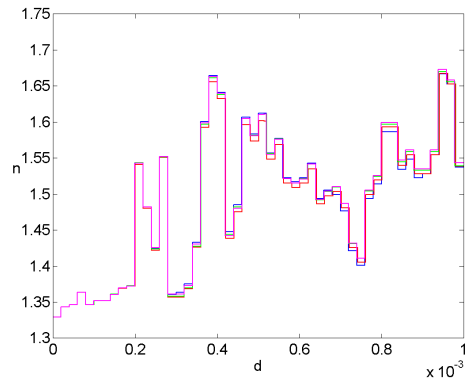


Figure 6.5: 50-layer structure. Refractive index distribution (blue) and the corresponding reconstruction for three different absorption value distributions.

Table 6.2: Errors in n and d reconstruction.

Color	Max Error in n	Max Error in d
Red	0.74%	1.2%
Green	0.68%	1.3%
Magenta	0.88%	1.6%

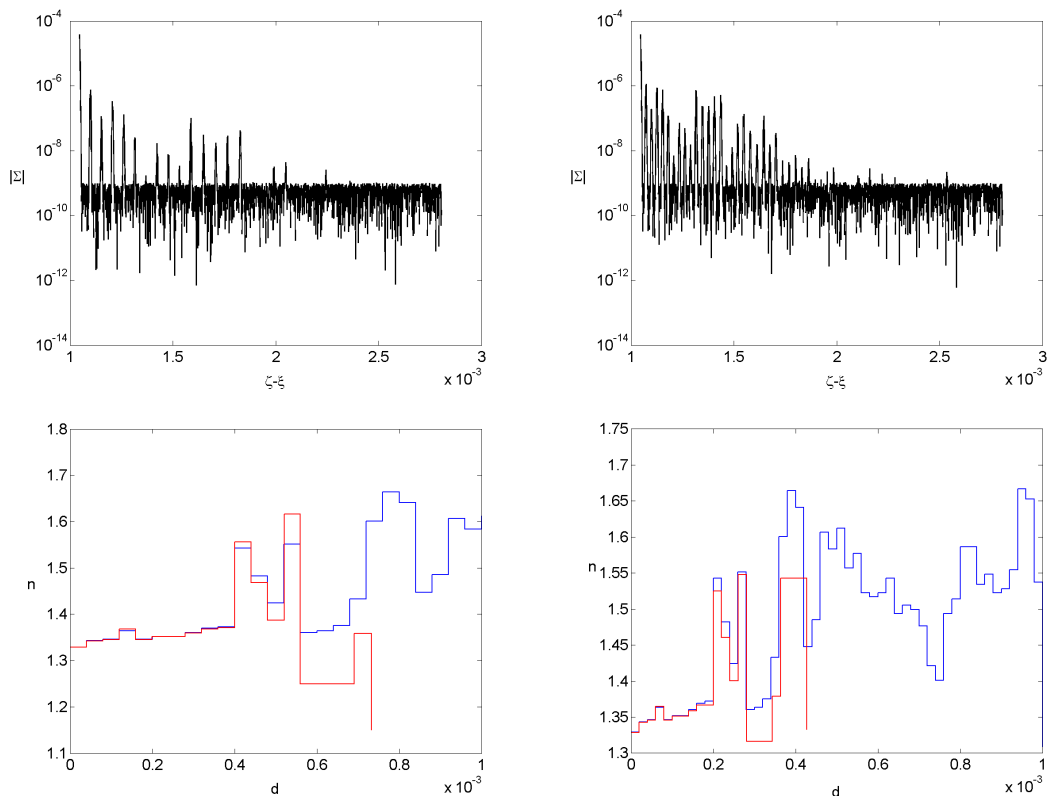


Figure 6.6: $|\Sigma|$ for an absorption ranging between 10^{-4} and 10^{-3} . Top left: 25-layer structure. Top right: 50-layer structure. Bottom left and right: corresponding solutions for these absorption levels.

6.2 Large Absorption/Noise Values

In this section we present examples that demonstrate the effects resulting from large values of absorption and noise. In the first pair of examples we assume samples whose refractive indexes are given by the top left portions of Figures 6.2 and 6.4, respectively, and whose absorptions are ten times those depicted in Figures 6.2 and 6.4 top right, respectively. Figures 6.6 top left and top right, display the corresponding values of the correlation $|\Sigma|$. We see that a significant loss of information occurs, as the increased absorption gives rise

to measured values of the correlation which fall below the noise level. Figure 6.6 bottom left and bottom right display the corresponding solutions produced by our solver in these cases. Clearly, only portions of the sample for which the measurements are not polluted by noise can be reconstructed with any accuracy.

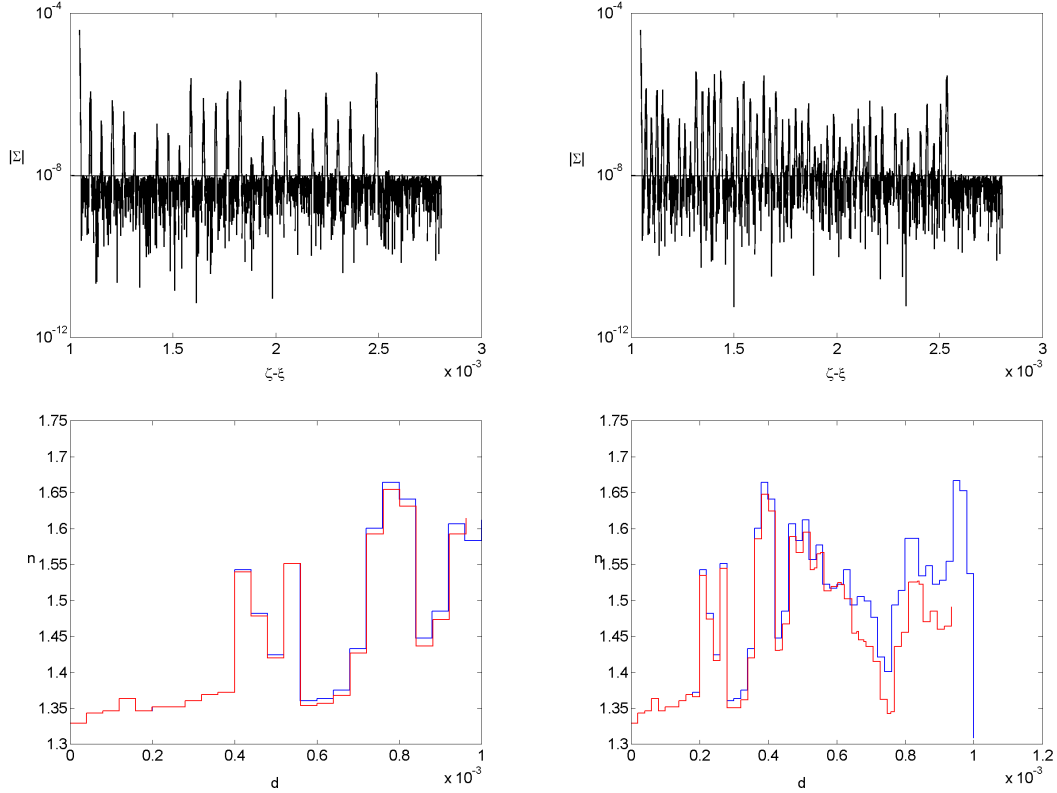


Figure 6.7: $|\Sigma|$ for a noise level of the order of 10^{-3} relative to the maximum interference fringe intensity (which is of the order of 10^{-5}). Top left: 25-layer structure. Top right: 50-layer structure. Bottom left and right: corresponding solutions for these noise levels.

In the second pair of examples we reduce the absorption level back to the values of Figures 6.2 and 6.4, and we study the effect of an increased noise floor by assuming the random noise is of the order of 10^{-8} —a factor of ten higher than all other values assumed in this text. Figures 6.7 top left and top right show the corresponding measured values of $|\Sigma|$ for the 25- and 50-layer structures. We note that the noise floor in these cases equals the threshold value $T^{thresh} = 10^{-8}$ used to detection of interfaces. Still, reasonable solutions are obtained—at least for the more highly illuminated portions of the sample.



Figure 6.8: Left: Chessboard distribution of the original figure, with original color code. Center: Refractive index assignment. Left: reconstructions under assumption of lenses with numerical aperture of $N.A. = 0.054$.

6.3 Volumetric Imaging

As mentioned in Section 4, the inverse solver developed in this thesis does not apply directly to the problem of imaging of volumetric samples containing non-planar layers. To gain an insight on the type of performance that may be hoped for when extending these methods to such three dimensional configurations, in this section we present the results of applications of our algorithm to three imaging problems involving true cell geometries, in which the volumetric geometry has been replaced by a “chessboard approximation”, that is, pixelated array of square voxels. These geometries were obtained from



Figure 6.9: Same as Figure 6.8.

<http://dept.kent.edu/projects/cell/images.html-ssi>; the needed “chessboard” approximations of these geometries are displayed in the left portions of Figures 6.8, 6.9 and 6.10.

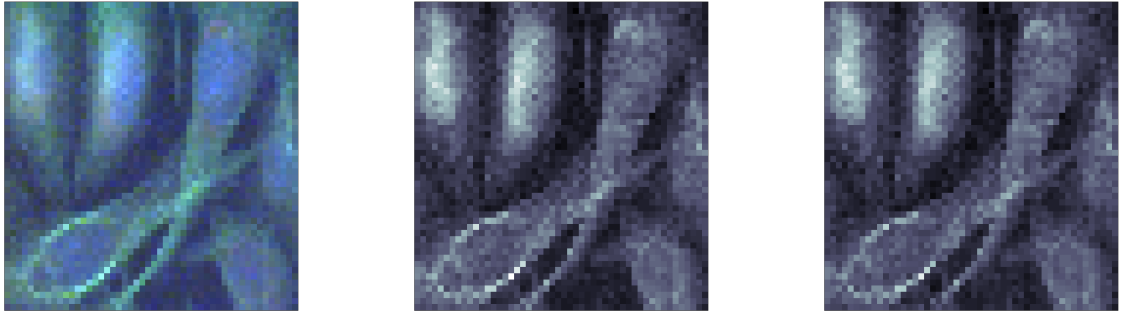


Figure 6.10: Same as Figure 6.8.

For the purposes of our demonstrations we assumed the figures shown are 1mm in side. The 50×50 chessboard structures shown here reflect the level of detail that can be produced under the value of the coherence length assumed in this thesis. Finer resolutions can certainly be obtained, provided light sources with correspondingly reduced coherence lengths are used.

The color code in the left figures matches that of the figures in the website mentioned above. The center Figures, in turn, display our own color code, which represents a value of the refractive index between $n = 1.3$ and $n = 1.8$ and absorptions of the order of $10^{-5} < \kappa < 10^{-4}$ —all fairly common values for biological applications. (The refractive index value at a given pixel in the center figures was chosen as a linearly scaled version of the *red component* in the RGB true-color image map for the corresponding left figures.) The right figures display the results of our reconstructions under assumption of lenses with numerical aperture of $N.A. = 0.054$. Note that each one of the right-hand figures resulted from solution of fifty 50-layer top-to-bottom inverse problems. The reconstructions shown are nearly perfect.

Chapter 7

Conclusions

In this work we introduced and solved a new inverse problem for the one-dimensional Helmholtz equation. In particular, we developed a fast and stable algorithm which, using interference fringes produced by an OCT microscope yields refractive indices and layer-thicknesses for multi-layered structures and which, therefore, makes it possible to determine the internal structure of multi-layered structures from a *direct* sampling of interference fringes. Thus, as mentioned in the introduction, the resulting approach represents a significant improvement over previous methods, as it does not require processing at data-collection time. In particular, while previous methods were limited to consideration of layered structures containing a number of the order of ten layers, the present approach should allow for solution of inverse problems containing thousands of layers in reasonable computing times.

The parallel-layer geometries to which our solver is applicable arise in a range of important engineering applications [24] (e.g., for quality control of transparent films of various materials). We hope, further, that the basic elements developed in this work will help open a door for future researchers to approach the more general two- and three-dimensional cases. A number of issues could be addressed as natural subsequent steps to this work. For example, our inverse solver accounts for absorption and scattering phenomena: We have shown that in many cases only the average absorption coefficient plays a role in the inverse problem and that, for such configurations, the absorption coefficient does not need to be determined accurately—the absorption average thus appears is a parameter that needs to be tuned. The role of absorption for general configurations needs to be studied in depth, however; for example, it is conceivable that slowly varying local absorption averages might be obtainable, so that the shadows regions so common in OCT images could be eliminated.

Other important issues for future work concern acceleration of the algorithm. In par-

ticular, one could use the fast high-frequency integration and integral equation methods presented in [9] to, 1) Evaluate rapidly three-dimensional scattered fields (and thus, the actual correlation term), and 2) Accelerate the algorithm for integration over the surface of the detector. If successful, this strategy would allow for solution of of general OCT inverse problems for three-dimensional bodies.

Appendix A

The Lens

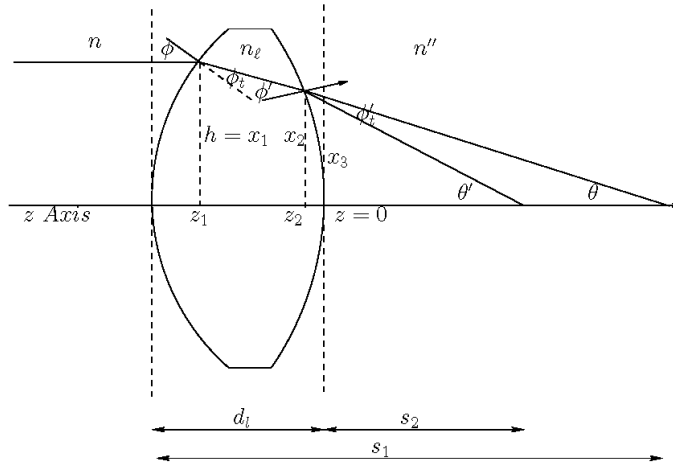


Figure A.1: The lens.

For easy reference, in what follows we present models and mathematical expressions for lenses relevant in our setting. Consider a doubly convex lens with radii r_1 and r_2 , refractive index n_ℓ and axial thickness ℓ [41]. As the incident light strikes the first lens interface the incidence angle with respect to the normal is given by

$$\phi = \arcsin(h/r_1),$$

where h is the height of the incident ray above the axis. By Snell's law the transmission angle ϕ_t with respect to the normal is given by

$$\phi_t = \arcsin(n/n_\ell \sin \phi),$$

while the transmission angle with respect to the z axis and the distance from the surface to the image point are given by

$$\theta = \phi - \phi_t \text{ and } s_1 = r_1 + r_1 \sin \phi_t / \sin \theta,$$

respectively. The four Snell formulae for the second lens surface are

$$\phi' = \arcsin((r_2 + s_1 - d)/r_2 \sin \theta),$$

$$\phi'_t = \arcsin(n_\ell/n'' \sin \phi'),$$

$$\theta' = \phi'_t + \theta - \phi', \tag{A.1}$$

$$s_2 = r_2 \sin \phi'_t / \sin \theta' - r_2, \tag{A.2}$$

where ϕ' and π'_t are the angles of incidence and transmission with respect to the normal to the surface, θ' is the angle of the transmitted ray with respect to the axis and s_2 is the image distance. The amplitude transmission coefficient of the lens is

$$t_\perp = \frac{4nn_\ell \cos \phi \cos \phi'}{(n \cos \phi_t + n_\ell \cos \phi_t)(n_\ell \cos \phi' + n'' \cos \phi'_t)}.$$

To obtain the optical path introduced by the lens let us assume the incident ray intersects the first surface at the point with coordinates $z_1 = r_1 - \ell - \sqrt{r_1^2 - h^2}$, $x_1 = h$, so that the transmitted ray intersects the second surface at the point with coordinates

$$\begin{aligned} x_2 &= \cos^2 \theta (h + \tan \theta (r_2 + z_1 - \\ &\quad - \sqrt{-h^2 + r_2^2 - 2h(r_2 + z_1) \tan \theta - z_1(2r_2 + z_1) \tan^2 \theta})), \\ z_2 &= -\cos^2 \theta (r_2 - h \tan \theta - z_1 \tan^2 \theta - \\ &\quad - \sqrt{-h^2 + r_2^2 - 2h(r_2 + z_1) \tan \theta - z_1(2r_2 + z_1) \tan^2 \theta}), \end{aligned}$$

and it intersects the line $z_3 = 0$ at the height

$$x_3 = x_2 + z_2 \tan \theta'.$$

The optical path-length L is thus given by

$$\begin{aligned} L &= n(r_1 - \sqrt{r_1^2 - h^2}) + n_\ell \sqrt{(z_1 - z_2)^2 + (x_1 - x_2)^2} + \\ &+ n_\ell \sqrt{(z_2 - z_3)^2 + (x_2 - x_3)^2}. \end{aligned} \quad (\text{A.3})$$

Therefore, if the lens is illuminated by an (infinitely thin) ray of monochromatic light given by

$$E_i = E_0 e^{ik_0 z},$$

the corresponding light transmitted by the lens is given by

$$E_t = E_0 t_\perp e^{i\varphi} e^{ik_0(\cos\theta'(z-d) - \sin\theta'(x-x_3))},$$

with $\varphi = k_0 L$.

A.1 Paraxial Approximation

Assuming small values of ϕ we have

$$\begin{aligned} \cos \phi &\approx 1, \\ \sin \phi &\approx \tan \phi \approx \phi, \end{aligned}$$

so that all rays intersect the z axis at a point P a distance

$$f = \frac{n''(d(n - n_\ell) + n_\ell r_1)r_2}{d(n - n_\ell)(n_\ell - n'') + n_\ell(-n''r_1 - n_\ell r_2 + n_\ell(r_1 + r_2))}, \quad (\text{A.4})$$

away from the end of the second surface of the lens.

Expanding the quantity s_2 in equation (A.2) in Taylor's Series around $h = 0$ we obtain

$$s_2 = f + Ch^2 + O(h^3),$$

where C is a constant that depends on the refractive indexes n, n_ℓ, n'' and on the dimensions of the lens. From these expressions one can see that the error in the paraxial approximation may not be negligible for cases in which the numerical aperture of the lens ($= \sin(\max(\theta'))$)

is not small.

Bibliography

- [1] American Institute of Physics, Section editors: Bruce H. Billings [and others], Coordinating editor: Dwight E. Gray, *American Institute of Physics Handbook*, New York, McGraw-Hill, 1972.
- [2] Z. S. Agranovich and V.A. Marchenko, *The Inverse Problem of Scattering Theory*, New York, English translation by Gordon and Breach, 1963.
- [3] S. R. Arridge and M. Schweiger, *Image reconstruction in optical tomography*, Phil. Trans. R. Soc. London. B, Vol. 352, 717-726, 1997.
- [4] S. R. Arridge, *Optical tomography in medical imaging*, Inverse Problems, Vol. 15(2), R41-R93, 1999.
- [5] K. Balasubramaniam, V. V. Shah and R. D. Costley, G. Boudreaux, J. P. Singh, *High temperature ultrasonic sensor for the simultaneous measurement of viscosity and temperature of melts*, Review of Scientific Instruments, Vol. 70(12), 4618-4623, 1999.
- [6] G. Borg, *Eine Umkehrung der Sturm-Liouvilleschen eigenwertaufgabe. Bestimmung der differentialgleichung durch die eigenwerte*, Acta Math., Vol. 8, 1-96, 1946.
- [7] B. E. Bouma and G. J. Tearney, *Handbook of Optical Coherence Tomography*, Marcel Dekker, 2002.
- [8] O. P. Bruno and J. Chaubell, *The inverse scattering problem for optical coherence tomography*. To appear in Optics Letters, Issue Date: 11/01/03.
- [9] O. P. Bruno, C. A. Geuzaine, J. A. Monroe, Jr. and F. Reitich, *Prescribed error tolerances within fixed computational times for scattering problems of arbitrarily high frequency: the convex case*, to appear in Philosophical Transactions of the Royal Society.

- [10] O. P. Bruno and E. M. Hyde, *A fast high-order method for scattering by inhomogeneous media in two dimensions: theoretical considerations*, In preparation.
- [11] G. Byrne and Ch. Hall, *Numerical Solution of Systems of Nonlinear Algebraic Equations*, Academic Press, 1973.
- [12] K. Chadan and P. C. Sabatier, *Inverse Problems in Quantum Scattering Theory*, Springer-Verlag, 1977.
- [13] Y. Chen and V. Rokhlin, *On the inverse scattering problem for the Helmholtz equation in one dimension*, Inverse Problems, Vol. 8, 365-391, 1992.
- [14] W. C. Chew, *Waves and Fields in Inhomogeneous Media*, Van Nostrand Reinhold, 1990.
- [15] P. Deift and E. Trubowitz, *Inverse scattering on the line*, Comm. Pure Appl. Math, Vol. 32, 121-251, 1979.
- [16] J. A. den Boer, *Magnetic Resonance Imaging*, Springer, 1996.
- [17] A. Diaspro, *Confocal and Two-Photon Microscopy: Foundations, Applications, and Advances*, Wiley-Liss, 2002.
- [18] M. Dunn and S. I. Hariharan, *One dimensional inverse scattering problem*, J. Computational Physics, Vol. 55, 157-165, 1984.
- [19] A. Entwistle, *Confocal microscopy: an overview with a biological and fluorescence microscopy bias*, The Quekett Journal of Microscopy , Vol. 38, 445-456, 2000.
- [20] A. J. Faber, F. Simonis, R. Breeuwer and H. Dewaal, *Application of ultrasonic measuring techniques in industrial glass melting*, Glastechnische Berichte-Glass Science and technology, Vol. 64(5), 117-122, 1991.
- [21] A. F. Fercher, W. Drexler, C. K. Hitzenberger and T. Lasser, *Optical coherence tomography: principles and applications*, Rep. Prog. Phys., Vol. 66, 239-303, 2003.
- [22] G. Frontini, J. Chaubell and G. Eliçabe, *Deconvolution by spline functions to estimate the relaxation spectrum of viscoelastic fluids* , Latin American Applied Research, Vol. 25-S, 17-22, 1995.

- [23] G. Frontini and J. Chaubell, *Inversion of turbidity measurements of polymer latex using wavelet functions*, Chemometrics and intelligent laboratory systems, Vol. 47, 89-97, 1999.
- [24] T. Fukano and I. Yamaguchi, *Simultaneous measurement of thicknesses and refractive indices of multiple layers by a low-coherence confocal interference microscope*, Optics Letters, Vol. 21(23), 1942-1944, 1996.
- [25] T. Fukano and I. Yamaguchi, *Separation of measurement of the refractive index and the geometrical thickness by use of a wavelength-scanning interferometer with a confocal microscope*, Applied Optics, Vol. 38(19), 4065-4073, 1999.
- [26] C. S. Gardner, J. M. Greene, M. D. Kruskal, and R. M. Miura, *Method of solving the Korteweg-de Vries equation*, Phys. Rev. Lett., Vol. 19, 1095-1097, 1967.
- [27] I. M. Gelfand and B. M. Levitan, *On the determination of a differential equation from its spectral function*, Am. Math. Soc. Transl., Vol. 2(1), 253-304, 1951.
- [28] H. H. Gilgen, R. P. Novák, R. P. Salathé, W. Hodel and P. Béaud *Submillimeter optical reflectometry*, J. of lightwave Tech., Vol. 7(8), 1225-1233, 1989.
- [29] J. W. Goodman, *Statistical Optics*, John Wiley and Sons, 1985.
- [30] F. Hagin, *Some numerical approaches to solving one- dimensional inverse problems*, J. Computational Physics, Vol. 43, 16-30, 1981.
- [31] E. Hecht and A. Zajac, *Optics*, Addison-Wesley, 1979.
- [32] G. Herman, *Image Reconstruction from Projections: the Fundamentals of Computed Tomography*, Academic Press, 1980.
- [33] G. Herman and D. Odhner, *Mathematical Methods in Tomography*, Heidelberg: Springer, 1991.
- [34] C. K. Hitzenberger, *Measurement of corneal thickness by low-coherence interferometry*, Applied Optics, Vol. 31(31), 6637-6642, 1992.
- [35] J. W. Hettinger, M. de la Peña Mattozzi, W. R. Myers, M. E. Williams, A. Reeves, R. L. Parsons, R. C. Haskell, D. C. Petersen, R. Wang, and J. I. Medford *Optical*

coherence microscopy. A technology for rapid, in vivo, non-destructive visualization of plants and plant cells, Plant Physiology, Vol. 123, 3-15, May 2000.

- [36] B. M. Hoeling, A. D. Fernandez, R. C. Haskell, E. Huang, W. R. Myers, D. C. Petersen, S. E. Ungersma, R. Wang, M. E. Williams and S. E. Fraser *An optical coherence microscope for 3 dimensional imaging in developmental biology*, Optics Express, Vol. 6, 136-146, March 2000.
- [37] J. P. Hornak, The Basics of MRI, <http://www.cis.rit.edu/htbooks/mri/>
- [38] D. Huang, E. Swanson, C. P. Lin, J. S. Schuman, W. G. Stinson, W. Chang, M. R. Hee, T. Flotte, K. Gregory, C. A. Puliafito, and J. G. Fujimoto, *Optical coherence tomography*, Science, Vol. 254, 1178-1181, 1991.
- [39] J. Izatt, M. Hee, G. Owen, E. Swason and J. Fujimoto, *Optical coherence microscopy in scattering media*, Optics Letters, Vol. 19(8), 590-592, 1994.
- [40] J. D. Jackson, *Classical Electrodynamics*, New York: Willey, 1999.
- [41] F. Jenkins, H. White, *Fundamentals of Optics*, McGraw-Hill, 1957.
- [42] R. Jost and W. Kohn, *Construction of a potential from a phase shift*, Phys. Rev., Vol. 87, 977-992, 1952.
- [43] G.W.C. Kaye, *Tables of Physical and Chemical Constants*, Essex, England, New York : Longman, 1995.
- [44] A. Kirsch, *An Introduction to the Mathematical Theory of Inverse Problems*, Springer, 1996.
- [45] A. D. Klose and A. H. Hielscher, *Quasi-Newton methods in optical tomographic image reconstruction*, Inverse Problems, Vol. 19, 387-409, 2003.
- [46] N. Levison, *On the uniqueness of the potential in a Schrödinger equation for a given asymptotic phase*, Mat. Tidskr. B, 25-30, 1949.
- [47] A. K. Louis, *Medical imaging: state of the art and future development*, Inverse Problems, Vol. 8, 709-738, 1992.

- [48] National Research Council, Institute of Medicine, *Mathematics and Physics of Emerging Biomedical Imaging*, National Academy Press, 1996.
- [49] A. A. Michelson, *Interference phenomena in a new form of refractometer*, Phil. Mag, Vol. 13(5), 236-242, 1882.
- [50] M. Minsky, *Memoir on inventing the confocal scanning microscope*, Scanning, Vol 10(4), 128-138, 1988.
- [51] R. Modre, B. Tilg, G. Fisher and P. Wach, *Noninvasive myocardial activation time imaging: A novel inverse algorithm applied to clinical ECG mapping data*, IEEE Transaction on Biomedical Engineering, Vol. 49 (10), 1153-1161, 2002.
- [52] D. L. Phillips, *A technique for the numerical solution of certain integral equations of the first kind*, J. ACM 9, 1962.
- [53] N. Polydorides and H. McCann, *Electrode configurations for improved spatial resolution in electrical impedance tomography*, Meas. Sci. Technol., Vol. 13, 1862-1870, 2002.
- [54] R. T. Prosser, Bulletin of the American Mathematical Society, Vol. 29, 139-144, 1993.
- [55] A. Puttmer, P. Hauptmann and B. Henning, *Ultrasonic density sensor for liquids*, IEEE Transactions on ultrasonics ferroelectrics and frequency control, Vol. 47(1), 85-92, 2000.
- [56] I. T. Rekanos, S. Panas and T. Tsiboukis, *Microwave imaging using the finite-element method and a sensitivity analysis approach*, IEEE, Transactions on medical imaging, Vol. 18(11), 1108-1114, 1999.
- [57] R. A. Robb, *Three Dimensional Biomedical Imaging: Principles and Practice*, New York: VCH, 1995.
- [58] T., G., Rochow and P., A., Tucker, *Introduction to Microscopy by Means of Light Electrons, X Rays, or Acoustics*, New York: Plenum Press, 1994.
- [59] W., J., Schempp, *Magnetic Resonance Imaging: Mathematical Foundations and Applications*, Wiley-Liss, 1998.
- [60] J. M. Schmitt, A. Knuttel and R. F. Bonner, *Measurement of optical-properties of biological tissues by low-coherence reflectometry*, Applied Optics, Vol. 32(30), 6032-6042, 1993.

- [61] J. C. Schotland and V. A. Markel, *Inverse scattering with diffusing waves*, J. Opt. Soc. Am. A, Vol. 18(11), 2001.
- [62] M. Schweiger and S. R. Arridge, *Optical tomography reconstruction in a complex head model using a priori region boundary information*, Phys. Med. Biol., Vol. 44, 2703-2721, 1999.
- [63] P. T. So, C. Y. Dong, B. R. Masters and K. M. Berland, *Two-photon excitation fluorescence microscopy*, Annual Review of Biomedical Engineering, Vol. 2, 399-429, 2000.
- [64] K. Takada, I. Yokohama, K. Chida and J. Noda, *New measurement system for fault location in optical wave-guide based on devices on an interferometric technique*, Applied Optics, Vol. 26(9), 1603-1606, 1987.
- [65] G. J. Tearney, M. E. Brezinski and J. F. Southern, B. E. Bouma, M. R. Hee, and J. G. Fujimoto, *Determination of the refractive index of highly scattering human tissue by optical coherence tomography*, Opt. Lett, Vol. 20(21), 2258-2260, 1995.
- [66] A. Tikhonov and V. Arsenin, *Solutions of Ill-Posed Problems*. Winston and Sons, 1997.
- [67] M. Yadlowsky, J. Schmitt and R. Bonner, *Multiple-scattering in optical coherence microscopy*, Appl. Optics, Vol. 34(25), 5699-5707, 1995.
- [68] R. Youngquist, S. Carr and D. Davies, *Optical coherence-domain reflectometry: a new optical evaluation technique*, Appl. Opt., Vol. 26, 158-160, 1987.
- [69] Y. Watanabe and I. Yamaguchi, *Geometrical tomography imaging of refractive indices through turbid media by a wavelength-scanning heterodyne interference confocal microscope*, Applied Optics, Vol. 41(13), 2002.